ABSTRACT

Title of Dissertation: MOLD PROCESS INDUCED RESIDUAL STRESS PREDICTION USING CURE EXTENT DEPENDENT VISCOELASTIC BEHAVIOR

Sukrut Prashant Phansalkar, Doctor of Philosophy, 2024

Dissertation directed by: Professor Bongtae Han, Mechanical Engineering

Epoxy molding compounds (EMC) are widely used in encapsulation of semiconductor packages. Encapsulation protects the package from physical damage or corrosion due to harsh environments. Molding processes produce residual stresses in encapsulated components. They are combined with the stresses caused by the coefficient of thermal expansion (CTE) mismatch to dictate the final warpage at room and reflow temperatures, which must be controlled for fabrication of redistribution layer (RDL) as well as yield during assembly.

During molding process, EMC is continuously curing and the mechanical properties continue to evolve; more specifically, the equilibrium modulus and the relaxation modulus. The former defines behavior after complete relaxation while the latter describes the transient behavior. It is thus necessary to measure cure-dependent viscoelastic properties of EMC to be able to determine mold induced residual stresses accurately. This is the motivation for this thesis.

In this thesis, a set of novel methodologies are developed and implemented to quantify a complete set of cure-dependent viscoelastic properties, including the fully cured properties. Firstly,

an advanced numerical scheme has been developed to quantify cure kinetics of thermosets with both single and dual-reaction systems. Secondly, a unique methodology is proposed to measure the viscoelastic bulk modulus -$K(t,T)$ of EMC using hydrostatic testing. The methodology is implemented with a unique test setup based on inert gas. The results of viscoelastic testing along with the shear modulus (G) and bulk modulus (K) master curves and temperature-dependent shift factors (a_T) of fully-cured EMC are presented.

Thirdly, a novel test methodology utilizing monotonic testing has been developed to measure two sets of equilibrium moduli - $E_\infty(p)$ and $K_\infty(p)$ of EMC as a function of cure extent (p). The main challenge for the measurements is that the equilibrium moduli could only be measured accurately only when the EMC has fully relaxed. The temperatures for complete relaxation typically occur above the glass transition temperature, $T_g(p)$, where the curing rate is also high. A special measurement procedure is developed, through which the EMC moduli above T_g can be determined quickly at a near isocure state. Viscoelastic testing of partially-cured EMC is followed to determine the cure-dependent shift factors of EMC. The test durations have to be very long (several hours) and it is conducted below $T_g(p)$ of the EMC where the reaction is slow (under diffusion-control)

Finally, a numerical scheme that can utilize the measured cure-dependent viscoelastic properties is developed. It is implemented to predict the residual stress evolution of molded packages during and after molding processes.

MOLD PROCESS INDUCED RESIDUAL STRESS PREDICTION USING CURE EXTENT DEPENDENT VISCOELASTIC BEHAVIOR

By

Sukrut Prashant Phansalkar

Dissertation submitted to the Faculty of the Graduate School of the
University of Maryland, College Park, in partial fulfillment
of the requirements for the degree of
Doctor of Philosophy
2024

Advisory Committee:
Professor Bongtae Han, Chair/Advisor
Professor Peter Sandborn
Professor Avik Dutt
Professor Michael Azarian
Professor Sung Lee, Dean's Representative

© Copyright by

Sukrut Prashant Phansalkar

2024

UNIVERSITY OF MARYLAND

2181 Glenn L. Martin Hall
College Park, MD 20742-3035
TEL: 301-405-2410
http://www.enme.umd.edu

07/17/2024

Re: Previously Published Materials appearing in Thesis or Dissertation

Dean of the Graduate School,

Sukrut Prashant Phansalkar (UID: 116243674) has:

☐ **NOT INCLUDED any previously published works within their thesis or dissertation.**

☒ **INCLUDED one or more previously published works within their thesis or dissertation. This letter certifies that** the examining committee for the student has determined that the student made a substantial contribution to the previously published work. The inclusion of the previously published work has the approval of the thesis or dissertation advisor and the Graduate Director.

Sincerely,

Peter Sandborn
Director of Graduate Studies
Department of Mechanical Engineering
University of Maryland

Sincerely,

Bongtae Han
Advisor for Sukrut Prashant Phansalkar

Table of Contents

Table of Figures..... vii

Chapter 1 Introduction..... 1

1.1. Motivation..... 1

1.2. Objectives..... 2

1.3. Organization of Dissertation..... 3

Chapter 2 Effect of Critical Properties of Epoxy Molding Compound on Warpage Prediction: A Critical Review..... 5

2.1. Introduction..... 5

2.2. Effective Cure Shrinkage (ECS)..... 9

2.2.1. Cure kinetics..... 9

2.2.2. Measurement of ECS..... 10

2.2.3. Transfer molding and compression molding..... 14

2.2.4. Discussion: Mold shrinkage..... 17

2.3. Time and Temperature Dependent Behavior of Polymers..... 19

2.3.1. Linear viscoelasticity..... 19

2.3.2. Critical assumptions used in the current practice..... 25

2.3.3. Measurement of bulk modulus..... 27

2.4. Cure-extent dependent Viscoelastic Behavior..... 31

2.4.1. Cure-extent dependent shear viscoelasticity..... 31

2.4.2. Time-cure superposition (TCS)..... 33

2.4.3. Measurement of cure-extent dependent viscoelastic properties..... 35

2.5. Additional discussion: About compression molding..... 36

2.6. Concluding Remarks..... 39

Chapter 3 Deterministic Approach to Obtain Autocatalytic Cure Kinetics Model Constants by Normal Equations of Least-Squares Method..... 41

3.1. Introduction..... 41

3.2. Cure kinetics Model..... 42

3.3. Proposed Deterministic Approach 43
3.4. Implementation 47
3.5. Discussions 50
3.6. Conclusions 51

Chapter 4 Novel Method to Determine Autocatalytic Cure Kinetics Model Constants of Dual Reaction Thermosets Using Minimum Testing Data 53

4.1. Introduction 53
4.2. Cure Kinetics Model and Kinetic Analysis 54
4.2.1. General reaction kinetics model 55
4.2.2. Isoconversional analysis: Friedman method 56
4.3. Deterministic Approach to Obtain Kamal-Sourour Model Constants [105] 57
4.4. Proposed Method 58
4.5. Implementation 61
4.6. Discussion 68
4.7. Conclusions 70

Chapter 5 Characterization of Bulk Behavior of EMC 72

5.1. Background and Motivation 72
5.1.1. Temperature-dependent bulk behavior measurement by P-V-T-C 72
5.1.2. Time-dependent bulk behavior measurement by embedded fiber Bragg grating (FBG) 75
5.1.2.1. Heat generation induced by gas 78
5.1.2.2. Errors associated with the governing equations used to determine bulk modulus 80
5.2. Proposed Method 81
5.2.1. Determination of optimum loading profiles to negate the heat generation 82
5.2.2. Analytical derivation for an n-chain model for linear + constant loading 86
5.2.3. Methodology to determine compressibility Prony series constants from the experimental data 88
5.3. Implementation of the Proposed Method 91
5.3.1. Description of the testing apparatus 91

5.3.2. Fabrication of EMC specimen 92
5.3.3. Measurement data 93
5.3.4. Data analysis and compressibility calculations 96
5.3.4.1. Viscoelastic Young's modulus measurement 97
5.3.4.2. Compressibility calculations 101
5.4. Discussions 104
5.4.1. Repeatability of measurements 104
5.4.2. Iteration issue 105

Chapter 6 Interconversion of Viscoelastic Properties 107

6.1. Introduction 107
6.2. Background and Assumption made in current practice 108
6.2.1. Assumptions and simplications used in the current practice of viscoelastic modeling 109
6.2.1.1. Use of $\boldsymbol{Et}$ Prony series for $\boldsymbol{G(t)}$ and constant bulk modulus - $\boldsymbol{K0}$ 110
6.2.1.2. Determination of $\boldsymbol{Gt}$ and $\boldsymbol{K(t)}$ master curves assuming constant Poisson's ratio - $\boldsymbol{\nu 0}$ 112
6.3. Interconversion of Viscoelastic Properties from Governing Equations 113
6.3.1. Calculation of shear relaxation modulus - $\boldsymbol{G(t)}$ from $\boldsymbol{E(t)}$ and $\boldsymbol{K(t)}$ 114
6.3.2. Calculation of viscoelastic Poisson's ratio - $\boldsymbol{\nu(t)}$ from $\boldsymbol{E(t)}$ and $\boldsymbol{K(t)}$ 115

Chapter 7 Characterization of Cure-extent Dependent Viscoelastic Behavior117

7.1. Theoretical Background: Cure-dependent Viscoelasticity 117
7.1.1. Cure-rheological simplicity (CRS) 118
7.1.1.1. Time-cure superposition (TCS) 119
7.1.1.2. Evolution of equilibrium moduli during curing 120
7.2. Background and Motivation 121
7.2.1. Cure-dependent viscoelastic measurements of EMC 121
7.2.2. Cure-dependent viscoelastic measurements of unfilled thermosets 128
7.3. Proposed Method 133
7.3.1. Proposed equilibrium moduli measurement procedure 133
7.3.2. Proposed cure-dependent shift factor measurement procedure 135

7.4. Equilibrium Moduli Measurements 136
7.4.1. Measurement of $\boldsymbol{Tg}(\boldsymbol{p})$ using DSC 136
7.4.2. Measurement of gel point ($\boldsymbol{pgel}$) 139
7.4.3. Gel point determination of EMC 142
7.4.4. Experiments to measure the equilibrium moduli 146
7.4.5. Evolution model calculation 150
7.5. Cure-dependent Shift-factors Measurements 154
7.5.1. Measurement of diffusion-controlled cure-kinetics 154
7.5.2. Determination of cure-dependent shift-factors ($\boldsymbol{ap}(\boldsymbol{p})$) using MFT sweeping 158
7.5.2.1. Discussion: Temperature-dependent shift-factors ($\mathbf{log}\boldsymbol{aT}$) for partially-cured specimen 163
7.6. Implementation of Time-cure superposition (TCS) in a commercial FEM program 164
7.6.1. Cure extent ($\boldsymbol{p}$) – Thermal ($\boldsymbol{T}$) analogy 165
7.6.1.1. Cure-dependent viscoelastic master curves - $\boldsymbol{G}(\boldsymbol{t},\boldsymbol{p})$ and $\boldsymbol{K}(\boldsymbol{t},\boldsymbol{p})$ 166
7.6.2. Comparison of relaxation behavior at various cure extents with analytical solution 167
7.6.3. Mold process simulation using a TFBGA package 168

Chapter 8 Thesis Contributions and Future Work 173
8.1. Thesis Contributions 173
8.2. Future Work 175

Appendix 177
A-1 First-order and second-order optimality criterion for a system of linear equations. 177

References 179

Table of Figures

Figure 1 Schematic illustration of a package warpage history: warpage caused by (a) transfer molding; and (b) heating the package from mold temperature to reflow temperature..... 5

Figure 2 Illustration of (a) solder bridging and (b) solder opening during board level assembly .. 6

Figure 3 Illustration of (a) desired and (b) undesired warpage combinations in PoP stacking. 7

Figure 4 Illustration of the warpage of FO-WLP wafer at room temperature 7

Figure 5 Evolution of cure shrinkage and modulus during curing 11

Figure 6 Schematic illustration of a setup used to measure the effective cure shrinkage of EMC: (a) application of the mold pressure to collapse an EMC pellet; and (b) curing the FBG-embedded EMC specimen inside a constraint-free fixture..... 13

Figure 7 Effective cure shrinkage of EMC as a function of normalized time where the inset shows the BW signal of initial 40 min. 13

Figure 8 Schematic illustration of transfer molding process: (a) EMC is charged, and the mold is heated to the mold temperature; (b) EMC remains as a viscous liquid during EMC transfer (before EMC passes its gel point); and (c) EMC becomes a deformable solid as soon as EMC passes its gel point. 15

Figure 9 Schematic illustration of compression molding process: (a) EMC is charged, and the mold is heated to the mold temperature; (b) EMC remains as a viscous liquid during EMC transfer (before EMC passes its gel point); (c) EMC becomes a deformable solid as soon as EMC passes its gel point, and the pressure continuously deforms EMC until the mold is opened. 17

Figure 10 Illustration of the dimensions of (a) cavity at room temperature and (b) molded EMC at room temperature..... 18

Figure 11 Illustration of the material behavior of TRS polymers..... 21

Figure 12 Procedure to create a master curve and to obtain shift factors using the TTS principle 22

Figure 13 Representative DMA results: (a) Storage modulus obtained from the MFT sweep; (b) shift factors (a_T); (c) storage modulus master curve in the frequency domain; and (d) relaxation modulus master curve in the time domain..... 24

Figure 14 Implication of the assumption of bulk modulus behavior: (a) time-independent; and (b) temperature-independent behavior 26

Figure 15 Schematic illustration of high-pressure dilatometer..... 28

Figure 16 FBG embedded EMC specimen 29

Figure 17 Schematic illustration of a setup to measure the bulk modulus 29

Figure 18 Bulk modulus of EMC: (a) 1 second isochronous values as a function of temperature; and (b) time-dependent values obtained at a temperature near T_g..... 30

Figure 19 Schematic illustration of cure extent dependent EMC behavior: (a) equilibrium modulus evolution; (b) relaxation modulus as a function of time; and (c) complete time dependent behavior 33

Figure 20 Illustration of the TCS concept, where the relaxation modulus obtained at various cure extents are normalized by the difference between the glassy modulus and the equilibrium modulus 34

Figure 21. Strain evolution from a test simulating compression molding, where the pressure is 7 MPa: (a) complete strain evolution and (b) zoom-in view marked by a box in (a)..... 38

Figure 22. Schematic illustration of warpage behavior after demolding at the mold temperature: (a) compression molding and (b) transfer molding 39

Figure 23 A plane defined by the nth order model (Eq. 8); and a line produced by a single dynamic scan data..... 46

Figure 24 DSC dynamic scan data at the standard heating rates of β = 5 and 10 °C/min; the data is scaled by the higher heating rate (β_{ref} = 10 °C/min). 48

Figure 25 Rate of reactions (dp/dt) as a function of temperature (T), obtained from the data shown in Figure 24 48

Figure 26 Precited cure extent is compared with experimental data. Only the data obtained from the standard rates of β = 5 and 10 °C/min are used to determine the model parameters, and the additional dynamic scan data (β = 2.5 and 7.5 °C/min) are used only for comparison. 50

Figure 27 Curved surfaces represented by Eq. (35), where black and blue planes are obtained from Eq. (38) and (14), respectively. The intersecting line (red) coincides with a curved line produced by the single dynamic scan data of 5 °C/min 51

Figure 28 Schematic diagram of a flip-chip IC package 62

Figure 29 DSC dynamic scan data at the standard heating rates of β = 5 °C/min and 10 °C/min; the data is scaled by the higher heating rate (β_{ref} = 10 °C/min). 63

Figure 30 Rate of reactions (dp/dt) as a function of temperature (T), obtained from the data shown in Figure 29 63

Figure 31 Friedman analysis plot containing lines through isoconversion points obtained from the two standard DSC dynamic scan data (β = 5 °C/min and 10 °C/min) 64

Figure 32 Apparent activation energy as a function of cure extent, obtained from the Friedman analysis. 64

Figure 33 DSC data of $\beta = 5$ °C/min is compared with the predicted values: (a) the curing rates and (b) the cure extents..... 68

Figure 34 Predicted cure extent is compared with the experimental data. Only data obtain from two dynamic scanning rates - $\beta = 5$ °C/min and 10 °C/min are used to determine the model constants and the additional scan data ($\beta = 2.5$ °C/min and 7.5 °C/min) are used for validation. 68

Figure 35 Schematic of a P-V-T/ plunger-based high-pressure dilatometer setup 72

Figure 36 Volume change for EMC in different temperature and pressure for PVT measurement [110] 74

Figure 37 FBG embedded specimen subjected to mechanical loading for measurement of mechanical properties 76

Figure 38 Schematic of hydrostatic testing chamber assembly 78

Figure 39 BW signals demonstrating the effect of heat generation due to the instantaneous pressure application 79

Figure 40 Schematic of a polymer specimen with embedded FBG under axial and radial loading 81

Figure 41 A illustration of a standard linear solid (SLS) using a spring-dashpot model..... 83

Figure 42 Results of the virtual experiment and the optimization program to determine $B(t)$ – (a) Strain data as a function of time, and (b) comparison of the compressibility values used vs the values obtained from optimization program 90

Figure 43 A schematic drawing of the hydrostatic test setup designed to measured time-dependent bulk behavior 91

Figure 44 EMC specimen with the strain gauge attached fabricated for hydrostatic testing 93

Figure 45 Hydrostatic testing at room temperature – (a) pressure and strain as a function of time, (b) strain vs. pressure (psi) over the linear ramp period. 94

Figure 46 Raw experimental hydrostatic strain data at various temperatures of testing 96

Figure 47 A photo of EMC specimen mounted on the three-point bend fixture (TA DMA850) for viscoelastic testing 98

Figure 48 Raw MFT sweeping data of storage modulus ($E'(\omega)$) – 20°C to 240°C (10°C/step) and 0.1-25 Hz (5 points/decade) 99

Figure 49 Results of TTS shifting from EMC DMA testing – (a) Storage modulus master curve and (b) shift-factors ($\log aT$) vs. temperature (°C) 100

Figure 50 Time-domain Young's relaxation modulus master curve ($Tref = 130°C$) 100

Figure 51 Illustration of the optimization program using data at 130°C – (a) Pressure profile data, (b) Calculated compressibility values and (c) comparison of prediction vs the experimental hydrostatic strain data with the obtained constants. 101

Figure 52 Comparison of the strain data obtained from experiment with the prediction of strain using the compressibility Prony series obtained from the optimization program 103

Figure 53 Bulk behavior master curves obtained from the experimental data – (a) compressibility, and (b) bulk modulus ($Tref = 130°C$) 103

Figure 54 Comparison of compressibility obtained from Test 1 vs Test 2 104

Figure 55 Comparison of compressibility evaluated for 2 temperatures (130 and 145°C) using single data sets versus the entire data set. 105

Figure 56 Comparison of real $G(t)$ and $K(t)$ master curves with the master curves obtained using the assumptions. 111

Figure 57 Calculation of time-dependent Poisson's ratio using $G(t)$ and $K0$ 112

Figure 58 $G(t)$ and Kt master curves calculated based on the Poisson's ratio $\nu 0 = 0.3$ using Eq. (85) 113

Figure 59. Master curves for EMC - E, G, K and ν 116

Figure 60 A schematic illustration relaxation modulus at various cure-extents 118

Figure 61 A schematic illustrating crosslinking process in a polymer during curing ($p1 < p2 < p3$) [125] 119

Figure 62 Horizontal shifting of the normalized master curves (shape functions) on the $\log t$ scale using time-cure superposition (TCS) 120

Figure 63 Volume change of fully-cured EMC in different temperature and pressure for P-V-T measurement [14] 122

Figure 64 Schematic of the shear clamps used for EMC testing [14] 123

Figure 65 Temperature profile and measured stiffness values during various ramping testing for different degrees of cure. 124

Figure 66 Storage modulus master curves at various cure extents 125

Figure 67 Normalized shear modulus master curves. 126

Figure 68 Shift-factor related to shear modulus master curves 126

Figure 69 Cure-dependency of the shear rubbery plateau. Fittings are based on Martin and Adolf theory. 127

Figure 70 (a) Master curves at various cure states referenced at a test temperature of 23°C, (b)super-master curve generated by normalizing and horizontally shifting the data in (a) [80] 129

Figure 71 Experimental values of equilibrium modulus vs. Adolf and Martin model [69] 130

Figure 72 Poisson's ratio from stress relaxation testing of samples at various cure states [76]. 131

Figure 73 Poisson's ratio vs. degree of cure (a) 100 seconds and (b) 1000 seconds [76] 132

Figure 74 Master curve of Poisson's ratio obtained with horizontal shifting [76] 133

Figure 75 Temperature profile followed in DSC to determine $Tg(p)$ of the material 137

Figure 76 Heat flow rate vs Temperature during dynamic ramping of partially cured specimens at various cure extents 138

Figure 77 Evolution of glass transition temperature - Tgp during curing..... 139

Figure 78 (a) Dielectric sensor, (b) equivalent electrical circuit model for polymer material [129]. 140

Figure 79. Experimental results of (a) D and viscosity, and (b) dD/dt and viscosity during the curing process [129] 142

Figure 80. Illustration of the (a) dielectric sensor and electrical connection and (b) measurement setup. 144

Figure 81. Result of the dissipation factor measurement, (a) dissipation factor and temperature, (b) rate of the dissipation factor change as a function of time. 145

Figure 82 Results of monotonic testing data using DMA for Young's equilibrium modulus measurements – (a)Force vs deflection data, and (b) Stress vs Strain data..... 148

Figure 83 Results of monotonic testing data using hydrostatic test setup for bulk equilibrium modulus measurements – (a) Pressure vs. output voltage strain signal and, (b) pressure vs volumetric strain. 148

Figure 84 Measured values of equilibrium moduli – (a) $E\infty(p)$ (black scatter plot) and, (b) $K\infty(p)$ (blue scatter plot) 150

Figure 85 Comparison of $E\infty(p)$ data with the percolation model fitting 151

Figure 86 Comparison of $G\infty(p)$ data with the percolation model fitting 153

Figure 87 Plot of evolution of viscoelastic functions with cure extent 154

Figure 88 Cumulative heat released as a function of time obtained from DSC experiment 155

Figure 89 Diffusion function (fd) for various cure temperatures (Tc) obtained for the isothermal data – (a) Plot of $-lnfd$ vs. $\Delta Tg(p)$ and (b) comparison data vs prediction of diffusion function (fd) vs ΔTgp 157

Figure 90 Comparison of model prediction (diffusion and chemical control) with isothermal DSC test data at 90°C 158

Figure 91 Raw storage modulus data of MFT sweeping tests conducted on partially-cured EMC specimen from $p = 0.6$ to $p = 0.9$ 160

Figure 92 MFT results – master curves after shifting at $Tref = -40°C$ 161

Figure 93 Normalized master curves for partially-cured EMC at $Tref = -40°C$ 162

Figure 94 Results of TCS shifting – (a) Master curve after overlap, and, (b) Cure-dependent shift-factors ($\log ap(p)$) 162

Figure 95 $\log aT$ calculated while generating master curves for the partially-cured specimens tested 164

Figure 96 Comparison of stress relaxation results obtained from FEM vs. analytical solution – (a)$p = 0.9$, and (b) $p = 0.7$ 168

Figure 97 Schematic of a TFBGA package used in the FEM model 168

Figure 98 Mold pressure profile used in the FEM model 169

Figure 99 Model conditions - (a)Boundary conditions applied on the model and (b) Meshed model 169

Figure 100 Warpage of the TFBGA package during and after molding process 170

Figure 101 Warpage at various stages during and after molding processes – (a) Before demolding – 0 μm, (b) just after demolding – 50 μm, and (c) after complete relaxation (600 seconds) – 155 μm. 172

Chapter 1 Introduction

1.1. Motivation

Molding processes produce residual stress in encapsulated components. They are combined with the stresses caused by the coefficient of thermal expansion (CTE) mismatch to dictate the final warpage at room and reflow temperatures, which must be controlled for fabrication of RDL as well as yield during assembly.

With advanced computational mechanics techniques and computing hardware, one can model any kind of semiconductor package for complex loading and boundary conditions. However, it is still difficult to make quantitative prediction of residual stresses/ warpages after molding process.

The reason for this is that some critical properties are missing during the prediction. To compensate for the missing properties, commercially available warpage measurement tools such as shadow moiré, projection moiré, digital image correlation (DIC), etc., have been employed, through which the simplified material properties are adjusted until numerical predictions have reasonably good agreement with displacement measurements.

Unfortunately, the calibrated models often do not produce accurate warpage predictions for different package architectures using the same epoxy molding compounds (EMCs) - "architecture-dependent" modeling, which is defined as "a model that works for a specific packaging design but does not work for different designs using the same material sets". If accurate

material properties are employed, however, the prediction accuracy should remain the same regardless of the package architectures - "authentic material-based modeling".

During molding process, EMC is continuously curing and the mechanical properties continue to evolve; more specifically, the equilibrium modulus and the relaxation modulus. The former defines behavior after complete relaxation while the latter describes the transient behavior. It is thus necessary to measure cure-dependent viscoelastic properties of EMC to be able to determine mold induced residual stresses accurately. This is the motivation for this thesis.

1.2. Objectives

The objective of this thesis is to develop techniques and methodologies to be able to characterize cure-extent dependent viscoelastic behavior of epoxy molding compound (EMC). The goal of this characterization is to be able to predict residual stress and deformations induced in EMC by molding processes. Achieving the objective entails:

a) Characterizing the cure-kinetics of EMC in both diffusion and chemical controlled regions; considering that it is essential to know the cure-extent of EMC to be able to understand how mechanical properties of EMC evolve during the curing process.

b) Develop methodologies to determine the comprehensive viscoelastic behavior by measuring two time-temperature viscoelastic constants – Young's relaxation modulus ($E(t,T)$) and bulk relaxation modulus - $K(t,T)$ of fully-cured EMC. These properties are required for developing master curves for partially-cured EMC as well as stress prediction after curing has completed.

c) Development of methodologies to characterize cure-extent dependent viscoelastic behavior of EMC by – (1) measurement of equilibrium moduli - $E_\infty(p)$ and $K_\infty(p)$,

and (2) validation of the assumption of time-cure superposition (TCS) and determination of cure-dependent shift-factors ($\log a_p(p)$) for various cure extents (p).

d) Implementation of cure-extent dependent viscoelastic behavior into a commercial FEM module to be able to predict evolution of stresses and deformations of electronics packages during and after molding processes.

1.3. Organization of Dissertation

The dissertation consists of 8 chapters. Chapter 1 presentation the motivations of the work and the lists the main objectives.

Chapter 2 introduces the background of the dissertation. This chapter reviews the effect of critical EMC properties on warpage behavior. Based on the data and the analyses reported in the literature, the chapter addresses the causes that make the prediction of warpages still difficult. A literature review on current understanding of cure-dependent viscoelastic behavior is discussed and gap in the literature is identified. This chapter has been published in the special edition of *Microelectronics Reliability* journal in 2022.

Chapter 3 presents a deterministic approach to quantify cure kinetics of polymers using a Kamal-Sourour (KS) autocatalytic model. An analytical solution based on the reaction equations has been developed. Minimum number of tests required for accurate quantification have been identified and a simple set of equations which can be solved using a standard spreadsheet software have been derived. This chapter has been published in the *IEEE Transactions on Components, Packaging and Manufacturing Technology (CPMT)* journal in 2024.

Chapter 4 presents a novel method to determine autocatalytic cure kinetics constants of advanced thermosets with dual-reaction peaks. Commercial polymer formulations are often

tailored to match the industry requirements and advanced thermosets are being developed with multi-reaction systems to achieve this. This chapters utilizes non-linear regression tools and provides a procedure for initial guess values for the optimization program to be able to determine the cure kinetics of such dual-reaction systems accurately. This chapter has been submitted to *Journal of Materials Science and Engineering B* and is currently under a review process.

Chapter 5 presents a new test setup and a novel procedure to determine viscoelastic bulk behavior of EMC using hydrostatic testing. The methodology combines the advantage of direct strain measurement along with constitutive equations of linear viscoelasticity (LVE) to determine master curves (Prony series) of bulk modulus directly from the time-dependent pressure and strain data.

Chapter 6 discusses the equations and numerical methods for interconversion of viscoelastic properties using the measured (E, K) to obtain (G, K) required for FEM modeling based on the constitutive equations.

Chapter 7 presents methodologies for complete characterization of cure-extent dependent viscoelastic behavior of EMC. Using the measured properties, the cure-extent dependent viscoelastic behavior has been implemented into a commercial FEM software (ANSYS) to predict residual stresses/ warpages of electronics packages during and after molding process.

Chapter 8 contains a summary of contributions made by this study and a discussion for the future studies that can be extended from the present study.

Chapter 2 Effect of Critical Properties of Epoxy Molding Compound on Warpage Prediction: A Critical Review

2.1. Introduction

Residual stresses exist inherently in components encapsulated by molding processes. They are combined with the stresses caused by the coefficient of thermal expansion (CTE) mismatch, and eventually dictate the final warpage of components at room and reflow temperatures.

The warpage history of a package during manufacturing is illustrated schematically in Figure 1, where transfer molding is considered. The package bends upward (∪) after molding (Figure 1 (a)), at the mold temperature, because the epoxy molding compound (EMC) shrinks during molding. When the package is heated to the reflow temperature after molding, the CTE mismatch causes the package to bend downward (∩), because the CTE of EMC at the peak reflow temperature is typically higher than those of adjacent materials (Figure 1 (b)). Obviously, both quantities (cure shrinkage and CTE induced thermal strains) are required to accurately predict the warpage at the peak reflow temperature.

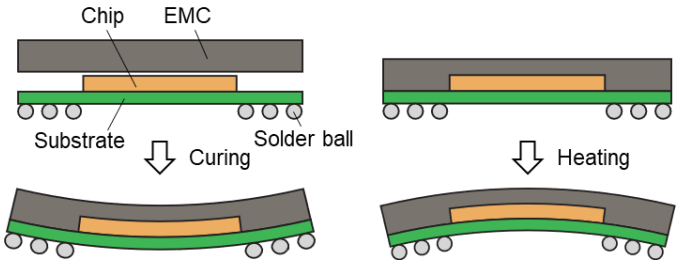
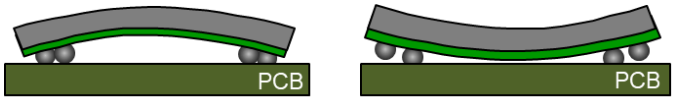


Figure 1 Schematic illustration of a package warpage history: warpage caused by (a) transfer molding; and (b) heating the package from mold temperature to reflow temperature.

The original problem definition of warpage involved controlling the warpage of a single component at the solder reflow temperature. In those applications, the printed circuit board (PCB)

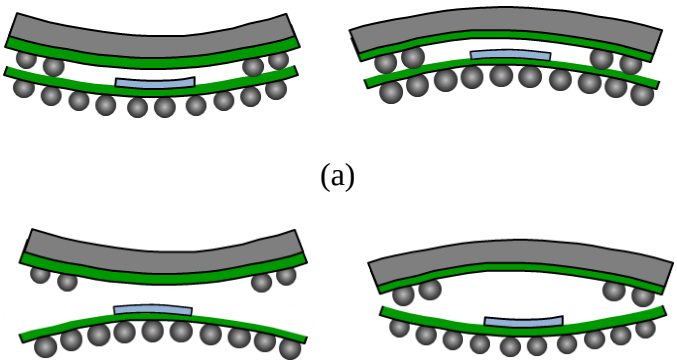
was relatively thick, and it was reasonable to assume that the PCB was flat at the reflow temperature considering the symmetric design of signal planes with respect to the power plane at the center. Thus, the component warpage simply had to be controlled not to exceed certain specifications (relative to solder ball sizes) and thus to avoid solder bridging or opening during the assembly process, as illustrated in Figure 2.



(a) (b)

Figure 2 Illustration of (a) solder bridging and (b) solder opening during board level assembly

The warpage issue became more challenging, when the portable electronics industry, adopted the package-on-package (PoP) technology. In typical mobile phone applications, a top package (typically low I/O memory module) is stacked on a bottom package (typically high I/O logic module) using solder balls. Naturally, the packaging requirements of the two packages are different (e.g., wire-bond vs. flip-chip), and so are their thermomechanical behaviors, i.e., warpage. In order to accommodate this inherent warpage behavior difference, the warpage of both packages have to be controlled simultaneously to offer a desired stacking yield. The desired and undesired warpage combinations are illustrated in Figure 3 (a) and (b), respectively.



(a)

(b)

Figure 3 Illustration of (a) desired and (b) undesired warpage combinations in PoP stacking.

More recently, the warpage issue became even more challenging simply because EMCs became a part of some interconnect systems in various heterogeneous integration solutions, including fan-out wafer level packaging (FO-WLP) and embedded technologies, where vias and signal redistribution layers are fabricated in or on EMC after molding is completed [1-6]. The wafer level warpage of FO-WLP at room temperature is illustrated in Figure 4, which can be excessive due to a large wafer size. This must be controlled for successful process integration (e.g., fabrication of redistribution layer) after molding is completed.

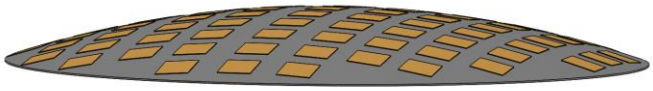


Figure 4 Illustration of the warpage of FO-WLP wafer at room temperature

For the past couple of decades, extensive efforts have been made to enhance the predictability of warpage. On the modeling front, commercial software packages are equipped with advanced but user-friendly analysis modules. As a result, even non-experts can model/simulate almost any kind of electronic packaging products. On the experimental front, thermo-mechanical properties required for numerical predictions, including CTE, the glass transition temperature (T_g), and the temperature-dependent viscoelastic properties, are routinely measured by commercial tools such as thermo-mechanical analyzer (TMA) and dynamic mechanical analyzer (DMA). In addition, temperature-dependent warpage can be measured readily using commercial shadow Moiré and digital image correlation (DIC) tools, and the results are used for model validation.

It is worth mentioning that an in-plane displacement measurement technique, called Moiré interferometry, was first used to verify the validity of complex numerical models [7, 8]. It is very effective in validating the constitutive relationships of various materials used in the package quantitatively. However, it has not been the most preferred choice for the verification of warpage prediction. Besides the complex experimental procedure, including sample preparation, the method produces relative deformations with respect to a reference (or assumed stress-free) temperature. This is ideal for a stress-analysis, but not most desired for a warpage analysis that requires an absolute stress state inside a package.

Due to its simplicity, shadow Moiré has been used most extensively to verify the validity of warpage prediction models. Some studies in the literature show excellent agreements between measurements and predictions [9, 10]. Yet even this verified model often does not predict accurately the warpage of different packages molded by the same EMC. In fact, good agreements between warpage predictions and measurements are possible even when the properties of EMC are not correct and/or some critical properties of EMC are missing. It is attributed partly to the fact that the warpage, i.e., the out-of-plane displacements of a traction-free top and/or bottom package surfaces should have a continuous and smooth field regardless of the complexity of underlying geometries and materials.

An attempt to investigate the reasons for the above paradox, i.e., why accurate warpage prediction is still difficult even with (1) temperature and time-dependent EMC properties and (2) numerical models verified by the experimentally measured warpage of actual packages, is the motivation of this review article.

Based on the data and the analyses reported in the literature, the paper addresses three potential causes related the physical properties of EMC, which make the prediction still a

challenging task. The causes are discussed in detail considering two most widely used molding processes, i.e., transfer molding and compression molding. The issue associated with EMC cure shrinkage will be discussed in Section 2.2. The improper assumptions used in the current practice of viscoelastic analysis will be discussed in Section 2.3. Section 2.4 will be devoted to unique challenges associated with cure-extent dependent viscoelastic properties. Some recommendations and future studies will be discussed in Section 5.

2.2. Effective Cure Shrinkage (ECS)

Numerical stress analyses are typically performed to determine relative changes of stresses with respect to a reference condition, where stresses are assumed to be zero. Warpage prediction, however, requires determination of the "absolute" stress state inside a package, which must include residual stresses caused by molding processes, more specifically, cure shrinkage-induced stresses.

CTE mismatch-induced stresses are generally much larger than cure shrinkage-induced stresses, and thus the latter is not so critical if warpage at room temperature is concerned, e.g., warpage of FO-WLP at room temperature directly affects the fabrication process of redistribution layer (RDL). Warpage caused by the latter is still very important for thin packages, especially, those used in portable devices, for which warpage at reflow temperature affects assembly yield significantly. This section discusses how to measure the cure shrinkage to be used for process-induced residual stresses.

2.2.1. Cure kinetics

EMC is based on thermosetting polymers. They are solidified through a chemical reaction that causes polymer chains to cross-link. The general form of a curing rate can be expressed as:

$$\frac{dp}{dt} = k_c(T,p) \cdot \phi(p) \tag{1}$$

where p is the cure-extent (or degree of cure); k_c is a temperature and cure dependent rate coefficient; and $\phi(p)$ is the cure kinetic function that can take any mathematical form of p.

The rate coefficient can take several functional forms. In the well-known n^{th} order model, the rate coefficient is only temperature dependent, and the curing rate is given by [11]:

$$\frac{dp}{dt} = k_c(T) \cdot p^m(1-p)^n;\ k_c(T) = A_0 \exp\left(-\frac{E_a}{RT}\right) \tag{2}$$

where k_c is the rate constant, E_a is the activation energy, R is the universal gas constant and n is the reaction order. In an autocatalytic reaction, the rate coefficient is dependent on both temperature and cure, and the curing rate is given by [11]:

$$\frac{dp}{dt} = k_c(1-p)^n; k_c(T,p) = k_1(T) + k_2(T)p^m \tag{3}$$

where $k_1(T)$ and $k_2(T)$ are rate constants which are temperature-dependent, and m, n are reaction orders. More details about cure kinetics and rate functions can be found in Ref. [11].

The modified autocatalytic model or Kamal-Suror's model has been known to describe well the curing behavior of several EMCs [12-14]. The model is given as:

$$\frac{dp}{dt} = k_0 \cdot p^m(1-p)^n \tag{4}$$

where k_0 is the rate constant and m, n are reaction orders.

2.2.2. Measurement of ECS

During solidification, each cross-linking causes incremental volumetric shrinkage, known as cure shrinkage. Numerous testing methods have been developed over the span of many decades,

and some of them are practiced routinely to measure the intrinsic (or total) cure shrinkage [15-22]. The cure shrinkage, ε, is proportional to the extent of cure as:

$$\varepsilon(p) = \varepsilon_{\infty}^{ch}\phi(p) \tag{5}$$

where $\varepsilon_{\infty}^{ch}$ is the total cure shrinkage that is accumulated during the entire curing process.

The behavior of a typical polymer system is illustrated in Figure 5, where the *x*-axis shows time axis, *t* (with arbitrary unit) , and the *y*-axis represents two polymer properties associated with curing (cure shrinkage, $\varepsilon(t)$, and shear modulus, $G(t)$), normalized by their equilibrium values, ε_{∞} and G_{∞}, obtained after curing is completed.

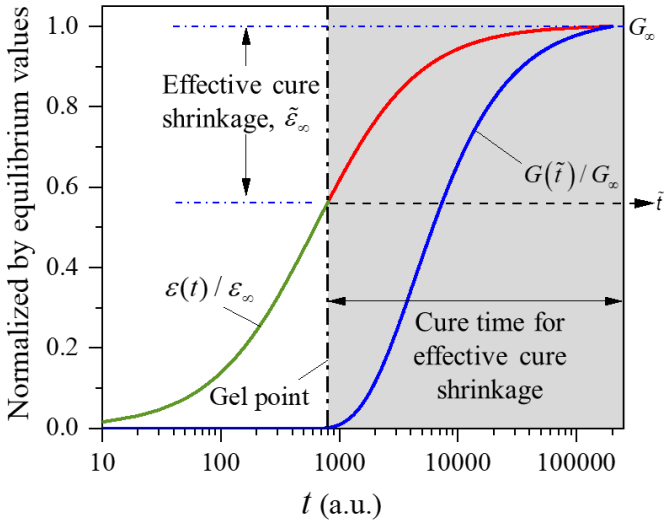


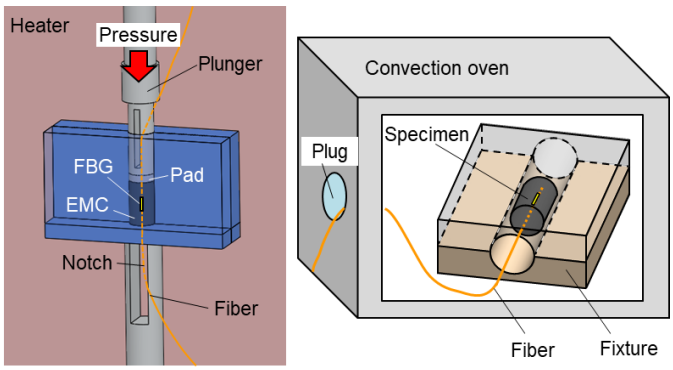
Figure 5 Evolution of cure shrinkage and modulus during curing

As mentioned earlier, cure shrinkage does occur before the gel point (denoted as p_{gel}). However, the modulus associated with the cure shrinkage developed before the gel point is virtually "zero", and it does not contribute to residual stresses. The cure shrinkage that occurs after the gel point has been defined as the "effective cure shrinkage (ECS)" [23-25] to distinguish it from the "total cure shrinkage". The ECS value should be used for calculation of cure-induced residual stresses. In the figure, the ECS amount is denoted by $\tilde{\varepsilon}_{\infty}$.

Unlike classical methods to measure the total shrinkage where only a volume change after curing has to be documented, a technique to measure the effective cure shrinkage should satisfy two critical requirements since the gel point must be identified accurately: (1) a stress-induced strain can be measured directly while curing occurs; (2) a strain sensor employed in the technique should be so robust not to be degraded by polymers and volatiles as well as harsh curing conditions (temperature, pressure, etc.).

A fiber Bragg grating (FBG) is an optical strain sensor that offers very high sensitivity ($\approx 1\mu\varepsilon$). It is extremely robust, as it is fabricated on a glass fiber. The ECS can be measured by embedding an FBG sensor inside EMC. The FBG-based technique was developed to estimate residual stresses [26-28] in composite structures, and it has been implemented successfully to measure the ECS values of various polymers [23-25].

A unique challenge is encountered during the ECS measurement of EMC. Large friction between EMC and mold inner surfaces occurs inevitably during mold pressure application, which hinders EMC from contracting freely during curing. Recently a novel idea involving two-stage curing has been conceived to cope with the problem [29]. A setup used to measure ECS is shown in Figure 6 [29]. In the first stage, an FBG sensor is embedded in EMC by a molding process (Figure 6 (a)). The FBG-EMC assembly is separated from the mold and the molded specimen is heated to a cure temperature rapidly in the second stage (Figure 6 (b)). This procedure ensures constraint-free curing, and thus, accurate measurement of ECS. The Bragg wavelength (BW) change is measured continuously until no noticeable change is observed.



(a) (b)

Figure 6 Schematic illustration of a setup used to measure the effective cure shrinkage of EMC: (a) application of the mold pressure to collapse an EMC pellet; and (b) curing the FBG-embedded EMC specimen inside a constraint-free fixture.

The results are shown in Figure 7, where the EMC strain is plotted as a function of time, normalized by the total curing time. It is important to note that the strain was zero for a short initial period, as shown in the inset. This is a clear indication that the FBG responded only after the gel point. The ECS value was 0.077%.

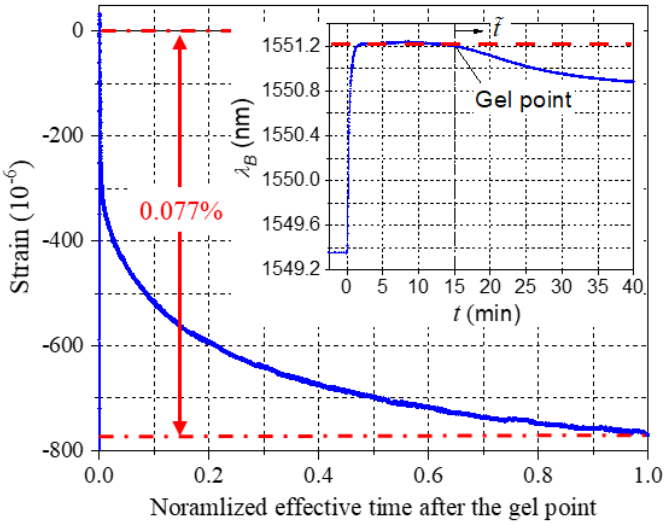


Figure 7 Effective cure shrinkage of EMC as a function of normalized time where the inset shows the BW signal of initial 40 min.

2.2.3. Transfer molding and compression molding

Two most widely used molding technologies are transfer molding and compression molding. Transfer molding was implemented first for various wire bond packages. More recently, compression molding was adopted for more advanced packages such as higher I/O packages and fan-out wafer (or panel) level packages.

Transfer molding is different from compression molding in that it forces EMC into an enclosed mold containing numerous cavities. Transfer molding typically uses a higher mold pressure to ensure uniform fill of mold cavities through narrow channels. For this reason, EMC inside mold cavities is under a completely different state of deformation after the molding process, compared to compression molding. These different deformation states of EMC should be simulated properly for accurate prediction of the residual stress caused by each molding process.

The transfer molding process is illustrated schematically in Figure 8. An EMC pellet is charged, and the mold is heated to a mold temperature. Then, a molding pressure is applied to transfer the charge from a transfer pot to cavities containing electronic packages, as shown in (a). The molding compound is driven through narrow channels called “runners”, which connect the transfer pot to the gates of cavities. During its transfer, the molding compound remains as a viscous liquid, and thus the molding pressure is transferred to all cavities, as illustrated in (b).

At the mold temperature, the molding compound cures rapidly, and quickly passes its gel point, at which the molding compound becomes a deformable solid. As a result, the pressure to fill the cavities is no longer transferred to the molding compound in the cavities after the gel point, as illustrated in (c), although the pressure is maintained until the mold is opened for removal of the encapsulated components. Therefore, the warpage of the components after the transfer

molding is caused solely by the cure shrinkage of the molding compound accumulated after the gel point, i.e., the effective cure shrinkage.

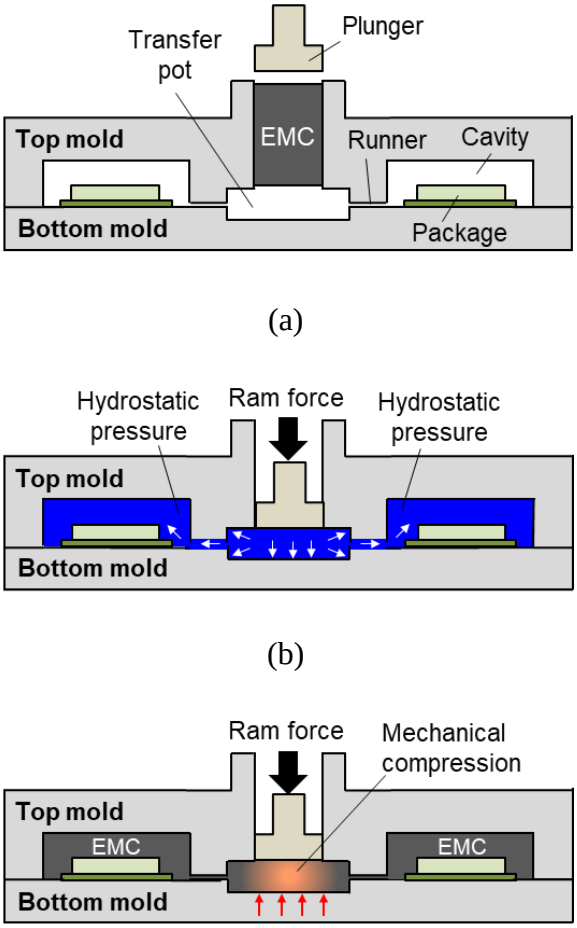


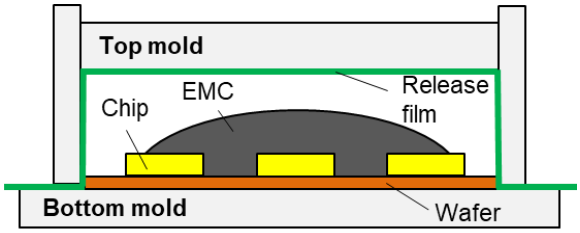
Figure 8 Schematic illustration of transfer molding process: (a) EMC is charged, and the mold is heated to the mold temperature; (b) EMC remains as a viscous liquid during EMC transfer (before EMC passes its gel point); and (c) EMC becomes a deformable solid as soon as EMC passes its gel point.

It is important to recall that during molding; the modulus evolves nonlinearly (Figure 5). A different set of cure-extent dependent material functions are required to predict cure-induced warpage after molding. It is inevitable that the ECS values and the cure-extent dependent

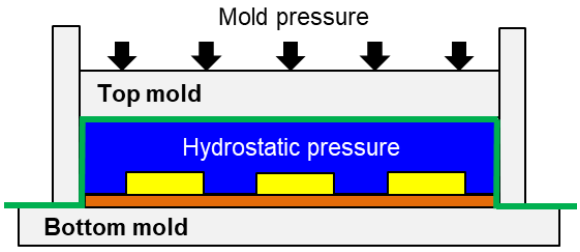
viscoelastic properties must be used be accurately predict warpage after transfer molding. Yet, these properties have not been characterized properly, and thus not readily available.

A typical compression molding process is illustrated schematically in Figure 9. The mold containing various forms of EMC (powder, granular, liquid, pellet, etc.) is heated first to the mold temperature (a); EMC remains as a viscous liquid during initial compression (b); and EMC becomes a deformable solid as soon as EMC passes its gel point (c).

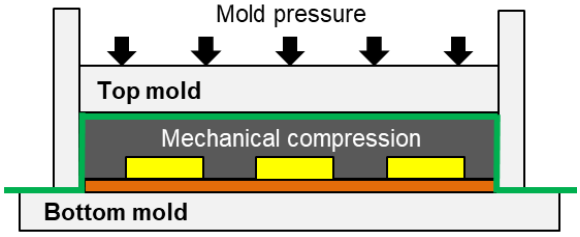
Unlike transfer molding, the mold pressure is continuously applied to EMC until the mold is opened during compression molding. As soon as it becomes compressible, i.e., from liquid (b) to deformable solid (c), EMC deforms continuously due to the mold pressure (nearly hydrostatic compression). Again, it seems impractical to predict warpage after compression molding without the ECS values and the cure-extent dependent viscoelastic properties. The cure-extent dependent properties will be discussed in detail in Section 4.



(a)



(b)



(c)

Figure 9 Schematic illustration of compression molding process: (a) EMC is charged, and the mold is heated to the mold temperature; (b) EMC remains as a viscous liquid during EMC transfer (before EMC passes its gel point); (c) EMC becomes a deformable solid as soon as EMC passes its gel point, and the pressure continuously deforms EMC until the mold is opened.

2.2.4. Discussion: Mold shrinkage

The mold shrinkage is defined to be the difference between the dimensions of the mold and the molded part at room temperature [30]. It is intended to provide a dimensional change at room temperature caused by the mold process. Typically, the mold shrinkage is measured using a standard cavity. As illustrated in Figure 10, the mold shrinkage (%) is defined as [31]:

$$MS(\%) = \frac{D-d}{D} = \left(\varepsilon_{ch}^{total} + \alpha_1\left(T_g - T_{room}\right) + \alpha_2\left(T_c - T_g\right) - \alpha_m\left(T_c - T_g\right)\right) \quad (6)$$

where $MS(\%)$ is mold shrinkage in %. D is the diameter of the mold at room temperature; d is the diameter of a cured EMC specimen at room temperature; ε_{ch}^{total} is the total volumetric shrinkage of EMC, α_1 and α_2 are the CTE values of EMC below and above T_g, respectively; α_m is the CTE value of the mold; and T_c and T_r are cure temperature and room temperature, respectively.

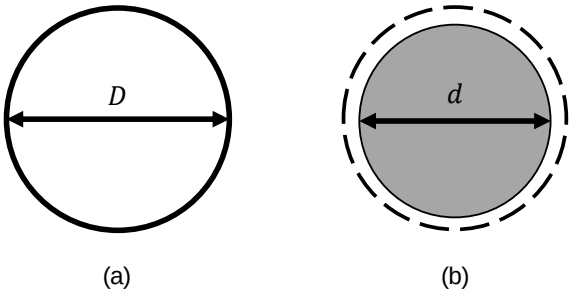


Figure 10 Illustration of the dimensions of (a) cavity at room temperature and (b) molded EMC at room temperature

In transfer molding, the difference between the dimensions of the mold and of the molded article produced therein from a given material vary according to the design and operation of the mold. It is affected by the size and temperature of the pot or cylinder and the pressure on it, as well as on mold temperature and molding cycle [31, 32].

Therefore, the mold shrinkage should not be used to predict the residual stresses at the mold temperature simply because it contains the effect of the coefficient of thermal expansion (CTE) of the mold as well as the cured thermoset polymers. The ECS value obtained from Figure 7 is approximately only 43% of the mold shrinkage provided by the EMC manufacturer.

2.3. Time and Temperature Dependent Behavior of Polymers

There is an abundance of literature that concerns numerical prediction of warpage. They can be categorized into temperature dependent linear elastic analyses [33-36] and linear viscoelastic analyses [9, 10, 37-40]. It is to be noted that only few representative papers are cited in this paper due to space limitation. Thermal excursions used in the analyses usually exceed the glass transition temperature (T_g) of EMC, and thus it is inevitable to use the temperature-dependent properties. In most cases, however, some critical properties have been assumed to be temperature-independent or were just missing; more specifically, Poisson's ratio (ν) in linear elastic analyses, and the bulk modulus (K) in viscoelastic analyses. Considering the current trend, this section discusses only the improper assumption used in the current practice of viscoelastic analyses, yet the same argument can be made for linear elastic analyses without losing generality.

2.3.1. Linear viscoelasticity

The constitutive law of linear viscoelasticity is written as [41]**:**

$$s_{ij} = 2\int_{0^+}^{t} G(t-\tau)\frac{\partial e_{ij}(\tau)}{\partial \tau}d\tau$$
$$\sigma_{kk} = 3\int_{0^+}^{t} K(t-\tau)\frac{\partial \varepsilon_{kk}(\tau)}{\partial \tau}d\tau \quad (7)$$

where s_{ij} and e_{ij} are the deviatoric stress and strain tensors, respectively. $G(t)$ and $K(t)$ are the time-dependent shear modulus and bulk modulus, respectively, and σ_{kk} and ε_{kk} are the dilatational (or volumetric) stress and strain tensors, respectively.

In the linear viscoelastic regime, two constants (E, ν) have the following relationship with the other two constants (G, K) in the Laplace domain as [42]:

$$\bar{G}(s) = \frac{\bar{E}(s)}{2[1 + s\bar{v}(s)]}; \bar{K}(s) = \frac{\bar{E}(s)}{3[1 - 2s\bar{v}(s)]} \quad (8)$$

where $\bar{E}(s), \bar{v}(s), \bar{G}(s)$ and $\bar{K}(s)$ are Young's modulus, Poisson's ratio, shear modulus and bulk modulus in the Laplace domain, respectively. For the numerical modeling, two of the four constants must be measured experimentally.

Conversion from the time-domain to the Laplace domain is usually simple. However, converting back from the Laplace domain to the time domain requires complex integral functions, and involves computationally heavy numerical solutions. Several approximate solutions for interconversion are available in the literature, and they are summarized in Ref. [42-44].

For thermorheologically simple (TRS) polymers, the viscoelastic behavior at one temperature can be related to that at another temperature only by a change in the log time scale [45]. This has been illustrated in Figure 11, where the relaxation modulus (or master curve) at various temperatures can be obtained only by shifting the master curve obtained at a reference temperature on a log time scale. Glassy modulus (G_G) is defined as the point on the relaxation curve where the molecular chains are frozen, and no relaxation can occur. This is also referred to as G_0 or relaxation modulus at the fictive time "0" after application of an instantaneous load. The shape of the master curve at any temperature remains the same and can be shifted to a reference temperature (T_{ref}) using temperature dependent shift factor, a_T. At temperature T_1 greater than T_{ref}, the relaxation rate is faster and at temperature T_3 less than T_{ref} the relaxation rate is slower as evident from Figure 11.

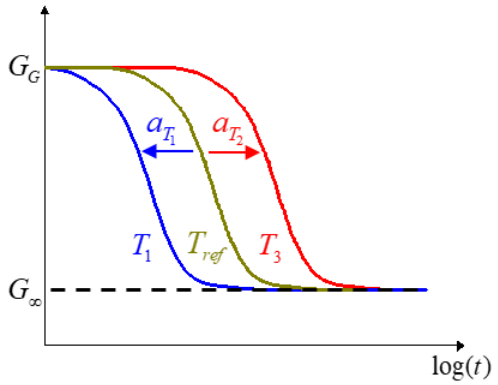


Figure 11 Illustration of the material behavior of TRS polymers

This is known widely as time-temperature superposition (TTS). The master curve at the reference temperature shown in Figure 11 can be expressed using the Prony series:

$$G(t) = G_\infty + \sum_{i=1}^{N} G_i \exp\left(-\frac{t}{\tau_i}\right) \tag{9}$$

The master curves at arbitrary temperature can be expressed using the reduced time as:

$$G(\psi) = G_\infty + \sum_{i=1}^{N} G_i \exp\left(-\frac{\psi}{\tau_i}\right) \tag{10}$$

where G_i are Prony shear constants; τ_i are relaxation time constants; and $\psi(t)$ is the reduced time. The reduced time is defined as:

$$\psi(t) = \int_0^t \frac{d\xi}{a_T(T)} \tag{11}$$

where $a_T(T)$ is the temperature-dependent shift-factor.

It is impractical to measure the entire master curve in a single experiment due to the large time range involved in the master curve. Instead, the relaxation tests are conducted at various temperatures for short periods of time. The data are then shifted to a reference temperature to

create a single master curve and obtain shift factors (a_T). This routine practice is illustrated in Figure 12

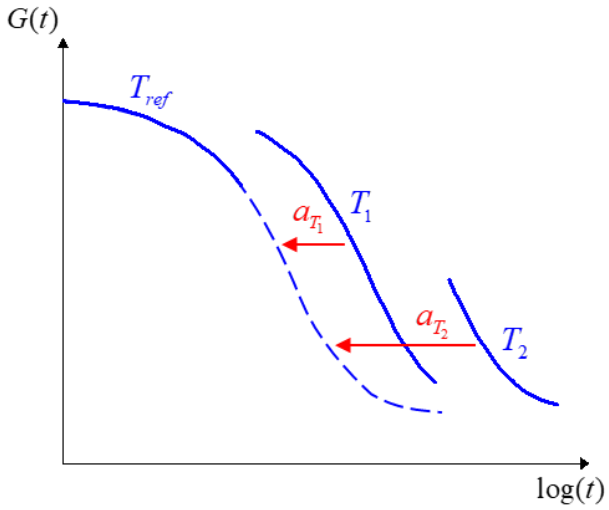


Figure 12 Procedure to create a master curve and to obtain shift factors using the TTS principle

Dynamic mechanical analysis has also been used extensively to measure the relaxation behavior of polymers. Dynamic mechanical analysis essentially involves measuring the stress/strain relationship while applying a cyclic strain ($\gamma(t)$) at a known frequency (ω). For viscoelastic materials, a phase lag (δ) exists between the applied cyclic strain and the cyclic stress response ($s(t)$) due to dissipation of the elastic energy through chain relaxation. The ratio of the cyclic stress to strain is called complex modulus ($\hat{G}(\omega)$). The relationships are known as [46]:

$$\begin{aligned} \gamma(t) &= \gamma_0 \cos(\omega t) = \gamma_0 Re\left[e^{i\omega t}\right] \\ s(t) &= s_0 \cos(\omega t + \delta) = s_0 Re\left[e^{i(\omega t+\delta)}\right] \\ \hat{G}(\omega) &= \frac{s(t)}{\gamma(t)} = s_0/\gamma_0 Re[\cos\delta + i\sin\delta] \end{aligned} \tag{12}$$

Additionally, complex modulus is expressed as a (pseudo-) vector sum of two components, storage modulus (G'- real) and loss modulus (G''- imaginary). Mathematically,

$$\hat{G}(\omega) = G'(\omega) + i\, G''(\omega) \tag{13}$$

where G' represents the storage modulus (or stored energy) and G'' represents the loss modulus (or dissipated energy) in a cycle.

Commercially available machines based on the analysis (dynamic mechanical analyzer: DMA) are routinely used to measure the relaxation modulus of polymers. A polymer is tested by applying a cyclic strain over a range of frequencies typically between 0.1 - 100 Hz at several temperature intervals (multi-frequency and temperature sweeps: MFT). The complex modulus is obtained by measuring the stress response for an applied sinusoidal strain at a given frequency (ω). The relationship between complex modulus and relaxation modulus is given as [47]:

$$\hat{G}(\omega) = i\omega \int_0^\infty G(s) e^{-i\omega s} ds = i\omega \mathcal{F}\{G(t)\} \tag{14}$$

where $\hat{G}(\omega)$ is the complex modulus, $G(t)$ is the relaxation modulus, and $\mathcal{F}\{\}$ is the Fourier transform.

The same TTS principle is exercised to obtain the shift factors (a_T) and the master curve in the frequency domain. The frequency domain Prony series for $G'(\omega)$ can be expressed using the relaxation time constants as [48]:

$$G'(\omega) = G_\infty + \sum_{k=1}^{N} G_k \frac{\omega^2 \tau_k^2}{1 + \omega^2 \tau_k^2} \tag{15}$$

where $(G_k; \tau_k)$ are Prony elastic constants and relaxation time constants, respectively and G_∞ is the equilibrium modulus.

An example of obtaining the relaxation modulus is shown in Figure 13. A DMA Multifrequency-temperature (MFT) sweep was conducted using a three-point bending sample to obtain the storage moduli.

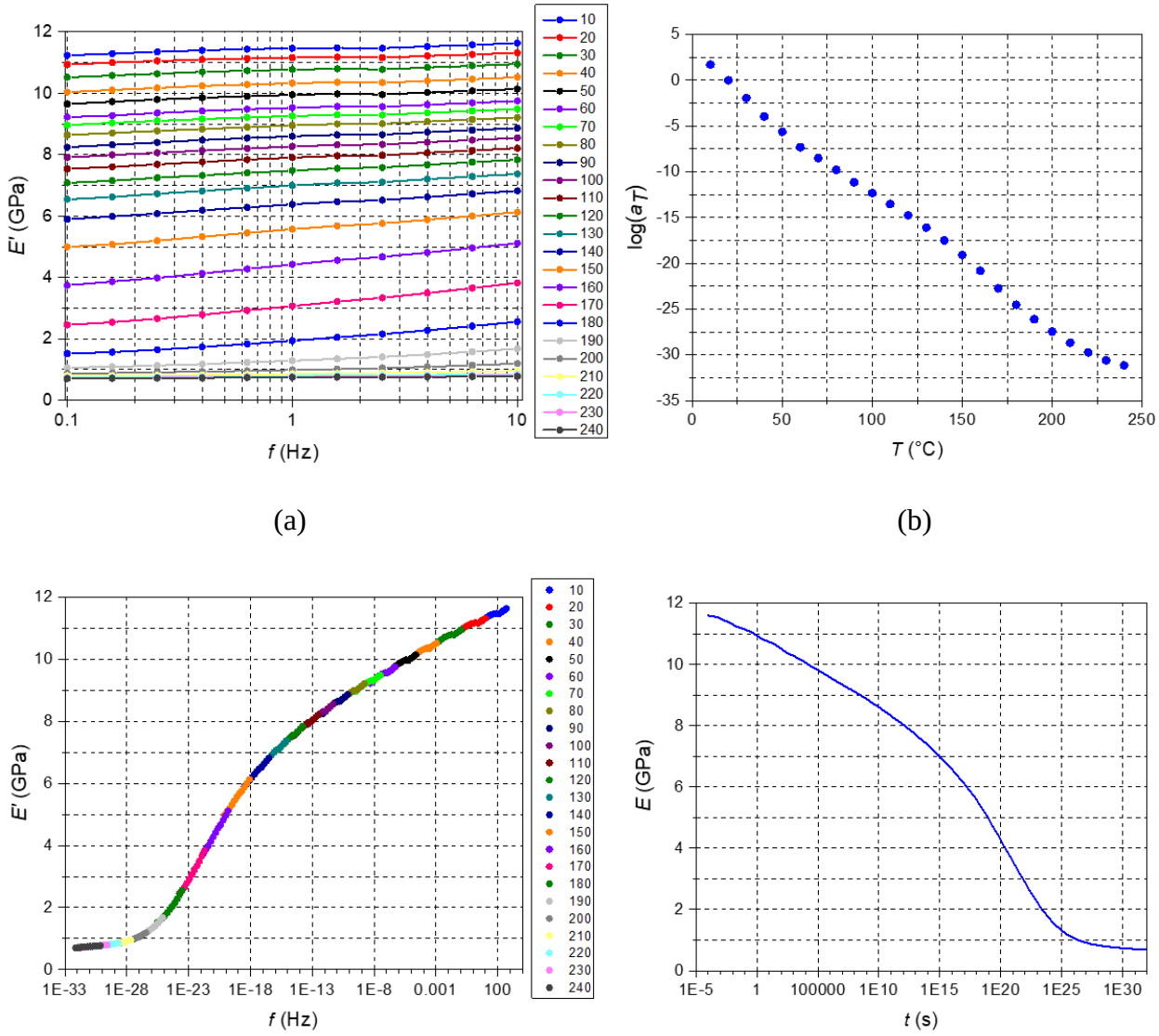


Figure 13 Representative DMA results: (a) Storage modulus obtained from the MFT sweep; (b) shift factors (a_T); (c) storage modulus master curve in the frequency domain; and (d) relaxation modulus master curve in the time domain

The storage moduli obtained from the MFT sweep are shown in (a). The shift factors (a_T) and the storage modulus master curve ($E^{'}(\omega)$) are shown in (b) and (c), respectively. The relaxation modulus master curve in the time-domain can be determined using Eqs. (10) and (11)

from the Prony series constants obtained by fitting Eq. (15) to the data in (c). The results are shown in (d).

2.3.2. Critical assumptions used in the current practice

As mentioned earlier, two master curves, $G(t)$ and $K(t)$, of EMC are required for a numerical viscoelastic analysis. Direct measurement of $G(t)$ and $K(t)$ is usually more challenging. Only limited shear moduli setups can be found in the literature [14, 49], but only the data obtained for soft polymers seem reliable because it is difficult to obtain the pure shear condition for rigid polymers [50, 51].

Time and temperature dependent Young's moduli are relatively easy to measure using the standard testing apparatuses such as DMA and universal testing machines. Two assumptions have been widely adopted to utilize the master curve of Young's modulus for a viscoelastic analysis, albeit without experimental validation. The first assumption is a constant, i.e., time and temperature "independent" Poisson's ratio [52]. With this assumption, the inverse transform of the first relationship in Eq. (8) becomes:

$$\mathcal{L}^{-1}\left[\bar{G}(s) = \frac{\bar{E}(s)}{2\left(1 + s.\frac{\nu_0}{s}\right)}\right] = G(t) = \frac{E(t)}{2(1+\nu_0)} \tag{16}$$

where ν_0 is the constant Poisson's ratio.

This simple relationship allows to convert the Young's modulus master curve obtained from DMA testing (Figure 13 (d)) into the shear modulus master curve as:

$$G(t) = \frac{E(t)}{2(1+\nu_0)} = \frac{1}{2(1+\nu_0)}\left(E_\infty + \sum_{i=1}^{n} E_i \exp\left(-\frac{t}{\tau_i}\right)\right) \tag{17}$$

where E_∞ is the equilibrium modulus; $E_k; \tau_k$ are Prony elastic constants and relaxation time constants respectively; and $G_\infty = E_\infty/2(1+\nu_0)$ and $G_k = E_k/2(1+\nu_0)$.

The second assumption is "time-independent" bulk modulus [37, 53, 54]. With this assumption, the bulk modulus is approximated as:

$$K(t) \sim K_0 = \frac{E_0}{2(1+\nu_0)} \text{ at } T = T_0 \tag{18}$$

It is worth mentioning that the assumption of "time-independent" bulk modulus implies that the bulk modulus becomes "temperature-independent" if EMC behavior follows the TRS assumption. These implications are illustrated in Figure 14.

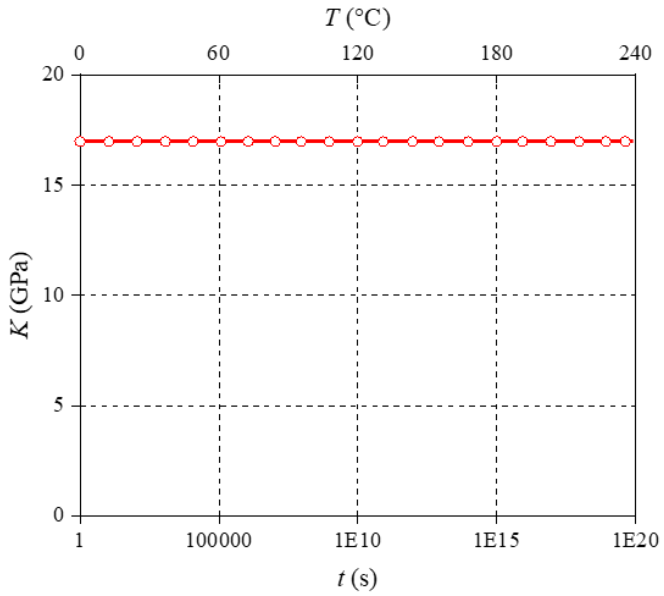


Figure 14 Implication of the assumption of bulk modulus behavior: (a) time-independent; and (b) temperature-independent behavior

When the above two approximations are implemented, i.e., only shear relaxation defined and Bulk modulus (K_0) as constant, the resultant Poisson's ratio would increase to the theoretical limit, i.e., $\nu \approx 0.5$, and thus incompressible, which could produce unreasonable results [52]. To circumvent this unrealistic mechanical behavior of EMC, two Poisson's ratios - below and above

T_g - can be considered, which produce two bulk moduli [55]. However, this approach deviates from the first assumption (the constant Poisson's ratio), and caution should be exercised when the approximated viscoelastic solutions are sought, based on the above assumptions.

2.3.3. Measurement of bulk modulus

There were several attempts to measure the bulk modulus of polymer [56] and EMC [57] by a high-pressure dilatometer [56, 57]. The system is illustrated schematically in Figure 15. In this method, the volume change was monitored as a function of time after the pressure was applied using a measurement piston, and the bulk compliance was determined from the volume change. It is important to note, however, that the dilatometer cannot apply true hydrostatic pressure as soon as the polymer passes its gel point, after which the polymer is no longer incompressible, i.e., $\nu \neq 0.5$. This inherent limitation makes the bulk modulus measurement difficult, although the volume change can be measured accurately.

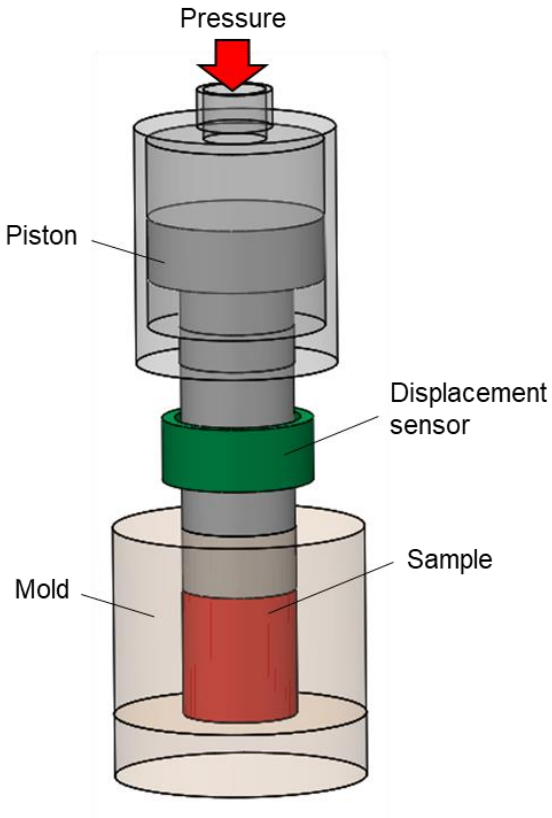


Figure 15 Schematic illustration of high-pressure dilatometer

Recently, the bulk behavior of EMC was characterized by a novel experimental technique using an embedded fiber Bragg grating (FBG) sensor [58, 59]. The FBG embedded specimen after specimen preparation and the setup used for hydrostatic testing are shown Figure 16 and Figure 17, respectively. The FBG embedded EMC specimen is placed inside a metal chamber, and it is sealed completely. The gas inlet of the chamber is connected to pressure transducer and the high-pressure cylinder through a pressure regulator.

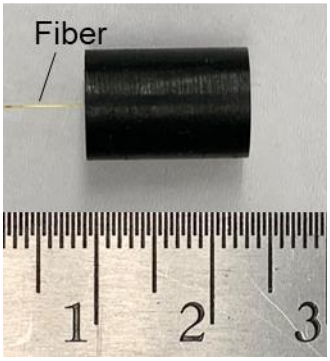


Figure 16 FBG embedded EMC specimen

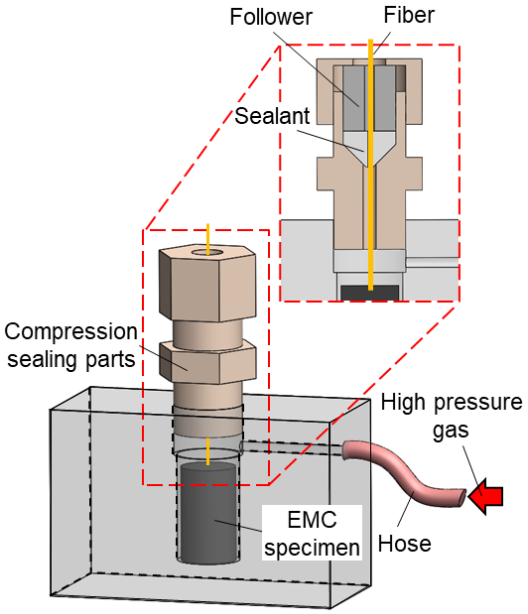
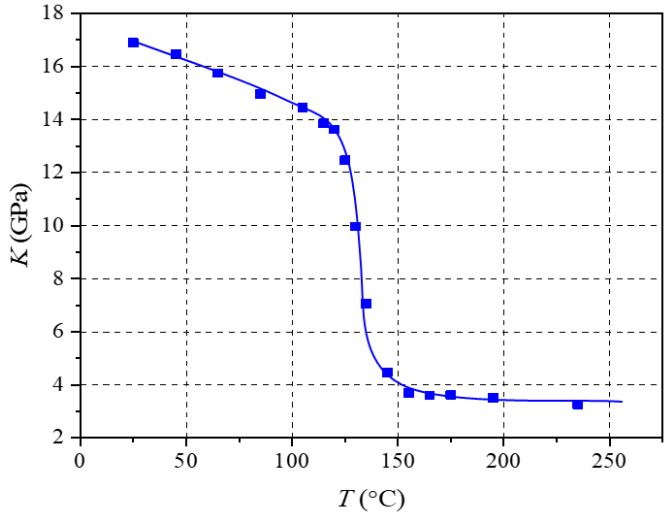
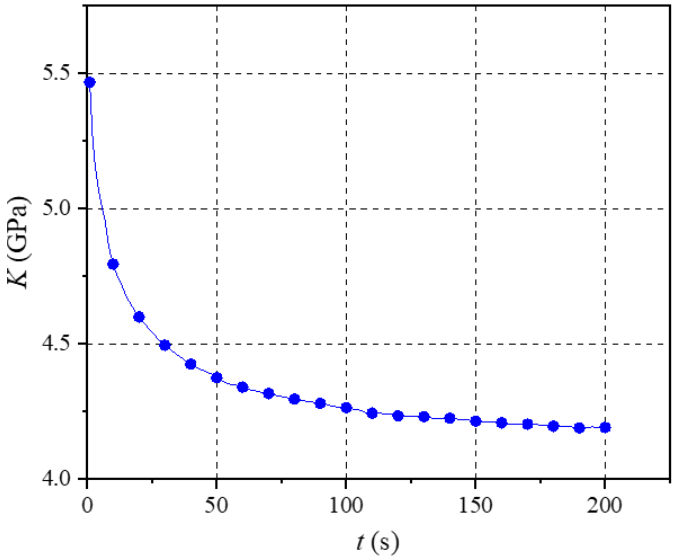


Figure 17 Schematic illustration of a setup to measure the bulk modulus

The results from the studies clearly showed strong temperature-dependent [58] as well as time-dependent bulk behavior EMC [59]. Representative results from the studies are shown in Figure 18 (a) (temperature dependence) and Figure 18 (b) (time-dependence). The dependence becomes very significant near the glass transition temperature (T_g) of EMC.



(a)



(b)

Figure 18 Bulk modulus of EMC: (a) 1 second isochronous values as a function of temperature; and (b) time-dependent values obtained at a temperature near T_g

If an absolute stress or warpage is to be predicted over a temperature range beyond T_g of EMC, it is inevitable to use temperature-dependent viscoelastic bulk modulus since the EMC material in packages is subjected to multiaxial constraints. The effect of the assumption on stress

analyses was discussed in Ref. [60], where the effect of the time-dependent bulk modulus on the internal stresses of Decawatt package (DPAK) in automotive ECU units was investigated using a linear viscoelastic analysis. The results showed that the constant bulk modulus overestimated the wire-lift force significantly due to extra constraints. A similar analysis was conducted to investigate the effect of the constant Poisson's ratio assumed in a linear elastic analysis on the package warpage [61]. The results showed that the constant Poisson's ratio increased the predicted warpage of a package containing two stacked dies by approximately 24%.

2.4. Cure-extent dependent Viscoelastic Behavior

It is important to recall that the modulus evolves non-linearly during molding (Figure 5). As mentioned earlier, a different set of cure-extent dependent material functions are required to predict cure-induced warpage after molding.

2.4.1. Cure-extent dependent shear viscoelasticity

In the classical viscoelasticity theory, the cure-dependent shear relaxation modulus can be expressed as [62]:

$$G(t,p) = G_\infty + G_t(t,p) \tag{19}$$

where $G_\infty(p)$ and $G_t(t,p)$ are the equilibrium modulus (steady-state) and the transient part of the modulus, respectively, at a cure extent of p. The relaxation modulus describes the transient behavior, while the equilibrium modulus defines the behavior after complete relaxation. Both properties are required accurately to predict a stress state at each instance during curing.

It was observed that the shear relaxation mechanism of thermorheologically simple (TRS) polymers remains the same during the curing process. However, increase in length of the polymer

chains during curing reduces the degree of freedom of the chains causing increase of the elastic stiffness (or equilibrium modulus, G_∞) [63]. For the same reason, relaxation time also increases as curing progresses.

Attempts to explain the gel formation and evolution of equilibrium modulus have been made using the Mean Field Theory [64] and the percolation theory [65]. It was also observed that a large set of thermosetting polymers, specifically epoxy resins, followed the percolation theory [16, 66-69]. The equilibrium modulus evolution of a two-component epoxy in the percolation theory was expressed as [70]:

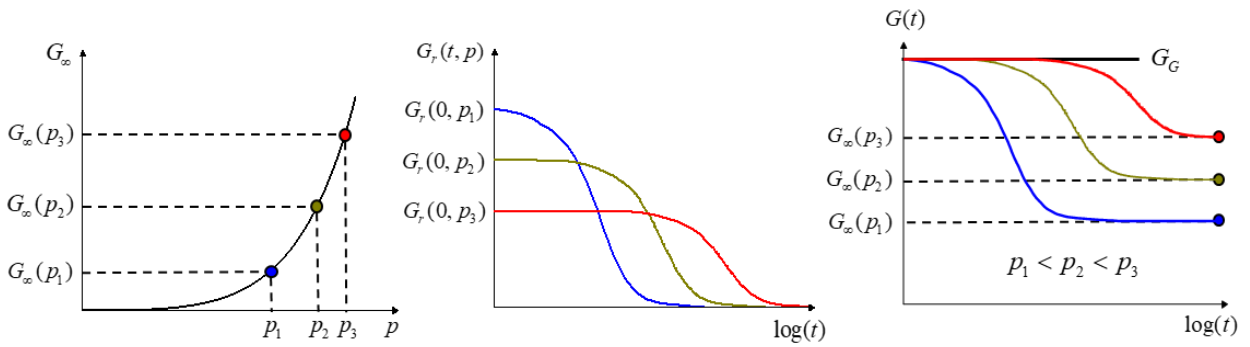
$$G_\infty(p) = G_\infty^f \left(\frac{p^2 - p_{gel}^2}{1 - p_{gel}^2} \right)^d \tag{20}$$

where $G_\infty(p)$ is the equilibrium modulus at a given degree of cure; G_∞^f is the equilibrium modulus of fully cured polymer; p_{gel} is a degree of cure at the gel point; and d is the evolution exponent determined experimentally [70].

The relaxation behavior at a given degree of cure can be represented by Prony series as:

$$G_r(t,p) = \sum_{i=1}^{n} G_i(p) \exp\left(-\frac{t}{\tau_i}\right) \tag{21}$$

where $G_i(p)$ is the Prony shear constants at a given degree of cure and τ_i are relaxation time constants. This is illustrated in Figure 19 (b), where increase in relaxation time at a higher degree of cure is evident. The complete cure-dependent shear modulus, $G(t,p)$, is illustrated in Figure 19 (c), where G_G is the glassy modulus.



(a) (b) (c)

Figure 19 Schematic illustration of cure extent dependent EMC behavior: (a) equilibrium modulus evolution; (b) relaxation modulus as a function of time; and (c) complete time dependent behavior

2.4.2. Time-cure superposition (TCS)

The concept of time-cure superposition (TCS) was first proposed by Adolf and Martin [70, 71] after observing that the relaxation behavior of TRS polymers remained the same during curing. The TCS concept is similar to the well-known TTS concept described in Section 3. Since its introduction, numerous researchers have shown that the viscoelastic behavior at different extents of cure can be superposed using appropriate horizontal shifts.

The initial implementations of the TCS concept were carried out for unfilled thermosets [72, 73], where the cure extent-dependent equilibrium modulus was ignored or handled improperly. Later, the concept was extended to filled thermosets including EMC, which clearly showed the effect of cure extent on the equilibrium modulus. To incorporate the concept for numerical implementation, Yang et.al [74] proposed a procedure to normalize the relaxation behavior by the difference between the glassy modulus and the cure extent-dependent equilibrium modulus, and it was implemented later by several others [14, 69, 75, 76]. The normalization can be expressed as:

$$\frac{G_r(t,p)}{G_G - G_\infty(p)} = \sum_{i=1}^{N} \frac{G_i(p)}{G_G - G_\infty(p)} \exp\left(-\frac{t}{\tau_i}\right) = \sum_{i=1}^{N} g_i \exp\left(-\frac{t}{\tau_i}\right) \tag{22}$$

where g_i are the normalized Prony shear constant, which is independent of cure extent. The normalized relaxation modulus at various degrees of cure is illustrated in Figure 20.

A cure-dependent shift function, $a_P(p)$, was employed to handle the increase in relaxation times during curing [69, 77]. The shift factors are also illustrated in Figure 20. The reduced-time, ϕ_P, is defined as [73]:

$$\psi_p(t) = \int_0^t \frac{d\xi}{a_p(p)} \tag{23}$$

The complete relaxation behavior as a function of cure extent can be expressed as [74]:

$$G(t,p) = G_\infty(p) + [G_G - G_\infty(p)] \sum_{i=1}^{N} g_i \exp\left(-\frac{\psi_p}{\tau_i}\right) \tag{24}$$

More details about the above equation can be found in Ref. [74, 78].

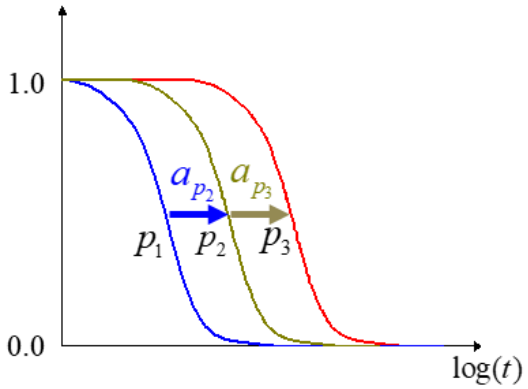


Figure 20 Illustration of the TCS concept, where the relaxation modulus obtained at various cure extents are normalized by the difference between the glassy modulus and the equilibrium modulus

2.4.3. Measurement of cure-extent dependent viscoelastic properties

Determination of cure-extent dependent viscoelastic properties require experimental techniques to measure the properties for various cure extents. The multi-frequency and temperature sweeps (MFT) of DMA was the preferred choice [69, 79, 80] for measuring cure-dependent viscoelastic Young's modulus (*E*).

For measurement of cure-dependent moduli, a partially cured specimen at a known cure-extent is subjected to MFT sweeps to obtain the frequency dependent behavior. These MFT sweeps have to be conducted at temperatures significantly lower than cure temperature (or sometimes T_g of the partially cured polymer) to ensure slow reaction rates during MFT sweeps.

Lin et.al. [13] proposed a combined or dual shift methodology to account for mechanical testing temperature (*T*) and degree of cure (*p*). In the implementation, the frequency-dependent isocure data at various testing temperatures (significantly below T_{cure}) is shifted to the reference temperature (T_{ref}) to create the master-curve of a partially- cured specimen (p_1). This procedure is repeated to produce the master-curves at various cure extents. The master curves obtained at three cure extents are illustrated in Figure 19 (c). These master curves are normalized by equilibrium moduli, as described by Eq. (22). Finally, the normalized master curves are shifted horizontally to obtain the cure-dependent shift factor (a_p). The combined shift factor ($a_{combined}$) consists of the two components – temperature dependency and cure dependency as [13]:

$$\log(a_{combined}) = \log(a_T) + \log(a_p) \tag{25}$$

The current practice of measuring the cure-extent dependent properties is based on well-known theories but also on unconfirmed assumptions. These issues should be addressed to enhance warpage productivity in the future.

In the current practice of creating a master curve of partially cured polymer, the mechanical testing is conducted at temperatures much lower than the curing temperature to ensure that extra curing during testing can be negligible, i.e., to maintain the constant cure-extent state. This would result in much less viscoelastic behavior, and would require a proportionally larger range of frequencies to obtain a complete master curve. With the commercial DMA machines, it would be rather difficult, albeit not impossible, to obtain the equilibrium modulus accurately.

It was observed for some thermosets that the temperature shift factor is independent of the degree of cure and can be used directly to shift the master curves of partially cured specimens to the reference temperature [69, 80]. The viscoelastic behavior of partially cured polymers is affected significantly by the degree of cure. This observation was not supported by any rigorous theoretical explanations and should be practiced with extreme caution.

It is important to recall that fully cured EMC shows strong time dependent bulk behavior [59]. With less crosslinking, partially cured EMC would definitely show even stronger time dependent bulk behavior. It is inevitable that the cure extent dependent viscoelastic bulk modulus must be measured to predict the warpage after compression molding accurately.

Packages fabricated by molding processes are subjected to the post mold curing (PMC) process, which produces additional effective cure shrinkage induced-deformations as well as CTE mismatch-induced thermal deformations. It is clear that both cure-dependent and post-cure viscoelastic properties are required to accurately predict the warpage after compression molding.

2.5. Additional discussion: About compression molding

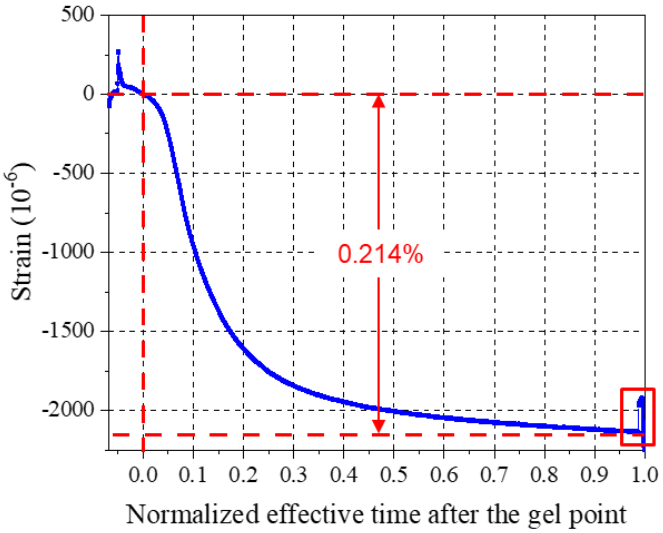
In the compression molding, mold parameters (temperature, pressure, and time) affect the warpage behavior. This implies that the warpage behavior can be tailored for a given EMC to a

certain degree. A test similar to one to measure the effective cure shrinkage (Section 2) was conducted to illustrate the concept.

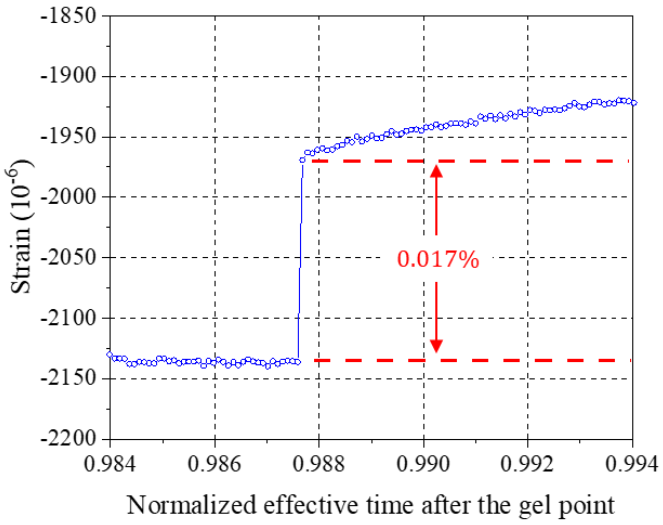
In this test, the pressure was maintained until curing was completed to simulate the compression molding condition. The results are shown in Figure 21. The total EMC strain was 0.214%, which is nearly three times as high as the effective cure shrinkage reported in Section 2 (i.e., the strain without the pressure). It was attributed to the near hydrostatic creep deformation caused by the pressure after the gel point. The pressure was removed after curing was completed. The behavior is shown in Figure 21 (b). A sudden increase of the EMC strain is apparent, which represents the elastic recovery of EMC deformed by the pressure. The EMC creep strain was recovered continuously as a function of time.

The package warpage after demolding is illustrated schematically in Figure 22. The elastic and creep recovery after compression demolding produces downward bending ($\cap$) at the mold temperature (Figure 22(a)). This is opposite to the case of transfer molding, which produces upward bending ($\cup$) at the mold temperature (Figure 22 (b)).

As mentioned earlier, there is a gap in literature associated with experimental data and constitutive models associated with the time and cure dependent behavior of *K*. This behavior must be characterized experimentally to be incorporated into numerical modeling for accurate warpage prediction after compression molding.

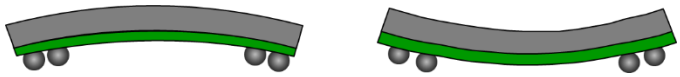


(a)



(b)

Figure 21. Strain evolution from a test simulating compression molding, where the pressure is 7 MPa: (a) complete strain evolution and (b) zoom-in view marked by a box in (a).



(a) (b)

Figure 22. Schematic illustration of warpage behavior after demolding at the mold temperature: (a) compression molding and (b) transfer molding

2.6. Concluding Remarks

This review paper discussed three topics related to warpage prediction uncertainties.

(1) The first topic was related to the cure shrinkage that occurs during molding. The modulus of EMC associated with the cure shrinkage developed before the gel point is virtually "zero", and it does not contribute to cure-induced warpage. The cure shrinkage that occurs after the gel point is called the effective cure shrinkage (ECS). The ECS value should be used for calculation of cure-induced warpage.

(2) The second topic was the two-assumption used, but not yet validated, in the current practice of linear viscoelastic analysis, "*constant* Poisson's ratio and "time *independent* bulk modulus". Experimental data were presented to show that the assumptions are not valid at high temperatures, especially around the glass transition temperature. Time and temperature-dependent bulk modulus should be used for a viscoelastic analysis for accurate warpage prediction.

(3) The last topic dealt with the cure-extent dependent viscoelastic behavior. Only limited data is available in the literature due to the measurement complexity (theoretical as well as experimental). More measurements of partially cured EMC properties are warranted to improve warpage predictability.

Utilizing the uniaxial as well as bulk behavior of partially and fully cured EMC, "designing" warpage – in contrast to the conventional approach to "controlling" warpage – would become

possible to enable the industry to tailor advanced molding process parameters, including but not limited to (1) mold temperature, pressure, and time and (2) post-mold curing temperature and time.

Chapter 3 Deterministic Approach to Obtain Autocatalytic Cure Kinetics Model Constants by Normal Equations of Least-Squares Method

3.1. Introduction

The thermoset cure process is exothermic, and the amount of heat released can be directly measured by differential scanning calorimetry (DSC). The measured quantity provides the degree of cure, which can be used to investigate cure kinetics.

There are several methodologies and techniques available in the literature to determine the cure kinetics model constants. After the pioneering and original work by Borchardt and Daniels (B/D) [81], the American Society for Testing and Materials (ASTM) established a standard test method based on *linear* regression, through which the kinetic parameters of the well-known n^{th} order model are determined from a single temperature scanning DSC data at a linear heating rate (also known as dynamic heating scan measurement data) [82]. The method is quick and useful, and it has been practiced widely.

Numerous advanced thermosets, typically highly-filled with silicas (50 to 90 wt.%), are used in the semiconductor packaging industry. Understanding the curing behavior of the filled thermosets are increasingly important to optimize manufacturing processes, as the packages are becoming thinner and complex [83, 84] .

The advanced thermosets typically follow the autocatalytic behavior, for which the autocatalytic kinetics model should be used to describe the curing behavior faithfully, especially at the beginning of cure. Several types of *non-linear* regression algorithms have been implemented to determine the kinetic parameters of the autocatalytic model [85]. Due to the extreme non-linear nature of the model, the non-linear regression usually requires a large quantity of dynamic scan

data obtained at three or more heating rates to ensure proper convergence during the regression, unless the initial values of the constants are selected carefully.

This paper proposes a novel method to determine the constants of the autocatalytic model using DSC data. The proposed method is based on the *normal* equations, which is an analytical approach of the least-squares method. The method requires only two standard DSC dynamic scan data obtained at the linear heating rates of 5 and 10 °C/min, but can obtain the four cure kinetics parameters of the autocatalytic model, including the activation energy, analytically but accurately without regression analyses. The method is described in detail after briefly reviewing the autocatalytic cure kinetics model. The method is implemented for a highly-filled epoxy molding compound (EMC). The experimental data and the predictions of cure extent are presented, and the robustness and accuracy of the method are discussed.

3.2. Cure kinetics Model

The general form of reaction kinetics model is expressed as [11]:

$$\frac{dp}{dt} = k(T,p) \cdot f(p) \tag{26}$$

where k is the rate constant; and $f(p)$ is the cure kinetics function that can take any mathematical form of p. The rate constant can be a function of both temperature (T) and cure-extent (p). For most thermosets used in the semiconductor packaging industry, it has been known that the rate constant is independent (or a very weak function) of cure-extent [86-88], and it can be expressed using the Arrhenius equation as:

$$k(T) = A \exp\left(-\frac{E_a}{RT}\right) \tag{27}$$

where A is the Arrhenius constant; E_a is the activation energy; and R is the ideal gas constant ($8.314\ J \cdot mol^{-1} \cdot K^{-1}$).

Then, the modified autocatalytic model, known as Kamal-Sourour (KS) model, takes the following form [89]:

$$\frac{dp}{dt} = k(T) \cdot p^m (1-p)^n;\ k(T) = A \exp\left(-\frac{E_a}{RT}\right) \tag{28}$$

where *n* and *m* are reaction orders associated with the model.

3.3. Proposed Deterministic Approach

The proposed method is based on the normal equation, which is an analytical approach of the least-squares method [90]. The normal equation-based least-squares method was utilized successfully to determine the elastic constants using the experimental full-field displacement field [91]. A similar approach is adopted to determine the KS model constants.

The KS model can be expressed in the following form by taking natural logarithm of Eq. (28) as:

$$\ln\left(\frac{dp}{dt}\right) = \ln A + n\ln(1-p) + m\ln(p) - \frac{E_a}{RT} \tag{29}$$

The objective function (S) defined by sum of square error (SSE) between the model prediction and the DSC data can be expressed as:

$$\begin{aligned} S &= \sum_{i=1}^{N}\left[\ln\left(\frac{dp}{dt}\right)_{i,model} - \ln\left(\frac{dp}{dt}\right)_{i,DSC}\right]^2 \\ &= \sum_{i=1}^{N}\left[\ln A - \frac{E_a}{RT} + n\ln(1-p) + m\ln(p) - \ln\left(\frac{dp}{dt}\right)_{i,DSC}\right]^2 \end{aligned} \tag{30}$$

The least-squares criterion for the four independent variables (i.e., the first-order condition of the least-squares minimization) requires:

$$\frac{\partial S}{\partial(\ln A)} = \frac{\partial S}{\partial E_a} = \frac{\partial S}{\partial m} = \frac{\partial S}{\partial n} = 0 \tag{31}$$

The above criterion produces a system of equations, known as the *normal* equations. The results can be expressed in a matrix form as:

$$\{X\} = [C]^{-1}\{B\} \tag{32}$$

where $\{X\} = \begin{Bmatrix} \ln A \\ E_a \\ n \\ m \end{Bmatrix}$

$[C]$

$$= \begin{bmatrix} \sum_{i=1}^{N} 1 & -\sum_{i=1}^{N} \frac{1000}{RT_i} & \sum_{i=1}^{N} \ln(1-p_i) & \sum_{i=0}^{N} \ln(p_i) \\ -\sum_{i=1}^{N} \frac{1000}{RT_i} & \sum_{i=1}^{N} \frac{1000^2}{R^2T_i^2} & -\sum_{i=1}^{N} \frac{1000}{RT_i}\ln(1-p_i) & -\sum_{i=1}^{N} \frac{1000}{RT_i}\ln(p_i) \\ \sum_{i=1}^{N} \ln(1-p_i) & -\sum_{i=1}^{N} \frac{1000\ln(1-p_i)}{RT_i} & \sum_{i=1}^{N} (\ln(1-p_i))^2 & \sum_{i=1}^{N} \ln(1-p_i)\ln(p_i) \\ \sum_{i=1}^{N} \ln(p_i) & -\sum_{i=1}^{N} \frac{1000}{RT_i}\ln(p_i) & \sum_{i=1}^{N} \ln(p_i)\ln(1-p_i) & \sum_{i=1}^{N} (\ln(p_i))^2 \end{bmatrix}$$

$$\{B\} = \begin{Bmatrix} \sum_{i=1}^{N} \ln\left(\frac{dp}{dt}\right)_i \\ -\sum_{i=1}^{N} \frac{1000}{RT_i}\ln\left(\frac{dp}{dt}\right)_i \\ \sum_{i=1}^{N} \ln(1-p_i)\ln\left(\frac{dp}{dt}\right)_i \\ \sum_{i=1}^{N} \ln(p_i)\ln\left(\frac{dp}{dt}\right)_i \end{Bmatrix}$$

The values of dp/dt and p are directly obtained from DSC tests. In the above equations, "*N*" is the number of data points obtained from the DSC measurements. If there are no differences between the model predictions and the DSC data, the four constants in the above equation (A, E_a, n and m) can be determined using only four arbitrary points in the DSC data. In practice, discrepancies attributed to experimental uncertainties are always present, and this is the rationale of the over deterministic approach where the *N* is much larger than the number of constants to be determined [10]. It is also important to recall that the normal equation is a closed-form solution that minimize the value of SSE. The solution is always unique (global minima) as long as $[C]^{-1}$ is determinable [90-92].

Data Required to Handle Non-linearity of KS Model

The KS model poses a new regression analysis challenge due to its extreme non-linearity, more specifically, dual power terms of cure-extent). As explained clearly in the ASTM standard [3], the simpler n^{th} order model in a logarithm form can be expressed as a linear function with two independent variables (x, y), repeated here, as

$$z(x, y) = a + bx + cy \tag{33}$$

where $z \equiv \ln(dp/dt)$; $a \equiv \ln A$; $b \equiv n$; $x \equiv \ln(1-p)$; $c \equiv E_a/R$; and $y \equiv 1/T$. It is worth noting that the first independent variable, *x*, is a function of cure extent, *p*; and the second independent variable, *y*, is a function of temperature, *T*.

Eq. (33) defines a plane for a given set of three parameters (A, n, E_a) in the (x, y) domain. This is graphically illustrated in Figure 23. A line produced by a single dynamic scan data is also shown in Figure 23. It is important to note that the line lies in the plane, but it is curved due to the

non-linear relationship between the x and y variables. Therefore, the solution obtained from the normal equations using a single dynamic scan data can define the plane uniquely; and thus, the three parameters (A, E_a, n) can be obtained by the normal equations using a single dynamic scan data.

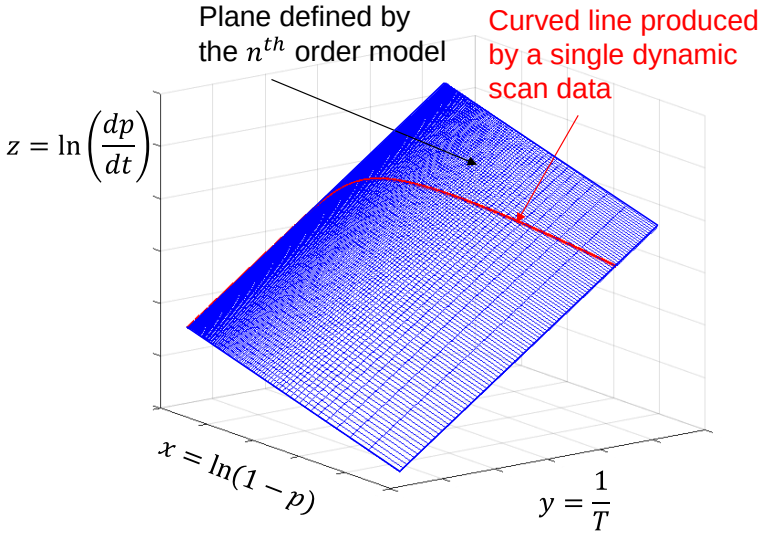


Figure 23 A plane defined by the n^{th} order model (Eq. 8); and a line produced by a single dynamic scan data

The KS model of Eq. (29) can be expressed using the similar notations as:

$$z(x, y) = a + b_1 x_1 + b_2 x_2 + cy \tag{34}$$

where $z \equiv \ln(dp/dt)$; $a \equiv \ln A$; $b_1 \equiv n$; $x_1 \equiv \ln(1-p)$; $b_2 \equiv m$; $x_2 \equiv \ln p$; $c \equiv E_a/R$; and $y \equiv 1/T$. The above equation contains two variables, (x_1, x_2), that are a function of p. They are related as $x_2 = \ln(1 - e^{x_1})$. Thus, Eq. 9 can be rewritten as:

$$z(x, y) = a + b_1 x + b_2 \ln(1 - e^{x}) + cy \tag{35}$$

Eq.(35) defines a curved surface for a given set of four parameters (A, n, m, E_a) in the (x, y) domain, which cannot be defined by a single curved line obtained from a single dynamic scan data; in other words, a curved plane cannot be defined uniquely by a single curved line. This

implies that the closed form solution obtained from Eq. 7 using a single dynamic scan data will not provide a unique set of the four parameters of the KS model. One more dynamic scan data (i.e., an additional curved line) is required to define the curved surface uniquely.

This can be expressed mathematically as:

$$[C]_1\{X\} + [C]_2\{X\} = \{B\}_1 + \{B\}_2$$
$$[C] = [C]_1 + [C]_2 \text{ and } \{B\} = \{B\}_1 + \{B\}_2 \quad (36)$$

where $[C]_i$ and $\{B\}_i$ for $i = 1, 2$ are the matrices obtained from two dynamic scan data.

3.4. Implementation

An epoxy molding compound (EMC) was used to determine the cure kinetics constants of the KS model. TA Discovery DSC 250 was used to obtain the dynamic scan data at the standard heating rates of β = 5 and 10 °C/min. The heat flow data ($\dot{Q}$) obtained from DSC are shown as a function of temperature ($°C$) in Figure 24, where the heat flow is scaled by the higher heating rate ($\beta_{ref} = 10$ °C/min).

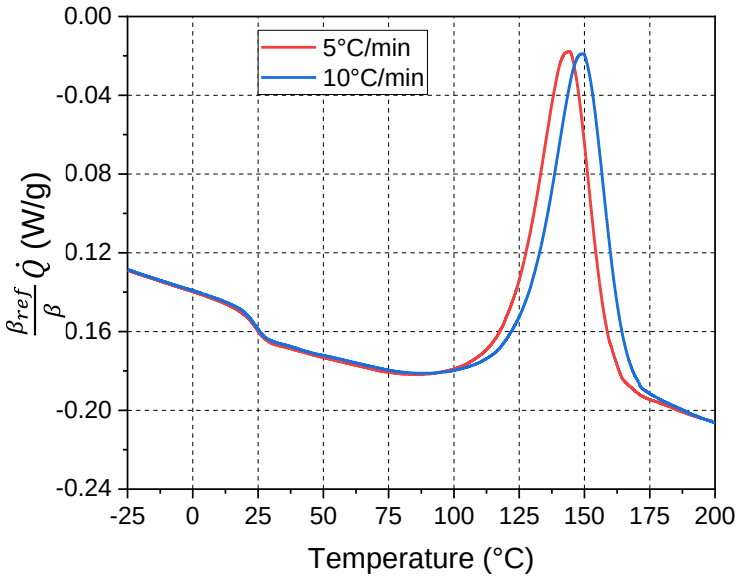


Figure 24 DSC dynamic scan data at the standard heating rates of β = 5 and 10 °C/min; the data is scaled by the higher heating rate (β_{ref} = 10 °C/min).

The total enthalpy of the reaction (ΔH) was measured by subtracting the baseline determined using the start and the end point. The average enthalpy of the reaction obtained from both rates was 29.2 ± 0.16 J/g. The curing rate (dp/dt) as a function of temperature were obtained by dividing the heat flow rate ($\dot{Q}$) by the total amount of heat released. The results are shown in Figure 25.

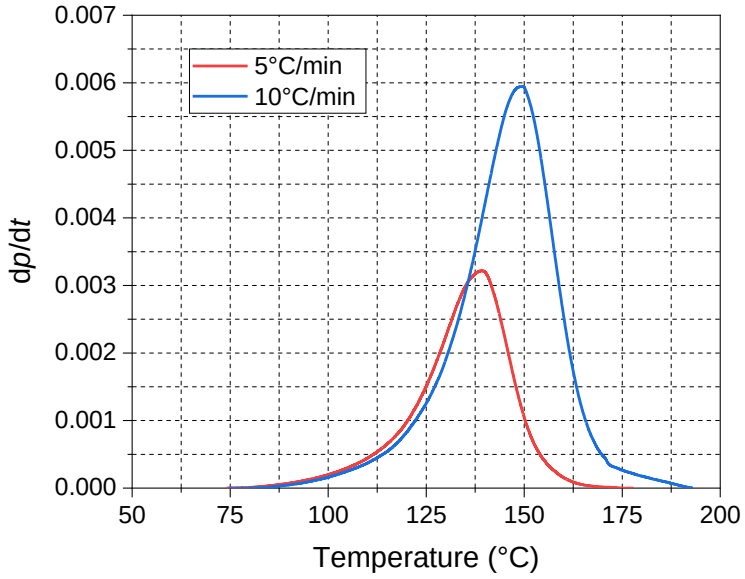


Figure 25 Rate of reactions (dp/dt) as a function of temperature (T), obtained from the data shown in Figure 24

The normal equation matrices (Eq. (36)) obtain from each data sets are:

$$\{X\} = \left([C]_{5°C/min} + [C]_{10°C/min} \right)^{-1} (\{B\}_{5°C/min} + \{B\}_{10°C/min})$$

$$\{B\}_{5°C/min} = \begin{Bmatrix} -32974.20 \\ 9852.37 \\ 25544.08 \\ 41872.23 \end{Bmatrix}; \{B\}_{10°C/min} = \begin{Bmatrix} -17585.1 \\ 5082.67 \\ 18423.61 \\ 19895.75 \end{Bmatrix} \quad (37)$$

$$[C]_{5°C/min} = \begin{bmatrix} 5070 & -1511.89 & -4042.54 & -6109.68 \\ -1511.89 & 451.26 & 1171.41 & 1862.67 \\ -4042.54 & 1171.41 & 6764.42 & 1703.918 \\ -6109.67 & 1862.67 & 1703.918 & 11430.12 \end{bmatrix}$$

$$[C]_{10°C/min} = \begin{bmatrix} 2947 & -851.01 & -3026.52 & -3208.63 \\ -851.01 & 246.03 & 846.20 & 953.01 \\ -3026.52 & 846.20 & 6360.26 & 936.5 \\ -3208.63 & 953.01 & 936.5 & 6026.78 \end{bmatrix}$$

This yields:

$$\{X\} = \begin{Bmatrix} \ln A \\ E_a \\ n \\ m \end{Bmatrix} = \begin{Bmatrix} 17.556 \\ 75.44 \\ 1.13 \\ 0.62 \end{Bmatrix} \tag{38}$$

The four parameters of the KS model obtained from $\{X\}$ are shown in Table 1.

Table 1 Reaction constants of KS model

$\boldsymbol{A}$ $(\boldsymbol{s^{-1}})$	$\boldsymbol{E_a}$ $(\mathbf{kJ \cdot mol^{-1}})$	$\boldsymbol{n}$	$\boldsymbol{m}$
4.21E+07	75.44	1.13	0.62

The values in Table 1 were used to predict the cure extent. The predicted cure extent is compared with the cure extent obtained from DSC data in Figure 26. Two additional dynamic scan data obtained at the heating rates of β = 2.5 and 7.5 °C/min are also used for comparison. The predicted values and the experimental data show excellent agreements, not only at the two standard rates used to determine the parameters, but also at the two additional rates.

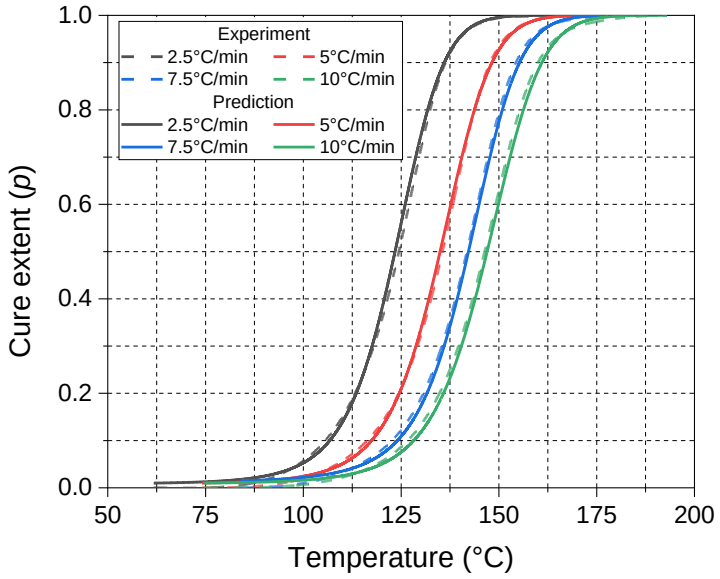


Figure 26 Precited cure extent is compared with experimental data. Only the data obtained from the standard rates of β = 5 and 10 °C/min are used to determine the model parameters, and the additional dynamic scan data (β = 2.5 and 7.5 °C/min) are used only for comparison.

3.5. Discussions

As discussed earlier, the normal equation using a single dynamic scan data will not provide a unique set of the four parameters of the KS model. In order to examine this further, the four parameters were determined using the single data set of 5°C/min using Eq.(32). The results are:

$$\{X\}_{\beta=5\ °C/\min} = \begin{Bmatrix} \ln A \\ E_a \\ n \\ m \end{Bmatrix} = \begin{Bmatrix} -73.11 \\ -237.01 \\ 0.33 \\ 3.15 \end{Bmatrix} \tag{14}$$

The values are significantly different from the values obtained from two dynamic scan data (Eq.(38)).

This discrepancy is explained graphically in Figure 27. The black plane shows the curved surface representing the true solution (Eq. (38)), while the blue plane shows the curved surface

representing the solution obtained only using the single dynamic scan data of 5°C/min (Eq. (14)). The intersecting line (red line) is identical to a curved line produced by the 5°C/min dynamic scan data. The results clearly show that one additional curved line is required to define the black plane uniquely.

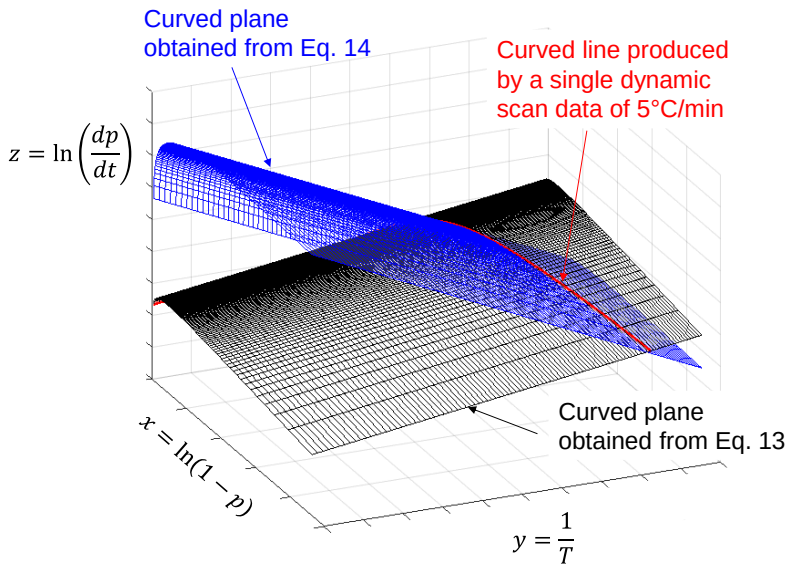


Figure 27 Curved surfaces represented by Eq. (35), where black and blue planes are obtained from Eq. (38) and (14), respectively. The intersecting line (red) coincides with a curved line produced by the single dynamic scan data of 5 °C/min

3.6. Conclusions

An analytical approach based on the *normal* equations of the least-squares method was developed to determine the constants of the autocatalytic model, and it was implemented for a highly-filled epoxy molding compound (EMC). Only two standard DSC dynamic scan data (β = 5 and 10 °C/min) were required to uniquely obtain the four cure kinetics parameters of the autocatalytic model, including the activation energy. The predicted cure extent was compared with the cure extent obtained from DSC data. The predicted values and the experimental data showed excellent agreements, not only at the two standard rates used to determine the parameters,

but also at the two additional dynamic scan data obtained at the heating rates of β = 2.5 and 7.5 °C/min, which corroborated the robustness and the accuracy of the proposed method.

The method is “analytical” in nature, and can be implemented by commercial spreadsheet application software. The method is efficient, but robust and accurate. More implementations using advanced thermosets in semiconductor packaging are expected.

Chapter 4 Novel Method to Determine Autocatalytic Cure Kinetics Model Constants of Dual Reaction Thermosets Using Minimum Testing Data

4.1. Introduction

A wide range of advanced thermosets, typically highly filled with silica ranging from 50 % to 90 % (w/w), are being extensively used and continuously developed for advanced semiconductor packaging applications. Understanding the curing behavior of those filled thermosets and cure-dependent material properties is increasingly important for optimizing manufacturing processes, as the advanced packages become thinner and more complex to accommodate the ever-increasing demand for portability and integration [83, 84].

Differential scanning calorimetry (DSC) provides a convenient and robust way to measure the extent of cure, or degree of cure (DOC), for thermosetting polymers [93]. Several methodologies to determine the cure kinetics model constants for single-reaction polymer systems using DSC data are readily available in the literature [94-96], as well as ASTM standards including ASTM E698 (Flynn/Wall/Ozawa method), E2041 (Borchardt and Daniels method), E2890 (Kissinger's and Farja's methods), and E2070 (isothermal methods).

Dual reactions are often present in advanced thermosets [86, 93, 94, 97, 98] to achieve the desired specifications to satisfy various design and manufacturing requirements. The details of the reaction systems (i.e., chemistry and composition) are typically proprietary information and not disclosed by material manufacturers. Additionally, the high inorganic filler loading produces

a proportionally smaller amount of heat during curing. These factors make quantitative characterization of the cure kinetics of dual reactions challenging.

Analysis of the cure kinetics of dual-reaction thermosets requires the determination of nine model constants: the ratio of the first reaction to the total reaction; and eight constants of two autocatalytic models that describe dual-reactions. Simultaneous determination of the nine constants from experimental data using regression analyses is challenging because of the extremely non-linear nature of combined kinetic functions. A set of initial values that are reasonably close to the true model constants are required for proper convergence.

This paper proposes a novel method to obtain the required initial values consistently, which subsequently enables the accurate determination of all nine constants. The method utilizes a well-known model-free analysis and an analytical least-squares approach. The proposed method is remarkably efficient; it requires only two sets of DSC dynamic scan data (at linear heating rates of 5 °C/min and 10 °C/min) to determine the contributions of the first and second reactions to the total cure reaction as well as the eight model constants in two autocatalytic models representing these two reactions.

The proposed method is described in detail after briefly reviewing the cure kinetics models and kinetic analyses. The method is implemented here using a highly-filled dual-reaction epoxy-based underfill material used in advanced semiconductor packaging applications. The results are reported while corroborating the validity and accuracy of the proposed method.

4.2. Cure Kinetics Model and Kinetic Analysis

A general form of reaction kinetics model and an autocatalytic model, known as the Kamal-Sourour model are first reviewed here. One of the model-free (isoconversional) kinetic analysis

methods, known as the Friedman method, is also reviewed. A deterministic approach to determine the model constants of the Kamal-Sourour model is described briefly.

4.2.1. General reaction kinetics model

The general form of reaction kinetics model is expressed as [11, 99, 100]:

$$\frac{dp}{dt} = k(T,p) \cdot f(p) \tag{39}$$

where *t* is the time (in seconds); k is the rate constant (in s^{-1}); and $f(p)$ is the reaction model. The rate constant can be a function of both temperature (T) and extent of cure (p). For most thermosets used in the semiconductor packaging industry, it has been reported that the rate constant is independent (or a very weak function) of the extent of cure [87, 88]. The rate constant can be expressed using the Arrhenius equation as:

$$k(T) = A \exp\left(-\frac{E_a}{RT}\right) \tag{40}$$

where A is the pre-exponential factor (in s^{-1}); E_a is the activation energy (in J mol^{-1}); and R is the ideal gas constant (8.314 J mol^{-1} K^{-1}).

Then, the modified autocatalytic model, known as the Kamal-Sourour model, takes the following form [89]:

$$\frac{dp}{dt} = k(T) \cdot p^m (1-p)^n \tag{41}$$

where n and m are reaction orders associated with the model.

4.2.2. Isoconversional analysis: Friedman method

The isoconversional (also known as model-free) analysis [101] offers a way of determining the activation energy of a reaction process without assuming a cure kinetics function. The main advantage of the model-free analysis is its simplicity while avoiding errors associated with choice of a kinetic model. Two most widely-known methods are the Friedman method (a differential model-free method) [102] and the Kissinger–Akahira–Sunose method (an integral model-free method) [103]. The former is adopted in this study because the curing rate (dp/dt) from a dynamic scan data of DSC can be directly used for the analysis. The method is briefly reviewed below.

Taking the logarithm of the general kinetics model (Eqs. (26) and (2)) yields

$$\ln\left(\frac{dp}{dt}\right) = \ln\big(A \cdot f(p)\big) - \frac{E_a(p)}{RT} \tag{42}$$

At a constant cure extent (p), the above equation becomes a linear curve, which can be expressed as:

$$y = a + bx \tag{43}$$

where $y \equiv \ln(dp/dt)$; $b \equiv \ln\big(A\, f(p)\big)$; $a = E_a(p)/R$ and $x = 1/T$. The slope of the linear equation provides the activation energy at a given cure extent, $E_a(p)$ [102, 104]. The activation energy can be calculated from the slope of the line using the following equation:

$$E_a(p) = -R \left(\frac{\ln\left(\frac{dp}{dt}\right)}{\frac{1}{T}} \right)_p \tag{44}$$

4.3. Deterministic Approach to Obtain Kamal-Sourour Model Constants [105]

The Kamal-Sourour (K-S) model can be expressed in the following form by taking the natural logarithm of Eq. (28) as:

$$\ln\left(\frac{dp}{dt}\right) = \ln A + n\ln(1-p) + m\ln(p) - \frac{E_a}{RT} \tag{45}$$

The objective function (S) defined by the sum of square error (SSE) between the experimentally measured and calculated reaction rate data can be expressed as:

$$\begin{aligned} S &= \sum_{i=1}^{N}\left[\ln\left(\frac{dp}{dt}\right)_{\text{i,model}} - \ln\left(\frac{dp}{dt}\right)_{\text{i,DSC}}\right]^2 \\ &= \sum_{i=1}^{N}\left[\ln A - \frac{E_a}{RT} + n\ln(1-p) + m\ln(p) - \ln\left(\frac{dp}{dt}\right)_{\text{i,DSC}}\right]^2 \end{aligned} \tag{46}$$

The least-squares criteria for the four independent variables requires:

$$\frac{\partial S}{\partial(\ln A)} = \frac{\partial S}{\partial E_a} = \frac{\partial S}{\partial m} = \frac{\partial S}{\partial n} = 0 \tag{47}$$

The above criterion produces a system of equations, known as the *normal* equations. The results can be expressed in a matrix form as:

$$\{X\} = [C]^{-1}\{B\} \tag{48}$$

where $\{X\} = \begin{Bmatrix} \ln A \\ E_a \\ n \\ m \end{Bmatrix}$;

$$\{B\} = \sum_{i=1}^{N}\begin{Bmatrix} \ln\left(\frac{dp}{dt}\right)_i \\ -\frac{1000}{RT_i}\ln\left(\frac{dp}{dt}\right)_i \\ \ln(1-p_i)\ln\left(\frac{dp}{dt}\right)_i \\ \ln(p_i)\ln\left(\frac{dp}{dt}\right)_i \end{Bmatrix};$$

$$[C] = \sum_{i=1}^{N} \begin{bmatrix} 1 & -\frac{1000}{RT_i} & \ln(1-p_i) & \ln(p_i) \\ -\frac{1000}{RT_i} & \frac{1000^2}{R^2T_i^2} & -\frac{1000}{RT_i}\ln(1-p_i) & -\frac{1000}{RT_i}\ln(p_i) \\ \ln(1-p_i) & -\frac{1000\ln(1-p_i)}{RT_i} & (\ln(1-p_i))^2 & \ln(1-p_i)\ln(p_i) \\ \ln(p_i) & -\frac{1000}{RT_i}\ln(p_i) & \ln(1-p_i)\ln(p_i) & (\ln(p_i))^2 \end{bmatrix}$$

The *normal* equation is an analytical approach of the least-squares method, which does not need to use regression analyses. It has been shown that the method requires only two standard DSC dynamic scan data to obtain the kinetic parameters of the Kamal-Sourour model accurately without regression analyses. More details can be found in Ref. [105].

4.4. Proposed Method

To determine the overall cure reaction kinetics of a dual-reaction system, it is necessary to understand the contribution of each reaction to the overall exothermic heat (ΔH_T) obtained from the dynamic DSC data. The total heat of reaction can be expressed as:

$$\Delta H_T = \Delta H_1 + \Delta H_2 \tag{49}$$

where ΔH_1 and ΔH_2 represent the heat generated by the two reactions, respectively. The overall reaction rate can be expressed as:

$$\frac{dp}{dt} = \eta \frac{dp_1}{dt} + (1-\eta)\frac{dp_2}{dt}$$

$$\Delta H_1 = \eta \cdot \Delta H_T \; ; \;\; \Delta H_2 = (1-\eta) \cdot \Delta H_T$$

$$p_1 = \frac{\Delta H_1}{\Delta H_T}; p_2 = \frac{\Delta H_2}{\Delta H_T} \tag{50}$$

$$p = \eta p_1 + (1-\eta)p_2$$

where η is the ratio of the first reaction to the total reaction (will be referred to as "ratio"). The variable, η, was first introduced in Ref. [106]. Although the value of η should be a constant as a material system parameter, the concept was treated incorrectly, resulting in the values of η that varied with the DSC linear heating rates.

Using the K-S model, the overall reaction model for two reactions can be expressed as:

$$\frac{dp}{dt} = \eta \frac{dp_1}{dt} + (1-\eta)\frac{dp_2}{dt}$$
$$= \eta[k_1(1-p_1)^{n_1}p_1^{m_1}] + (1-\eta)[k_2(1-p_2)^{n_2}p_2^{m_2}] \quad (51)$$

where $k_1 = A_1 \exp\left(-\frac{E_{a1}}{RT}\right)$; $k_2 = A_2 \exp\left(-\frac{E_{a2}}{RT}\right)$, respectively.

The least-squares based method can be utilized to determine the constants. The objective function to obtain the nine constants $[A_1, E_{a1}, n_1, m_1, \eta, A_2, E_{a2}, n_2, m_2]$ is defined as:

$$S_d = \sum_{i=1}^{N}\left[\left(\frac{dp}{dt}\right)_{i,model} - \left(\frac{dp}{dt}\right)_{i,data}\right]^2$$
$$\left(\frac{dp}{dt}\right)_{i,model} = \eta\left(\frac{dp_1}{dt}\right)_{i,model} + (1-\eta)\left(\frac{dp_2}{dt}\right)_{i,model} \quad (52)$$

As mentioned earlier, the optimum values are sensitive to the initial values of the constants since the function shown in Eq. (14) is complex and extremely non-linear. Several local minima can exist which satisfy the convergence requirements. A set of good initial "guesses" or estimated values are required to ensure that the objective function converges at the true values with the minimum amount of test data. A novel procedure is developed to determine the initial values consistently.

Procedure to Determine the Initial Values

The initial values are determined by the following four sequential steps.

Step I: Conduct the model-free analysis

The analysis based on Eq. (44) offers the activation energy as a function of cure-extent. Recalling the fact that the activation energy of the K-S model is only a function of temperature, two reactions would produce two activation energies with a transition region. A middle point over the transition region will be selected as an estimated ratio (η_e).

Step II: Perform the deterministic approach for the first reaction

The closed form solution of Eq. (32) is implemented to estimate the kinetic constants of the first reaction $[(A_1)_e, (E_{a1})_e, (n_1)_e, (m_1)_e]$ using data from two standard DSC dynamic scans. The data obtained from DSC has to be modified using the estimated ratio (η_e) obtained in Step I.

$$\left(\frac{dp_1}{dt}\right)_e = \frac{1}{\eta_e}\frac{dp}{dt}$$
$$(p_1)_e = \frac{1}{\eta_e}p \tag{53}$$

where $\left(\frac{dp_1}{dt}\right)_e$ and $(p_1)_e$ are the estimated curing rate and cure extent of the first reaction, respectively.

Step III: Estimate the heat of the first and second reactions, $\Delta\widehat{H_1}$ and $\Delta\widehat{H_2}$

The first reaction is estimated by the K-S model using the constants obtained in Step II. The second reaction is then estimated by

$$\Delta\widehat{H_2} = \Delta H_T - \Delta\widehat{H_1}$$

where $\Delta\widehat{H_1}$ and $\Delta\widehat{H_2}$ are the estimated heats of the first and second reactions, respectively.

Step IV: Perform the deterministic approach for the second reaction

The closed form solution of Eq. (32) is implemented again to estimate the cure kinetics constants of the second reaction $[(A_2)_e, (E_{a2})_e, (n_2)_e, (m_2)_e]$ using the same two DSC dynamic scan datasets. The data obtained from DSC has to be modified using the estimated ratio (η_e) in Step I.

$$\left(\frac{dp_2}{dt}\right)_e = \frac{1}{1-\eta_e}\left(\frac{dp}{dt} - \eta_e\left(\frac{dp_1}{dt}\right)_e\right)$$
$$(p_2)_e = \frac{1}{1-\eta_e}(p - \eta_e(p_1)_e) \quad (54)$$

where $\left(\frac{dp_2}{dt}\right)_e$ and $(p_2)_e$ are the estimated curing rate and cure extent of the second reaction, respectively.

Non-linear regression to determine the nine constants

Once the initial values of the nine constants [η_e, $(A_1)_e, (E_{a1})_e, (n_1)_e, (m_1)_e$, $(A_2)_e, (E_{a2})_e, (n_2)_e, (m_2)_e$] are estimated, a non-linear fitting method (e.g., a modified form of gradient descent method) is used to determine the final values of the nine constants in Eq. (51).

4.5. Implementation

An epoxy-based underfill (filler contents 65% wt./wt.) was used to implement the proposed method. Use of the underfill material in flip-chip technology is illustrated schematically in Figure 28. The application of underfill involves dispensing the material around the edges of the chip. The underfill flows by capillary action between the chip and the substrate through and around the solder joints. The underfill is cured at high temperatures to achieve the desired thermo-mechanical properties. The function of underfill is two-fold: (1) it redistributes thermal stresses in the layer (the gap between the chip and substrate with solder joints and pads) and, thus, reduces bump stresses significantly and (2) it protects the layer of the device from operating environments [107].

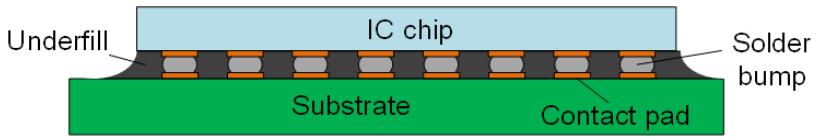


Figure 28 Schematic diagram of a flip-chip IC package

A commercial differential scanning calorimeter (TA Instruments Discovery DSC 250) was used to obtain the dynamic scan data at the standard heating rates of β = 5 °C/min and 10 °C/min. The standard uncertainties for temperature and heat flow are estimated to be ± 1 % and ± 3 %, respectively. The DSC heat flow data ($\dot{Q}$) are shown in Figure 29, where the heat flow is scaled by the higher heating rate ($\beta_{\mathrm{ref}} = 10$ °C/min) for a better comparison of the results at the same instrument sensitivity [86]. The shoulders that occur after the initial peak in Figure 2 clearly indicate two competing reactions.

The total heat of the reaction (ΔH_{T}) was measured by subtracting the baseline determined from the start and the end reaction point. The total heat of the reaction obtained from both rates was consistent with an average value of about 114.8 J/g. The curing rate (dp/dt) as a function of temperature were calculated by dividing the heat flow rate ($\dot{Q}$) by the total heat of reaction. The results are shown in Figure 30.

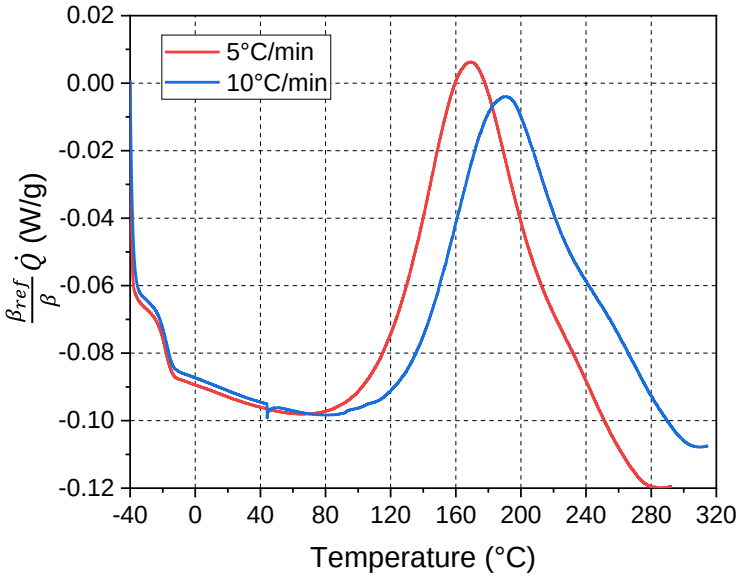


Figure 29 DSC dynamic scan data at the standard heating rates of β = 5 °C/min and 10 °C/min; the data is scaled by the higher heating rate (β_{ref} = 10 °C/min).

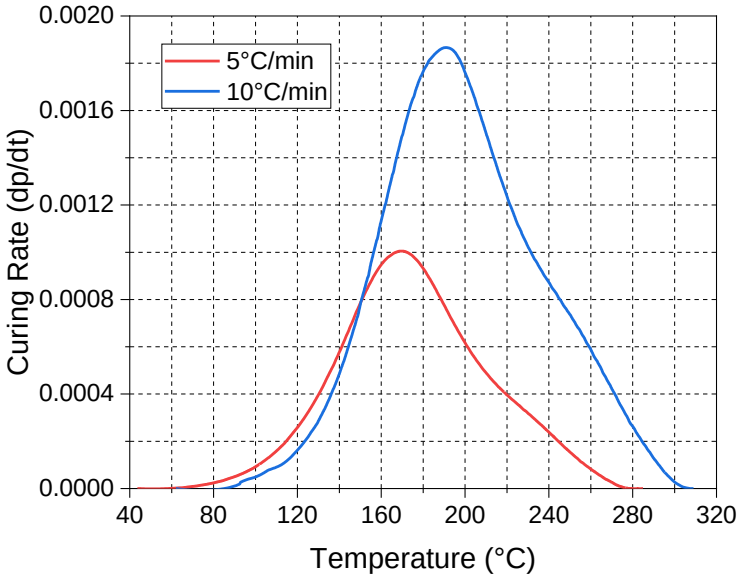


Figure 30 Rate of reactions (dp/dt) as a function of temperature (T), obtained from the data shown in Figure 29

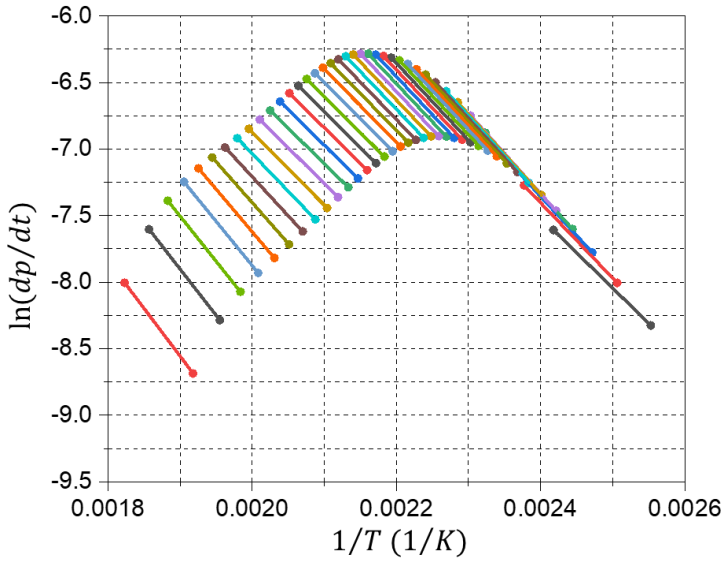


Figure 31 Friedman analysis plot containing lines through isoconversion points obtained from the two standard DSC dynamic scan data (β = 5 °C/min and 10 °C/min)

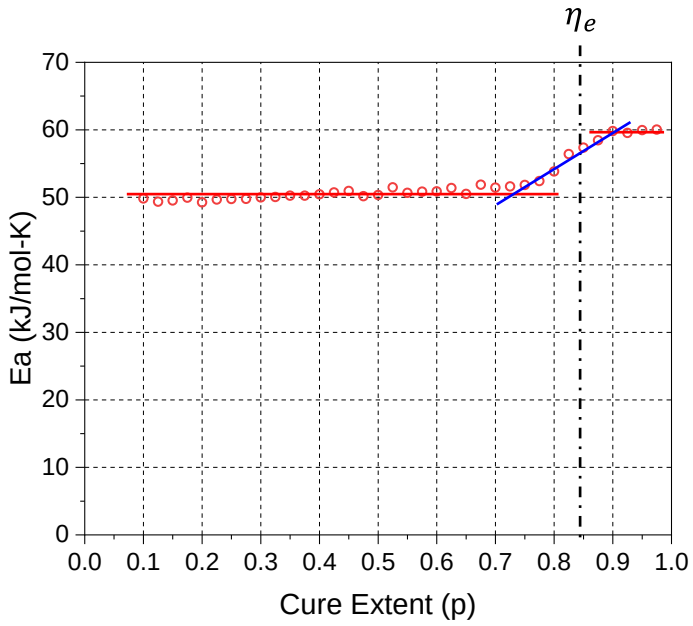


Figure 32 Apparent activation energy as a function of cure extent, obtained from the Friedman analysis.

The results obtained from Step I (a model-free analysis using the Friedman method) is shown in Figure 31. The apparent activation energy as a function of cure extent is shown in Figure 32. Two linear lines representing the activation energies were drawn and the transitions are

connected to help estimate η_e accurately. There is a clear step transition (blue line) of the activation energy, indicating that both reactions are occurring simultaneously in the transition region. The estimated ratio (η_e) was determined as the cure extent at the middle point over the transition region, η_e= 0.85, as indicated in the figure.

It is worth noting that only two data points are used for calculation of the activation energy, although three data points are typically used to minimize the uncertainties associated with the experimental data during slope calculation. The objective of the above calculation was not to determine the activation energy accurately but to just estimate the ratio. This provides a rationale for using two data points for the activation energy calculation.

It is also evident from Figure 32 that the contribution of the second reaction to the overall reaction is nearly negligible until p reaches 0.75; i.e., $dp_2/dt \sim 0$ and $p_2 \sim 0$. Therefore, only the first reaction contributes to the overall reaction when the extent of cure is below 0.75. Likewise, after p = 0.90, the first reaction reaches completion, and the second reaction dictates the heat flow response.

Table 1 Estimated cure kinetics constants of the first and second reactions.

$(E_{a1})_e$ (kJ mol^{-1})	$(A_1)_e$ (s^{-1})	$(n_1)_e$	$(m_1)_e$	η_e
48.61	1.64E+03	1.20	0.20	0.85
$(E_{a2})_e$ (kJ mol^{-1})	$(A_2)_e$ (s^{-1})	$(n_2)_e$	$(m_2)_e$	$1-\eta_e$
57.30	3.29E+03	1.01	0.25	0.15

Using the two data sets ($\beta = 5$ °C/min and $\beta = 10$ °C/min), a set of constants for the first reaction was estimated using Eq. (53), following Step II. The contribution of the second reaction

was determined by Step III. Then, using the two data sets ($\beta = 5$ °C/min and $\beta = 10$ °C/min), a set of constants for the second reaction was estimated using Eq. (54), following Step IV. The results for the estimated constants for the first and second reactions are listed in Table 1.

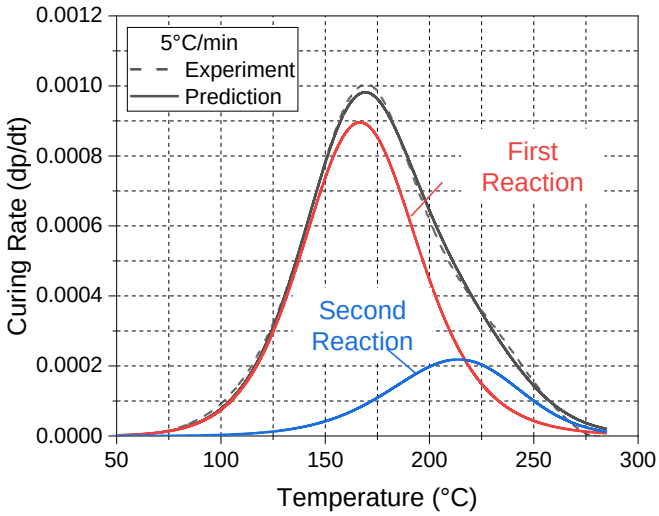
Using the nine initial values in Table 1, a non-linear fitting method utilizing a modified gradient descent method (Nedler-Mead algorithm) [108] was followed to fit the dataset. This algorithm is available as $fminsearch$ or $fmincon$ in MATLAB programming language. The values of the model constants obtained are summarized in Table 2.

The DSC data of $\beta = 5$ °C/min is compared with the predicted values in Figure 33. Figure 33(a) shows the curing rates of two reactions, while (b) shows the cure extents. They show excellent agreement with the overall $R^2 = 0.991$.

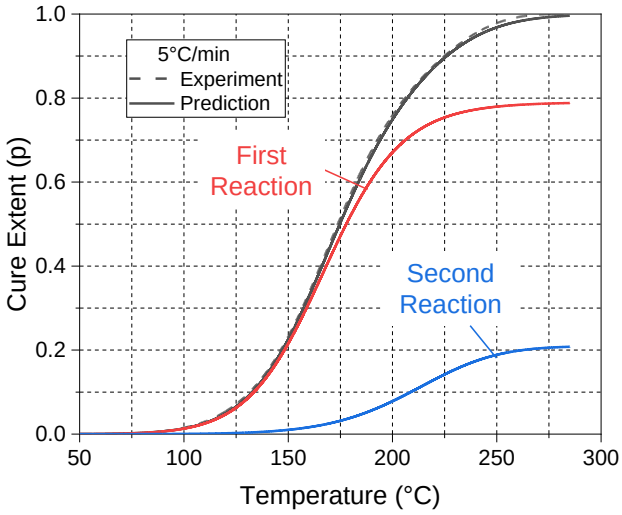
The prediction results can show the contributions of each reaction separately, and they were also included in Figure 6. As mentioned earlier, the second reaction is much weaker than the first reaction. The activation energy of the second reaction is nearly 50 % larger than that of the first reaction. However, the maximum curing rate of the first reaction is more than four times higher than that of the second reaction. Consequently, the second reaction contributes to only ≈ 20 % of the total cure extent. This information can be used effectively to optimize the curing schedule during manufacturing.

Table 2 Final reaction kinetic constants for the underfill material obtained using the proposed method

E_{a1} (kJ mol^{-1})	A_1 (s^{-1})	n_1	m_1	η
45.52	1.00E+03	1.45	0.35	0.79
E_{a2} (kJ mol^{-1})	A_2 (s^{-1})	n_2	m_2	$1-\eta$
62.25	1.08E+04	1.24	0.11	0.21


0.0012
0.0010
0.0008
0.0006
0.0004
0.0002
0.0000
Curing Rate (dp/dt)
5°C/min
Experiment
Prediction
First
Reaction
Second
Reaction
50
100
150
200
250
300
Temperature (°C)

(a)


1.0
0.8
0.6
0.4
0.2
0.0
Cure Extent (p)
5°C/min
Experiment
Prediction
First
Reaction
Second
Reaction
50
100
150
200
250
300
Temperature (°C)

(b)

Figure 33 DSC data of $\beta = 5$ °C/min is compared with the predicted values: (a) the curing rates and (b) the cure extents.

4.6. Discussion

Two extra dynamic scan datasets were obtained at β = 2.5 °C/min and 7.5 °C/min. These datasets were used to further validate the constants obtained from the proposed method. The cure extent obtained from DSC is compared with the predicted cure extent in Figure 34. The predicted values and the experimental data showed excellent agreement with $R^2 > 0.99$, not only at the two heating rates (β = 5 °C/min and 10 °C/min) used to determine the parameters, but also at the two additional heating rates of β = 2.5 °C/min and 7.5 °C/min. The results corroborate the robustness and the accuracy of the proposed method.

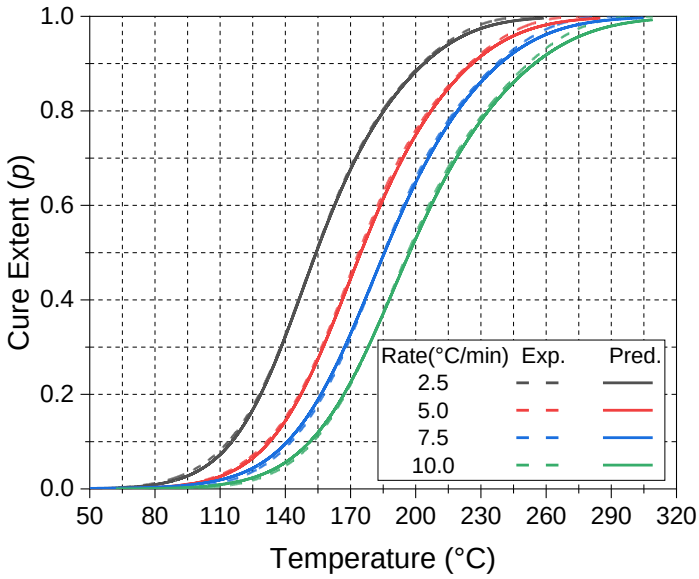


Figure 34 Predicted cure extent is compared with the experimental data. Only data obtain from two dynamic scanning rates - $\beta = 5$ °C/min and 10 °C/min are used to determine the model constants and the additional scan data ($\beta = 2.5$ °C/min and 7.5 °C/min) are used for validation.

Supplementary regression analyses were conducted to illustrate the complexity (i.e., extreme nonlinearity) of Eq. (51). The same Nedler-Mead algorithm-based method was implemented using three different sets of DSC data: - (1) two sets of data (β = 5 °C/min and 10° C/min); (2) three sets of data (β = 2.5 °C/min, 5 °C/min and 10 °C/min); and (3) four sets of data (β = 2.5 °C/min, 5 °C/min, 7.5 °C/min, and 10 °C/min) without pre-determining the initial values (Steps I to IV). The nine constants obtained from the supplementary regression analyses are compared with those obtained from the proposed method. The results are summarized in Table 3. The last row of the table shows the correlation coefficient (R^2) of each case.

Table 3 Comparison of cure kinetics constants obtained from various data sets with arbitrary initial values with the true values obtained for the proposed method

Constants	**(1)***	**(2)**	**(3)**	**(4)**
$\boldsymbol{\eta}$	0.79	0.37	0.49	0.16
$\boldsymbol{E_{a1}}$ **(kJ mol^{-1})**	45.42	32.8	38.6	76.9
$\boldsymbol{A_1}$ **(s^{-1})**	1.00E+03	4.56E+03	3.36E+02	9.45E+07
$\boldsymbol{n_1}$	1.45	0.87	2.16	0.81
$\boldsymbol{m_1}$	0.35	0.23	0.63	0.28
$\boldsymbol{E_{a2}}$ **(kJ mol^{-1})**	62.25	74.20	66.80	44.80
$\boldsymbol{A_2}$ **(s^{-1})**	1.08E+04	9.92E+02	5.89E+03	4.33E+02
$\boldsymbol{n_2}$	1.24	1.67	1.04	1.44
$\boldsymbol{m_2}$	0.11	0.27	0.03	0.23
Correlation coefficient ($\boldsymbol{R^2}$)	0.99	0.97	0.98	0.98

***** Note for Table 3: (1) Proposed method; (2) arbitrary initial points using two data sets; (3) arbitrary initial points using three data sets; and (4) arbitrary initial points using four data sets

The results obtained from the arbitrary initial values deviate significantly from the values obtained from the proposed method regardless of the amount of data used in the regression analyses. This is because the values of the kinetic constants can change significantly from the initial values while the nonlinear multi-parameter minimization converges to a minimum. This iterative process may lead to convergence to local minima rather than a unique global minimum. Therefore, the kinetic parameters obtained may not be unique and could be erroneous if arbitrary initial values are used.

As shown in Table 3, in one case (arbitrary initial points using four data sets), the activation energy of the first reaction was higher than that of the second reaction, which is not physically possible. The correlation coefficients (the last row) are very high in all cases, and thus the results can be completely misleading. This supplementary analysis confirms the rationale behind the proposed approach.

4.7. Conclusions

The cure kinetics of a highly-filled dual-cured epoxy, known as an underfill in the semiconductor packaging, were studied using standard DSC dynamic scan data. The DSC thermograms were used to describe the total reaction, and the contribution of the first reaction to the total reaction was determined in addition to the eight constants of two autocatalytic models that described the dual reactions. The objective function to determine the nine constants simultaneously from DSC data was highly non-linear. Therefore, these nine constants could only be uniquely determined unless a set of initial values that were reasonably close to the true model constants were provided, regardless of the amount of dynamic scan data used in the computation.

To overcome this challenge, a novel method was proposed to obtain the initial values consistently. The method first utilized the well-known Friedman method to determine the activation energy as a function of cure extent, from which the ratio of the first reaction to the total reaction was estimated. This ratio was subsequently used for an analytical approach of the least-squares method to estimate the autocatalytic model constants of each reaction. Then, a non-linear fitting method was applied to obtain the nine constants using the pre-determined initial values.

The proposed method demonstrated excellent efficiency using only two standard DSC dynamic scan datasets (at linear heating rates of 5 °C/min and 10 °C/min) to determine the nine constants correctly. The predicted cure extent was compared with the cure extent obtained from DSC data, not only for the two dynamic scan data but also for two additional dynamic scan data at different rates (2.5 °C/min and 7.5 °C/min). Excellent agreement (with $R^2 > 0.99$) was observed, which corroborated the robustness and accuracy of the proposed method. Extension of this approach to additional applications will be the subject of future work.

Chapter 5 Characterization of Bulk Behavior of EMC

5.1. Background and Motivation

There have been attempts to measure – bulk moduli (K) of a fully-cured polymer as a function of temperature and/or time. Unlike Young's modulus measurements which are routinely done using a commercially available tools like dynamic mechanical analyzer (DMA) and universal tensile test machine (UTTM), bulk behavior is challenging to measure and requires specialized commercial tools or custom designed setups for measurement. This section discusses the tools/ methodologies which have been used to measure the bulk moduli.

5.1.1. Temperature-dependent bulk behavior measurement by P-V-T-C

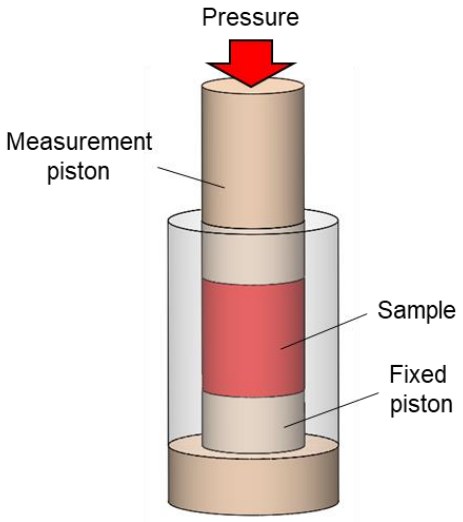


Figure 35 Schematic of a P-V-T/ plunger-based high-pressure dilatometer setup

A high-pressure dilatometer/ P-V-T (pressure-volume-temperature) machine has been used widely to measure temperature dependent bulk moduli. A schematic diagram of a typical P-V-T setup is shown in Figure 35. It consists of a sample coupon, i.e., the material being tested, a plunger

to apply pressure, and a high-resolution LVDT to record piston movements. The mold is typically made of a high-stiffness material like steel, which also acts as an environment chamber. The mold can be heated to various temperature to measure temperature-dependent properties.

This device was originally developed to measure the mold-shrinkage caused by compression molding processes [12, 109]. It was later adopted to measure temperature-dependent coefficient of thermal-expansion (CTE) and compressibility (bulk modulus) of filled molding compounds [38, 49].

With the device, different levels of pressure and temperature are applied to record volumetric displacements ($\Delta V(T,P)$), which can be calculated using the following equation:

$$\Delta V(T,P) = \frac{\pi d_0^2}{4}(h(T,P) - h_0) \tag{55}$$

where d_0 is the inner diameter of the mold, $h(T,P)$ is the height of the specimen at a temperature T and pressure P, and h_0 is the original height of the specimen. A typical volume change data for EMC as a function of temperature and pressure is shown in Figure 36 [110]. The data for volume change is recorded isochronously at each T,P.

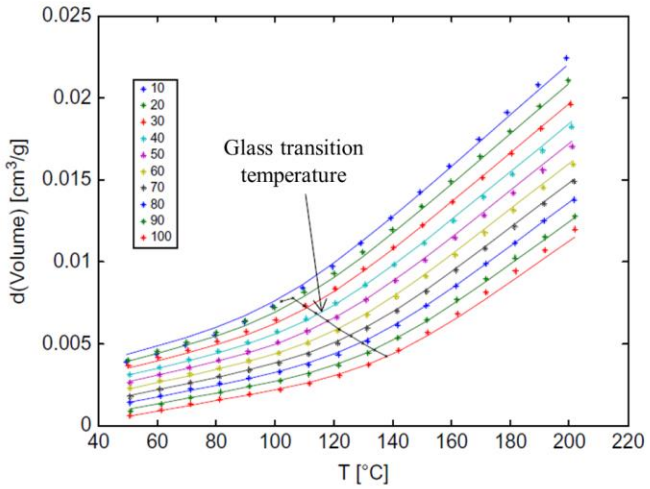


Figure 36 Volume change for EMC in different temperature and pressure for PVT measurement [110]

The governing relationship between volume, temperature and pressure can be expressed using equations of state (known as Tait's equation) as follows [111]:

$$v(T,p) = v''(T)\left[1 - C\left(1 + \frac{P}{b_1 \exp(-b_2 T)}\right)\right]$$
$$v''(T) = \left[1 + k_1\left(T - T_{gp}\right) + \frac{1}{2}k_2\left[\left(T - T_{gp}\right) + \frac{\ln\left(\cosh\left[A_1(T - T_{gp}\right]\right)}{A_2}\right]\right] \quad (56)$$

where $C,\ b_1, b_2, k_1, k_2, A_1, A_2$ are material-specific constants. The experiment data shown in Figure 36 fit into Eq. (56) to obtain the material constants. The compressibility -$B(T)$ and the bulk modulus - $K(T)$ are obtained by taking a partial-derivative of Eq. (56) with respect to pressure.

$$B(T) = -\frac{1}{V}\left(\frac{\partial V}{\partial P}\right)_T$$
$$K(T) = \frac{1}{B(T)} \quad (57)$$

This gives the temperature-dependent elastic bulk modulus of the EMC. It is clear form Eq. (56), that the equations of state have been obtained independent of time and do not consider

time-dependent behavior. Hence, the equations of state cannot be used to determine time-dependent compressibility or bulk modulus.

To incorporate the temperature-dependent bulk modulus - $K(T)$ into FEM, one cannot simply use LVE module as temperature-dependency implies time-dependency due to thermo-rheological simplicity (TRS). However, the implementation is modified using user-defined function using the following equations [49]:

$$\boldsymbol{\sigma} = \boldsymbol{s} + \boldsymbol{\sigma_v}$$

$$\boldsymbol{s} = 2G_\infty \boldsymbol{e} + 2\left[G_g - G_\infty\right] \sum_{i=1}^{N} g_i \boldsymbol{q_i}\,;\, \dot{\boldsymbol{q}}_{\boldsymbol{i}} + \tau_i \boldsymbol{q_i} = \dot{\boldsymbol{e}}_{\boldsymbol{i}} \tag{58}$$

$$\boldsymbol{\sigma_v} = K(T)\boldsymbol{\varepsilon_v}$$

where σ, s and σ_v are the total, deviatoric and volumetric stress tensors, respectively. e and ε_v are shear strain and volumetric strain tensors, respectively.

In the above analysis, the volumetric and shear tensors are evaluated separately and added together to give the total stress. Here, the shear stress is evaluated based on the Prony series but the volumetric stress is treated as elastic and evaluated based on the elastic bulk modulus values at a given temperature. Hence, the volumetric component of the stress does not exhibit time-dependent behavior.

5.1.2. Time-dependent bulk behavior measurement by embedded fiber Bragg grating (FBG)

More recently, a cylindrical polymer specimen with an embedded glass fiber Bragg grating (FBG) was used to measure the viscoelastic bulk moduli of EMC while subjecting the FBG-specimen assembly to high hydrostatic pressure produced by an inert gas [58, 59]. The FBG is made of glass fiber, and it is an ideal sensor for the measurements because it is robust enough to

handle the harsh manufacturing environment, i.e., high temperature and pressure with presence of corrosive chemicals.

Although the method was innovative and the results indeed exhibited clear time-dependent bulk behavior, a couple of technical challenges were realized during its implementation. These issues are discussed in detail below, as they are directly or indirectly related to a novel method proposed in this thesis.

Brief Description of FBG-based method

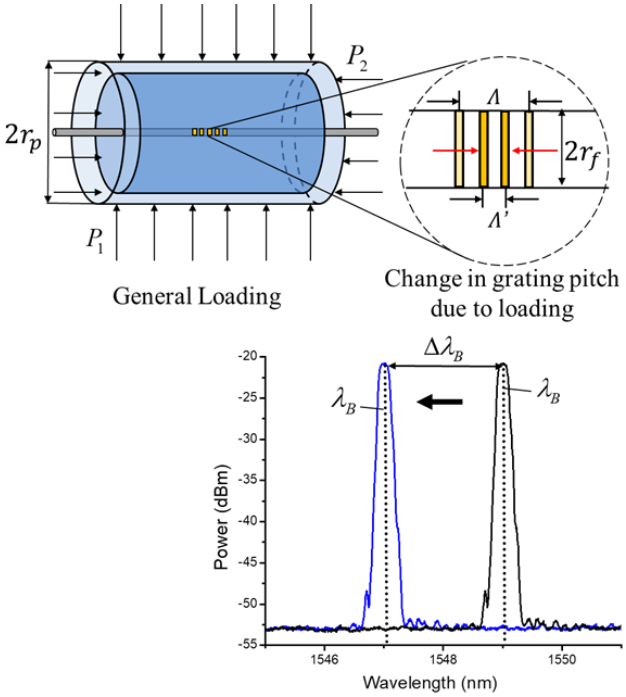


Figure 37 FBG embedded specimen subjected to mechanical loading for measurement of mechanical properties

A fiber Bragg grating (FBG) is an optical strain sensor that offers very high sensitivity ($\approx 1\mu\varepsilon$). It is extremely robust, as it is fabricated on a glass fiber. It can be embedded inside the EMC during curing process, as illustrated in Figure 37. Mechanical properties can be measured

by embedding an FBG sensor inside EMC [29]. For an isotropic and straight Bragg grating, the effective refractive index can be expressed using the following equation:

$$\Delta n_{eff} = -\frac{n^2}{2}\left[P_{12}\varepsilon_1 + (P_{11}+P_{12})\varepsilon_2 - \left\{\frac{2}{n^3}\frac{dn}{dT} + (P_{11}+2P_{12})\alpha_f\right\}\Delta T\right] \tag{59}$$

where ε_2 is the transverse strain, P_{ij} are the strain-optic coefficients (Prockel's coefficients), dn/dT is the thermal-optical coefficient, α_f is the CTE of the fiber core material, and ΔT is the temperature change. For the uniaxial loading where $\varepsilon_2 = -\nu\varepsilon_1$ with no temperature change, the equations can be simplified as:

$$\Delta\lambda_b = \lambda(1-P_k)\varepsilon_1 \tag{60}$$

where P_k is defined as $P_k = -\frac{n^2}{2}[P_{12} - \nu(P_{11}+P_{12})]$; ν is the Poisson's ratio of the fiber material. This shows the linear relationship between the applied strain and the BW change.

When both temperature and mechanical loading are incorporated in the grating, the BW shift can be expressed as:

$$\Delta\lambda = \Delta\lambda_i + \Delta\lambda_d \tag{61}$$

where $\Delta\lambda_i$ is the BW change by the temperature; $\Delta\lambda_d$ is the BW change caused by the mechanical loading. They can be expressed as [23, 112]:

$$\Delta\lambda_i = \lambda_d\left[\left(\alpha_f + \frac{1}{n_{eff}}\frac{dn}{dT}\right)\Delta T + \frac{1}{n_{eff}}\frac{dn}{dT}\alpha_f\Delta T^2\right]$$

$$\Delta\lambda_d = \frac{1}{E_f}\left\{\left[1 - \frac{n^2}{2}\left(P_{12} - (P_{12}+P_{11})\nu_f\right)\right]\sigma_{zz}^f - \left[2\nu_f + \frac{n^2}{2}\left((1-\nu_f)P_{11} + (1-3\nu_f)P_{12}\right)\right]\sigma_{rr}^f\right\} \tag{62}$$

where E_f and ν_f are the Young's modulus and Poisson's ratio of fiber respectively. σ_{zz}^f and σ_{rr}^f are the axial and radial stresses acting on the Bragg grating.

When EMC is subjected to axial and/or radial loading (P_1 and P_2), the pitch of the grating (Λ) and its effective refractive index (n_{eff}) changes to due to applied stresses. This causes change in the Bragg wavelength (BW) signal which can be used to calculate the mechanical properties of EMC.

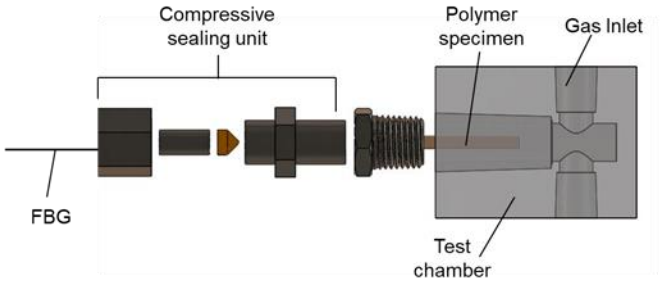


Figure 38 Schematic of hydrostatic testing chamber assembly

For measurement of bulk behavior, the fabricated FBG embedded EMC specimen is placed inside a metal chamber, and it is sealed using a compressive sealing unit as shown Figure 38. The gas inlet of the chamber is connected to pressure transducer and the high-pressure cylinder through a pressure regulator. Upon application of the pressure signal, the regulator valve opens and the high-pressure gas flows into the chamber till the set pressure is achieved, and the BW change ($\Delta\lambda_b$) is recorded. Then, the bulk modulus is obtained from the BW signal using a non-linear governing equation based on an elastic solution [58]:.

5.1.2.1. Heat generation induced by gas

The gas undergoes acceleration between the reservoir and the chamber due to the large pressure differential, followed by sudden stagnation in the chamber along the chamber walls and the specimen surface. The entire pressurization process last about 500-900 ms (from 0-1000 psi) and the sudden compression and stagnation causes large heat generation within the chamber.

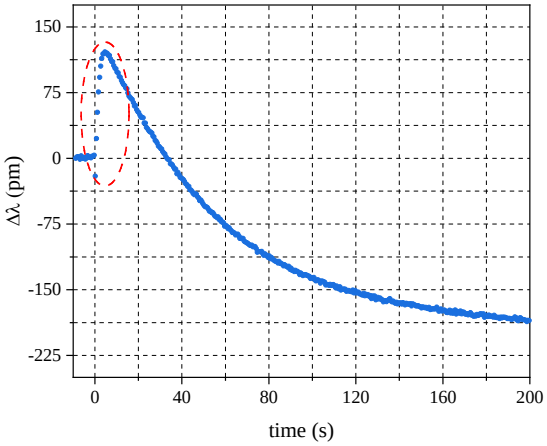


Figure 39 BW signals demonstrating the effect of heat generation due to the instantaneous pressure application

This effect of heat generation is illustrated in Figure 39. An FBG embedded EMC specimen (D = 4.5 mm) was placed in a chamber and subjected to an instantaneous gas pressure of 500 psi. The y-axis value indicates the Bragg wavelength (BW) change, which is directly related to the EMC strains. The initial increase marked by a red circle is the evidence of heat generation. Without the heat generation, the BW signal would decrease after a pressure is applied (t = 0).

The part of data affected by the heat generation was ignored in the previous practice, which extended the testing time significantly. For example, if the effect of heat generation lasts for 10 seconds, additional testing of 100 seconds is required to one decade of data in the log scale. In fact, although theoretically possible, it is extremely difficult to the distinguish the temperature effect from the creep data in practice, which can lead to erroneous bulk modulus measurements.

This detrimental effect of heat generation for hydrostatic testing will be exacerbated for testing in T_g region where large amount of creep behavior is observed. The main cause of the heat generation is sudden stagnation and compression of the incoming inert gases along the chamber walls and the specimen. The rapid heat transfer from the gas to the specimen due to the high heat

transfer coefficient causes significant and noticeable change in the BW signal upon pressure application. The total amount of pressure applied, time for pressure application and ambient temperature of testing also directly affect the amount of temperature rise in the chamber.

The inert gas used for testing (He or Ar) as well as the total volume of the chamber affect the total amount of thermal energy introduced into the system. This is because the two gases have significantly different thermodynamic and material properties (density, heat capacity, viscosity, etc.). Finally, the thermal properties of the chamber and the specimen affect the total share of heat absorbed by chamber and specimen, respectively, and the amount of time it takes to dissipate the heat and reach an equilibrium condition.

5.1.2.2. Errors associated with the governing equations used to determine bulk modulus

Embedding a glass fiber inside a cylindrical EMC coupon made the assembly inherently a composite structure, and thus the BW signals did not present a pure hydrostatic response in spite of the hydrostatic loading provided by an inert gas. The stresses on the glass fiber were caused by the multiaxial loading conditions induced by the applied pressure. Thus, in the first bulk modulus application, the temperature-dependent bulk modulus is obtained from the BW signal using the following non-linear equation based on an elasticity solution [58]:

$$K(T) = \Pi(\Delta\lambda_b(T), \beta, E(T))P \tag{63}$$

The temperature dependent Young's modulus $E(T)$ was required to calculate $K(T)$ from the BW signal.

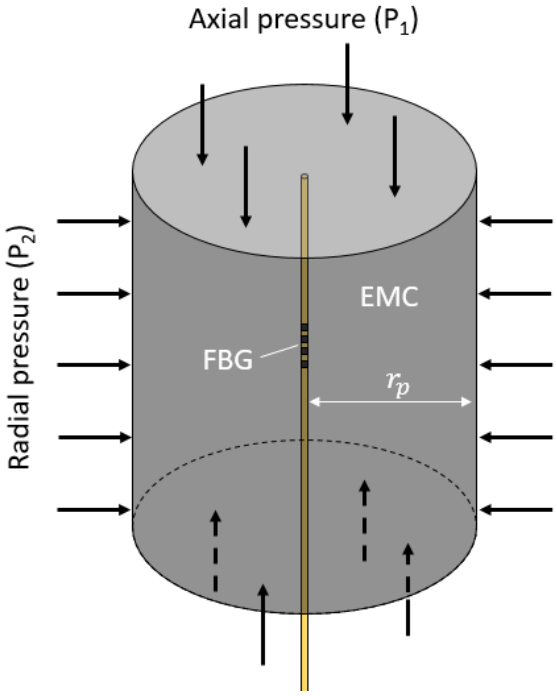


Figure 40 Schematic of a polymer specimen with embedded FBG under axial and radial loading

This approach was extended later for measurements of time-dependent behavior [58], which used the following relationship, still based on the elastic solution:

$$K(t,T) = \Pi(\Delta\lambda_b(t,T), \beta, E(t,T))P \qquad (64)'$$

This extension into the viscoelastic domain had a fundamental flaw. The governing equation based on an elastic solution will not be valid for viscoelastic behavior. The errors associated with Eq. can be significant, especially when a large viscoelastic behavior (around T_g).

5.2. Proposed Method

A novel method is proposed to measure viscoelastic compressibility/bulk moduli as a function of time and temperature -$B(t,T)$ and $K(t,T)$. The method utilizes the inert-gas based

pressure application, but uses a radically different loading profile to achieve the goal while negating the effect of heat generation produced by the gas.

5.2.1. Determination of optimum loading profiles to negate the heat generation

In a typical time-domain testing for compressibility, $B(t)$, or bulk modulus, $K(t)$, measurement, a constant strain or a stress is applied, and the viscoelastic response is recorded as a function of time, the compressibility or bulk modulus can be obtained directly from the measured data.

$$B(t) = \frac{\varepsilon(t)}{\sigma_0}$$
$$K(t) = \frac{\sigma(t)}{\varepsilon_0} \tag{65}$$

The main advantage of this method is measurement of the property is relatively simple. Although theoretically sound, in practice however, instantaneous load application is not possible. More importantly, the amount of heat generated due to high rate of loading (>7MPa/s) makes it extremely difficult to decouple CTE induced response to that of hydrostatic creep. Thus, it is practically very difficult to implement this method using inert gases.

To mitigate with the temperature issues of instantaneous loading, the rate of pressure application ($\Delta P/\Delta t$) needed to be reduced. In this section, various pressure profiles for load application have been demonstrated using a standard linear solid (SLS). The calculations involved in a SLS can be extended to a general Maxwell model without any loss of generality. The advantages and disadvantages in using each loading profile have been discussed and an optimum loading profile is chosen for the measurements.

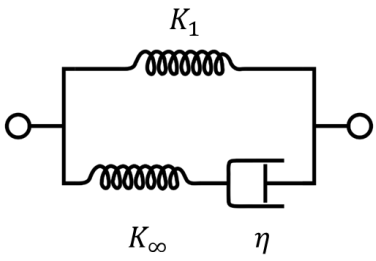


Figure 41 A illustration of a standard linear solid (SLS) using a spring-dashpot model.

Standard linear solid (SLS)

In a standard linear solid (SLS) as illustrated in Figure 41, the relaxation modulus and creep compliance can be expressed as [113]:

$$K(t) = K_\infty + K_1 \exp\left(-\frac{t}{\tau_1}\right); K_g = K_1 + K_\infty$$
$$B(t) = B_g + \left(B_\infty - B_g\right)\left(1 - \exp\left(-\frac{t}{\tau_c}\right)\right); B_g = \frac{1}{K_g}, B_\infty = \frac{1}{K_\infty}, \tau_c = \tau_1\left(\frac{B_g}{B_\infty}\right) \quad (66)$$

The bulk moduli - $K(t)$ and compressibility - $B(t)$ are inter-convertible in linear viscoelasticity using the convolution integral shown below:

$$\int_0^t B(t-\tau)K(\tau)\,d\tau = t \quad (67)$$

An analytical relationship between $K(t)$ and $B(t)$ exists for a SLS as described in Eq. (66). The integral have to be evaluated numerically for inter-converting between the properties with n-Prony terms [113].

Pure linear loading

In this method, pressure is applied linearly at a low but constant rate ($\dot{P}$) until the target pressure. The compressibility cannot be directly calculated by taking the ratio of strain to stress at each point. The polymer being viscoelastic exhibits history dependent behavior and hereditary

integral is needed to be able to relate strain response to the applied pressure at a particular time. The time-dependent compressibility can be calculated using the following equations:

$$\varepsilon_h(t) = \frac{1}{3}\left[\sigma(0)B(t) + \int_{0^+}^{t} B(t-\tau)\frac{dP(\tau)}{d\tau}d\tau\right]$$

$$\varepsilon_h(t) = \frac{\dot{P}}{3}\left(B_\infty t - \left(B_\infty - B_g\right)\tau_c\left(1 - \exp\left(-\frac{t}{\tau_c}\right)\right)\right) \tag{68}$$

$$\frac{3}{\dot{P}}\frac{d\varepsilon_h(t)}{dt} = \left(B_\infty - \left(B_\infty - B_g\right)\left(\exp\left(-\frac{t}{\tau_c}\right)\right)\right) = B(t)$$

The main advantage of the method is that the creep-response although being governed by hereditary integral simplifies due to the linear rate of loading. The compressibility can be calculated by simply taking the ratio of strain-rate ($\dot{\varepsilon_h}$) to the pressure application rate ($\dot{P}$) at a given time. However, for practical application, the upper limit of the pressure is usually restricted due to the pressure rating of the components used. Additionally, taking numerical derivative of the experimental data can cause significant errors due to the noise in the system.

Linear loading and unloading

For linear loading and unloading, the loading conditions will be from $t = 0$ to $t_0/2$, $\dot{P} = \dot{P}_r$ and $t = t_0/2$, $\dot{P} = -\dot{P}_r$

For $t \leq t_0/2$:

$$\varepsilon_h(t) = \frac{\dot{P}}{3}\int_0^t B(t-\tau)d\tau$$

$$\varepsilon_h(t) = \frac{\dot{P}}{3}\left(B_\infty t - \left(B_\infty - B_g\right)\tau_c\left(1 - \exp\left(-\frac{t}{\tau_c}\right)\right)\right) \tag{69}$$

For $t > t_0/2$ to t_0:

$$\varepsilon_h(t) = \frac{\dot{P}}{3}\left(B_\infty(t_0 - t) + \left(B_\infty - B_g\right)\tau_c\left(1 - 2exp\left(-\frac{t-\frac{t_0}{2}}{\tau_c}\right) + exp\left(-\frac{t}{\tau_c}\right)\right)\right) \quad (70)$$

In case of linear loading and unloading, the equations no longer remain simple like the previous case. One cannot directly obtain the compressibility from the experimental data. The Eq. (69) and (70) need to be solved using a numerical program to determine the values.

For practical application, the pressure regulators need to be programmed for both load application and load removal which requires a complex control system and regulators designed for both pressure application and removal. Additionally, the pressure values will change continuously and the noise to signal ratio would be higher compared to constant pressure. The total amount of creep will be smaller compared to the constant pressure case as the pressure is being changed at each time step.

Linear loading plus constant loading

For linear loading and constant pressure, the loading conditions will be from $t = 0$ to t_1, $\dot{P}_r$=$\dot{P}$ and $t = t_1$ to t_0, $P = P_0$

For $t < t_1$:

$$\varepsilon(t) = \frac{\dot{P}}{3}\int_0^t B(t-\tau)d\tau$$

$$\varepsilon(t) = \frac{\dot{P}}{3}\left(B_\infty t - \left(B_\infty - B_g\right)\tau_c\left(1 - \exp\left(-\frac{t}{\tau_c}\right)\right)\right) \quad (71)$$

For $t > t_1$ to t_0:

$$\varepsilon(t) = \frac{\dot{P}}{3}\int_0^{t_1} B(t-\tau)d\tau \quad (72)$$

$$\varepsilon(t) = \frac{\dot{P}}{3}\left(B_\infty t_1 - (B_\infty - B_g)\tau_c\left(\exp\left(-\frac{t-t_1}{\tau_c}\right) - \exp\left(-\frac{t}{\tau_c}\right)\right)\right)$$

In this case, a pressure at a known linear rate is applied and held constant for a period of time to record creep data as a function of time. Here also the data needs to be fit numerically to obtain the compressibility values from the experimental data. The constant pressure allows for recording of creep as a function of time. The required level of pressure can be smaller than the linear loading case. This pressure profile has been used to determine bulk behavior of the EMC in this work. A derivation and demonstration of a proof-of-concept for a general n-chain model is in the next section.

5.2.2. Analytical derivation for an n-chain model for linear + constant loading

For a general polymer like EMC, the viscoelastic behavior is expressed using a master curve which consists of n −chains represented by generalized Maxwell model, the viscoelastic property - $B(t)$ can be expressed using a Prony series:

$$B(t) = B_g + \sum_{i=0}^{N} B_i\left(1 - \exp\left(-\frac{t}{\tau_i}\right)\right); B_\infty = B_g + \sum_{i=1}^{N} B_i \qquad (73)$$

The relationship between hydrostatic strains and applied pressure can be expressed using the following hereditary integral:

$$\varepsilon_h(t) = \frac{1}{3}\int_0^t B(t-\tau)\frac{\partial P}{\partial \tau}d\tau = \frac{1}{3}\int_0^t \left(\sum_{i=1}^{N} B_i(1 - \exp\left(-\frac{t-\tau}{\tau_{c_i}}\right) + B_g\right)\frac{\partial P}{\partial \tau}d\tau \qquad (74)$$

For a general loading condition, the hereditary integral needs to be evaluated numerically to determine the evolution of pressure and strain over time. The experimental data obtained from hydrostatic testing is fitted to the data set - $P(t)$ vs. $\varepsilon_h(t)$ to obtain the $B(t)$. Under pressure

loading at linear rate of $\dot{P} = -\dot{P}_r$ for time $t = t_1$ followed by constant pressure $P = P_{t_1}$, the hereditary integral simplifies, and relationship can be determined analytically.

During linear loading part of pressure application, i.e., $t = 0$ to t_1 using pressure application rate of $dP/d\tau = \dot{P}$, the relationship between $\varepsilon_h(t)$ vs. $P(t)$ can be calculated as follows:

$$\varepsilon_h(t) = \frac{1}{3}\dot{P}\left(B_\infty t - \sum_{i=1}^{N} B_i \tau_c (1 - \exp\left(-\frac{t}{\tau_{c_i}}\right)\right) \tag{75}$$

For constant pressure part of the load application, $dP/d\tau = 0$ i.e, pressure is constant, the relationship between $\varepsilon_h(t)$ vs. $P(t)$ can be calculated as follows:

$$\varepsilon_h(t) = \frac{1}{3}\dot{P}\left(B_\infty t_1 - \sum_{i=1}^{N} B_i \tau_{c_i}\left(\exp\left(-\frac{t - t_1}{\tau_{c_i}}\right) - \exp\left(-\frac{t}{\tau_{c_i}}\right)\right)\right) \tag{76}$$

The Eq. (75) and (76) will be used for determining compressibility from the applied pressure and measured strain data.

In a general Prony series, the time-constants can theoretically range from $(-\infty, +\infty)$. It is a common practice in viscoelasticity to choose the time-constants with decade intervals to capture the behavior accurately i.e., $\tau_{c_i} = 10^{-n}$ to 10^{m}. For $t \gg \tau_{ci}$, the chains associated with small time-constants will practically relax completely and will not contribute to the actual strain data (due to the limitation of the data recording system). On the other hand, for $t \ll \tau_{ci}$, the rate of relaxation is too small and hence the chains associated with those time-constants will effectively act as pure springs and contribute to the unrelaxed component.

5.2.3. Methodology to determine compressibility Prony series constants from the experimental data

Eq. (75) and (76) are a system of linear equations with respect to the Prony series constants - $B_1, B_2 \dots B_{n-1}, B_n$ and B_∞, which makes the system of equations convex in nature. For an over-deterministic problem, i.e., the number of data points (M) > number of variables (N), the equations would yield a single solution. The solution will always converge to a unique global minimum (the proof of uniqueness can be found in Appendix).

Extra caution should be given while interpreting the uniqueness of a solution of system of linear equations. The system of equations will converge to a global minimum only when the data set being used covers the entire domain (time range) of the master curve (from glassy to rubbery region). If only a subset of data is being used, the equations will only converge to a solution, which best fits to the input data set. The solution may not work outside the range of data set. Hence, for using this method, the testing needs to be conducted over the entire range of the master curve before determining the constants. The effect of using a single data set for calculation of compressibility at one temperature vs. the entire data set has been discussed in Section 5.4.2.

The objective function for fitting to the data set is such that the sum of squared error (SSE) between the experimental strain data ($\varepsilon_{h,exp}(t)$) and the predicted strain data ($\varepsilon_{h,pred}(t)$) is minimized as follows:

$$\text{Minimize S} = \sum_{j=1}^{M} \left(\varepsilon_{h,exp}\,(t) - \varepsilon_{h,pred}(t)\right)^2 \tag{77}$$

The predicted strain data is calculated using the Prony series of compressibility - $B(t)$ and the hereditary integral in Eq. (75) and (76). For an n-chain model, the range of decades is very large and the tests are conducted over several temperatures to collect data over the entire range.

Shift-factors ($\log a_T$) are used to accelerate/decelerate the rate of relaxation for a given temperature. The Prony series of compressibility is as follows:

$$B(t) = B_g + \sum_{i=1}^{N} B_i \left(1 - \exp\left(-\frac{t}{a_T \tau_{ci}}\right)\right) \tag{78}$$

where a_T is the shift-factor already obtained form the Young's modulus measurements. An optimization program was written in MATLAB based on the minimizing SSE described in Eq. (77). It was used to determine the Prony series constants, i.e., compressibility as a function of time.

Table 4 A 5-term Prony series compressibility model to demonstrate the program

i, T_i	0 (Glassy)	1	2	3	4	5
B_i	0.001	0.01	0.02	0.03	0.02	0.01
τ_i		1E-2	1E-1	1E+0	1E+1	1E+2
$\log a_T$		-5	-2.5	0	1.5	3

A proof-of-concept of the optimization program has been demonstrated using a 5-chain compressibility Prony series and simulating a virtual experiment based on linear+ constant loading. The Prony series and a set of shift-factors ($\log a_T$) used for demonstrating the methodology is shown in Table 4. A virtual experiment was conducted in which a pressure was initially applied linearly at a rate of $\dot{P} = -1$ unit/s for 100 seconds and held constant for additional 250 seconds.

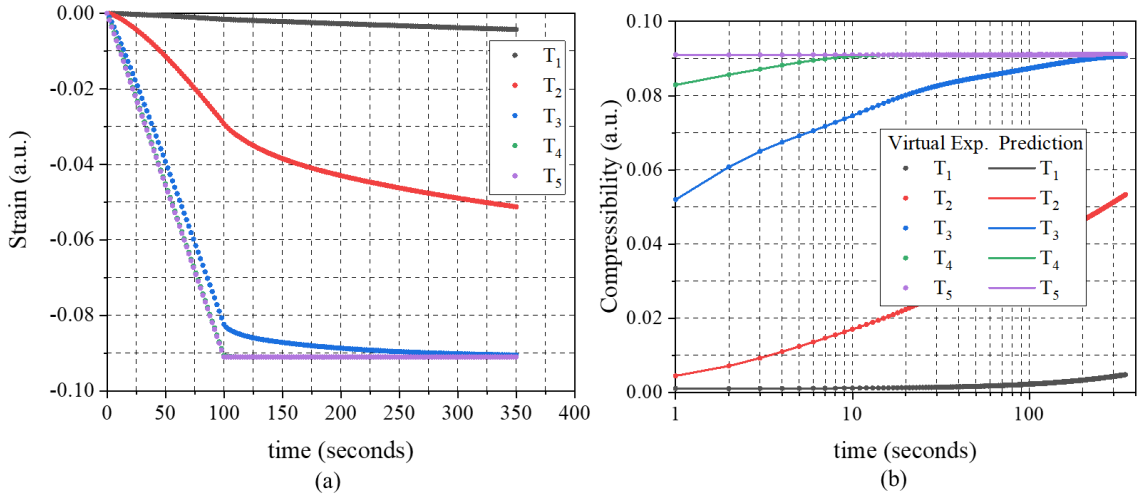


Figure 42 Results of the virtual experiment and the optimization program to determine $B(t)$ – (a) Strain data as a function of time, and (b) comparison of the compressibility values used vs the values obtained from optimization program

The hydrostatic strain as a function of time generated form the virtual experiment is shown in Figure 42 (a). Using the "data" from the virtual experiment as the strain data for the optimization program, the compressibility values have been recalculated as a function of time. A comparison between the calculated compressibility values and the input values is shown in Figure 42 (b). The values are virtually identical indicating that the optimization program works very well. This optimization program will be used to determine compressibility from the actual experimental data in the implementation section.

One of the main advantages of using this methodology is the direct determination of the entire material function as Prony series of compressibility from the set of data. One requirement for this methodology is that the shift-factors have to be known and measured beforehand.

As discussed previously, the shift-factors ($\log a_T$) are required to be able to calculate compressibility at various temperature using the Prony series function. The next section first briefly discusses measurement of viscoelastic Young's modulus using dynamic mechanical

analyzer (DMA). The multi-frequency temperature (MFT) sweeping data has been used to generate a frequency-domain master curve by TTS shifting. The corresponding shift-factors have been used in the implementation section to determine compressibility from the experimental data.

5.3. Implementation of the Proposed Method

5.3.1. Description of the testing apparatus

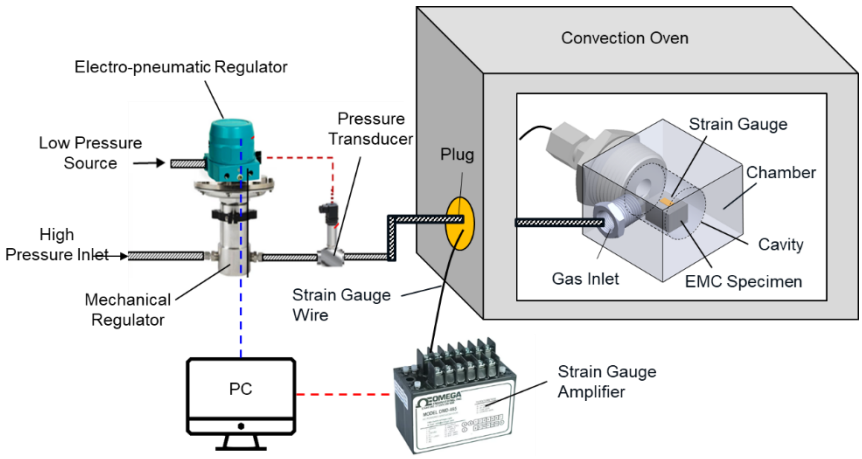


Figure 43 A schematic drawing of the hydrostatic test setup designed to measured time-dependent bulk behavior

A schematic of the complete test setup used for the experiments is shown in Figure 43. Hydrostatic testing chamber similar to the one used for FBG specimen testing [59, 114] was used for the experiment. The specimen was inserted inside the test chamber for the period of testing to be subjected to hydrostatic pressure. The sealing was achieved using a custom designed compressive sealing unit (Conax MPG -T-140). The allowed for sealing the inert gas while allowing the instrumentation cables (30-AWG Cu wires) to send the voltage signal from the strain gauge to communicate with the outside world. The voltage signal was passed through a signal conditioner and amplifier unit (Omega DMD-465) to the data acquisition unit (DAQ NI-4312) for

recording to the computer. Additionally, a shunt resistor circuit based on high-precision resistors was designed to calibrate the strain signal based on simulated maximum load to determine the amplification factor.

To achieve an accurate linear pressure rate, a fast response pressure application system with a feedback program was required to control the pressure rate. The schematic of the pressure application system is shown in Figure 43. It consists of a high-pressure mechanical regulator (TESCOM 2600-5000) which was controlled by a fast response electro-pneumatic pressure controller (TESCOM ER-3000). A high accuracy pressure transducer (TESCOM 1610) monitored the pressure on the chamber side while provide feedback to the control loop. A control routine using LABVIEW software was developed to achieve a desired pressure rate during the testing.

The chamber was kept inside an environment chamber to control and maintain the temperature during the testing. The temperature was continuously recorded and controlled using the LABVIEW program.

5.3.2. Fabrication of EMC specimen

A cuboidal EMC specimen of dimension 20 mm (length) x 10 mm (width) x 10 mm (height) was fabricated for testing. The specimen dimension was chosen considering the size of the strain gauge and thickness required to ensure complete strain transfer from specimen to the strain gauge, i.e., a negligible reinforcement effect across the entire temperature range.

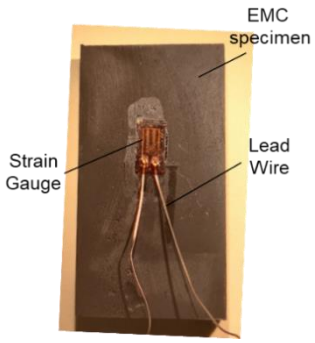


Figure 44 EMC specimen with the strain gauge attached fabricated for hydrostatic testing

A strain gauge was attached to the fully-cured specimen using a high-temperature bonding adhesive (VPG M-bond 610). An adhesive curing profile suggested by the manufacturer (VPG) was followed to attach the strain gauge to the specimen. The fabricated EMC test specimen with a strain gauge is shown in Figure 44. An instrumentation wire coated with high-temperature silicone (30 AWG) was soldered onto the lead wires for strain measurement. The specimen was then inserted into the hydrostatic test chamber for testing.

The strain gauge on an EMC specimen will be subjected to hydrostatic creep loading (constant pressure) at various temperatures (as high as 250 °C). The strain gauge expands along with the EMC due to the thermal expansion of EMC. Considering the typical values of coefficient of thermal expansion (CTE) of EMC, it is expected that the strain gauge will have the maximum strain of ~0.7%. A strain gauge suitable for the temperature range – 20°C to 250°C and a large strain range (~ 3%) was selected for testing (VPG: WK-05-062AP-350).

5.3.3. Measurement data

Initial testing was conducted to demonstrate the working on the setup which involved application of pressure and recording the strain data synchronously using the LABVIEW program. The tests were conducted at room temperature with a strain gauge attached to a known elastic

material. The results obtained are shown in Figure 45 (a), where a pressure rate of 5 psi/s (0.03445 MPa/s) was used and time-dependent measurements were made at two final pressure levels of 450 psi (3.10 MPa) and 900 psi (6.20 MPa).

The strain vs pressure signal during the ramp period is shown in Figure 45 (b). The linear relationship further confirms that the effect of heat generation was completely negated and this the strain gauge response was directly proportional to the applied pressure signal. The linear response was expected as the material was elastic at the room temperature.

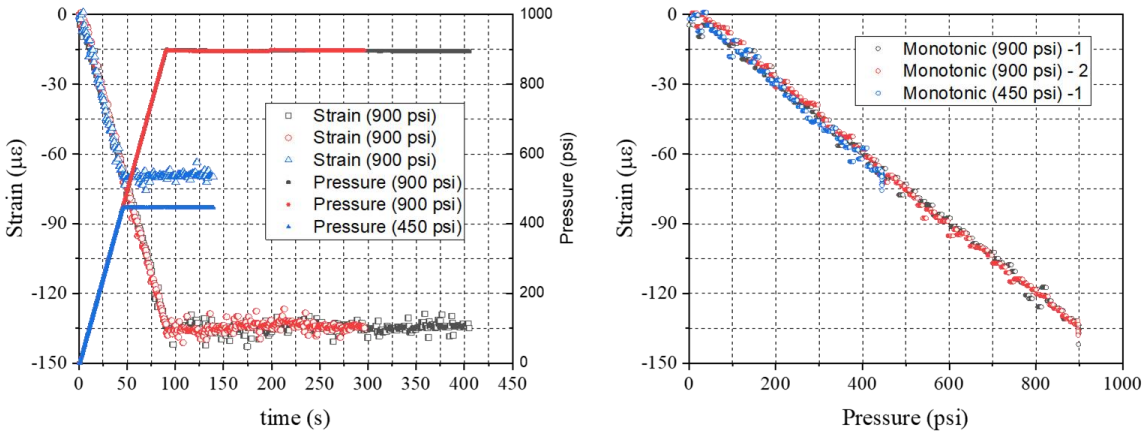


Figure 45 Hydrostatic testing at room temperature – (a) pressure and strain as a function of time, (b) strain vs. pressure (psi) over the linear ramp period.

In contrast to the Young's modulus measurements which were done in the frequency domain, the hydrostatic measurements were conducted in the time-domain. Due to practicality in time for measurements and the limitation of the instrumentation system, a single temperature could not be used to determine the entire master curve due the range of time-scales involved. It was thus essential to determine a set of test temperature and times for testing such as to get a near continuous master cure for bulk modulus.

The sampling rate of the system was limited to 0.1 seconds (10 Hz) and any changes smaller than this time-scale couldn't be captured effectively. At a given test temperature, the longer the time for testing, the more data we acquire on a decade scale. However, law of diminishing returns comes to play when the time-scales become larger as the amount of data acquired on a single decade can take 10-fold amount of time on a linear scale. At one point it is just faster to heat the system to a higher temperature and accelerate the rate of relaxation to gain additional data.

Thus, for the current experiment, the maximum time for testing was limited to 350 seconds (~2.5 decades). Testing beyond this time would be inefficient with the test apparatus as it would take another 650 seconds to just get additional 0.5 decade of data. The time-taken to heat the system to a higher temperature for additional testing is faster and would result in more decades covered compared to waiting for additional 650 seconds or more to gather data.

A set of shift-factors ($\log a_T$) and the master curve for Young's modulus was already determined through the viscoelastic Young's modulus measurements. Fundamentally, the shift-factors determined from Young's modulus would remain unchanged for a material and would be applicable to the bulk modulus as well.

The time-scale of the Young's relaxation modulus was used as a reference to determine the temperatures and time for testing such as to get a near contiguous master curve. The glassy and equilibrium values of $E(t)$ - $E_0 = 22.6$ GPa and $E_\infty = 0.59$ GPa along with the glassy and rubbery Poisson's ratio's available in the literature - $\nu_0 = 0.2 - 0.3$ and $\nu_\infty = 0.43 - 0.47$, an estimation was made for the expected glassy and rubbery values of bulk modulus - $K_0 \sim 14$ GPa and $K_\infty \sim 4$ GPa.

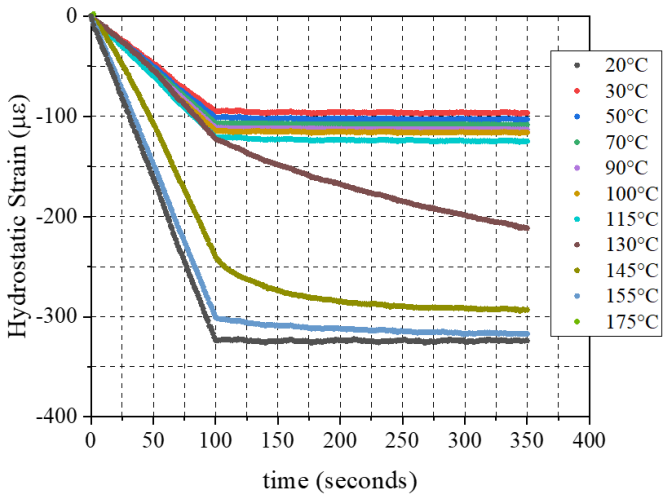


Figure 46 Raw experimental hydrostatic strain data at various temperatures of testing

Three levels of steady-state pressure were chosen – 750 psi (20-110°C), 500 psi (110-140°C) and 250 psi (150°C and above) so as to have approximate similar levels of strain across the all the temperatures. It is to be noted that these levels were chosen purely based on single expected value and do not account for the creep. The test was conducted at various temperatures from 20°C to 200°C. The raw strain data are shown in Figure 46.

As expected, the time-dependent behavior was small below T_g (below 110°C). Within the T_g region (110-150°C), large time-dependent strains were observed indicating large changes in bulk behavior. Beyond the T_g region (above 150°C), the retardation rate was very fast and the EMC showed small creep behavior.

5.3.4. Data analysis and compressibility calculations

As discussed previously, when loading (creep) or deformation (stress relaxation) is applied instantaneously and maintained, the creep compliance or the relaxation modulus can be obtained

directly from the ratio of the material response to the applied load or strain. For a general time-dependent loading, the material response is governed by the hereditary integral described in Eq. (71). The hereditary integral has to be solved and fit to the data set to obtain the compressibility - $B(t)$.

Additionally, the data is obtained at various temperatures, and the shift-factors ($\log(a_T)$) have to be utilized to be able to accelerate or decelerate the time-scales on a log-plot for generating a master curve. The shift-factors determined from Young's modulus master curve are directly utilized in the compressibility calculation program.

5.3.4.1. Viscoelastic Young's modulus measurement

Viscoelastic Young's modulus measurements are first conducted using DMA to obtain the master curve and the corresponding shift-factors. Dynamic mechanical analyzer (DMA) is widely used to characterize viscoelastic properties. A sinusoidal displacement (strain) is applied to a material sample using a very sensitive displacement sensor, based on linear variable differential transformer (LVDT) or an optical encoder, and the force (stress) response is measured using a high resolution loadcell. The phase lag between the stress and strain governs how viscoelastic a material behaves.

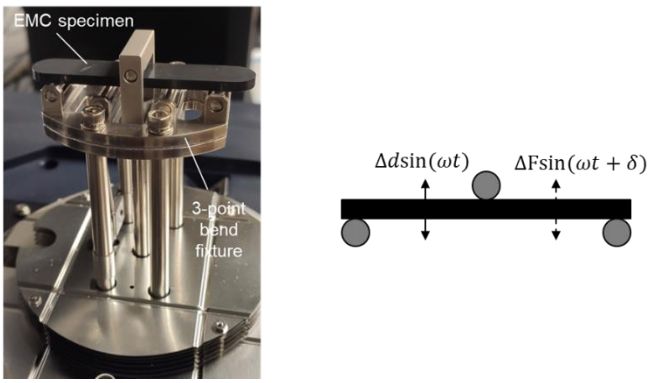


Figure 47 A photo of EMC specimen mounted on the three-point bend fixture (TA DMA850) for viscoelastic testing

Commercially available DMA machines provide versatile operational capabilities. With advanced user interfaces (UI) and highly sensitive load cells/ displacement sensors, the measurements can be completely automated. Yet, some cautions must be exercised for highly filled polymers as they can undergo a significant change in modulus over large temperatures (1-2 orders of magnitude). More details on how to conduct measurements accurately for such polymers are discussed in Ref. [115].

A multifrequency sweeping test (MFT) was conducted on an EMC specimen of dimension 50 mm x 10 mm x 3 mm. A three-point bending fixture was used for the experiment. The specimen mounted on the fixture is shown in Figure 47. The testing was conducted between 20°C – 240 °C (10 °C/step) and a frequency range of 0.1- 25 Hz (5 points/decade). The raw storage modulus data obtained from MFT sweeping is shown in Figure 48. The data appears to be continuous and shows good overlap. A storage modulus master curve was generated by TTS shifting.

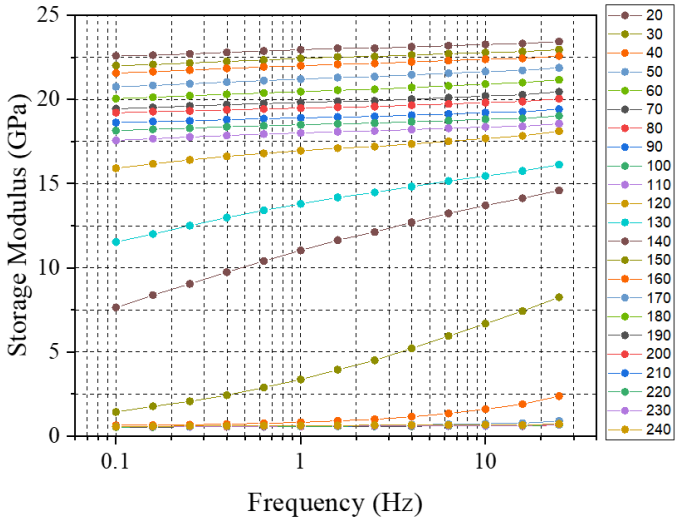


Figure 48 Raw MFT sweeping data of storage modulus ($E'(\omega)$) – 20°C to 240°C (10°C/step) and 0.1-25 Hz (5 points/decade)

The frequency domain master curve along with the corresponding shift factors are shown in Figure 49 (a) and (b), respectively. The reference temperature for shifting was $T_{ref} = 130$ °C.

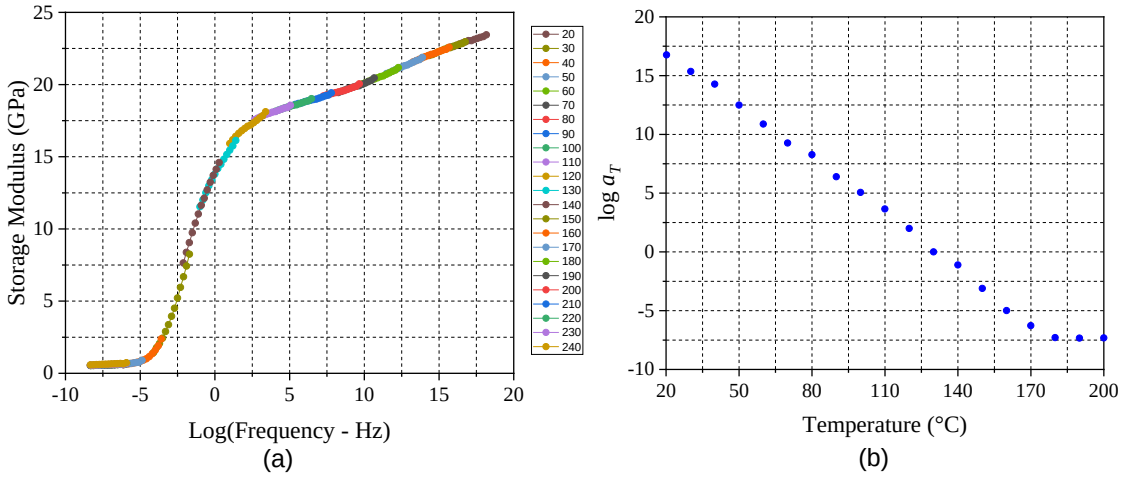


Figure 49 Results of TTS shifting from EMC DMA testing – (a) Storage modulus master curve and (b) shift-factors (log a_T) vs. temperature (°C)

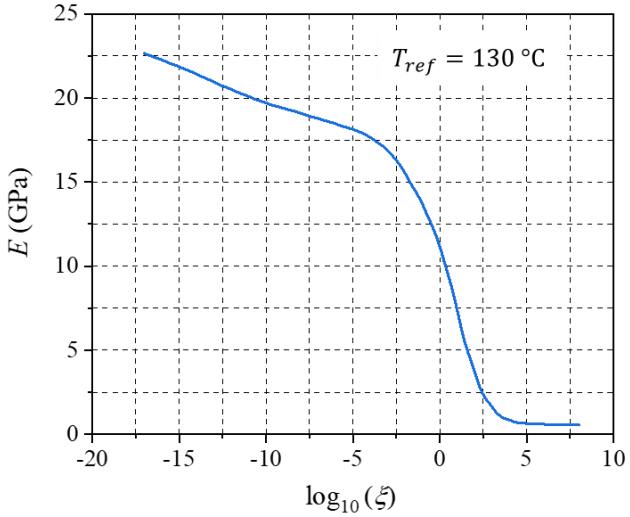


Figure 50 Time-domain Young's relaxation modulus master curve ($T_{ref} = 130°C$)

The storage modulus master curve was fitted to the Prony series equation using a non-linear fitting program in MATLAB. The frequency domain Prony series equation is:

$$E'(\omega) = E_\infty + \sum_{i=1}^{N} E_i \frac{\omega^2 \tau_i^2}{1 + \omega^2 \tau_i^2} \tag{79}$$

where E_i are the elastic constants and τ_i are the relaxation time constants of the Prony equation. The constants E_i and τ_i were determined from the fitting. The plot of time-domain master curve is shown in Figure 50 where ξ is the reduced-time axis on the log-scale.

5.3.4.2. Compressibility calculations

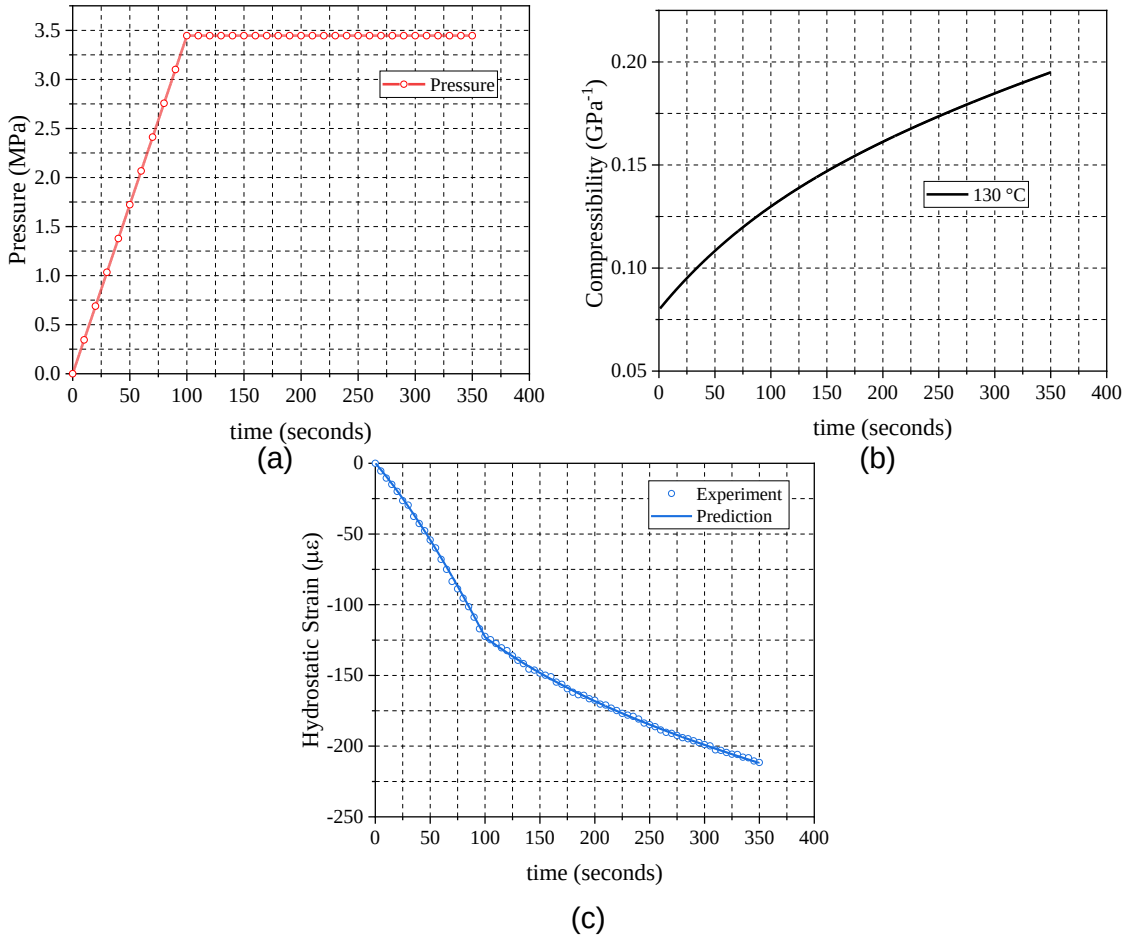


Figure 51 Illustration of the optimization program using data at 130°C – (a) Pressure profile data, (b) Calculated compressibility values and (c) comparison of prediction vs the experimental hydrostatic strain data with the obtained constants.

As mentioned previously, the entire temperature testing data set was used to determine compressibility using the optimization program. The results of the optimization program are demonstrated in Figure 51 using the data obtained at 130°C. The pressure profile used for load application is shown in Figure 51 (a), and the corresponding $B(t)$ values obtained from the fitting program are shown in (b). The strain values $\varepsilon_{h,pred}(t)$ were calculated using the obtained $B(t)$ values, and they were compared with the $\varepsilon_{h,exp}(t)$ documented during the experiment in (c).

Similar comparisons of the raw strain data with the prediction using the optimization program have been shown at various temperature of testing in Figure 52. Excellent correlations (overall $R^2 = 0.991$) corroborate the effectiveness of the optimization program.

In the next step, the compressibility values are converted to the bulk modulus using the following convolution integral:

$$\int_0^t B(t-\tau)K(\tau)d\tau = t \tag{80}$$

The above integral was solved numerically to determine $K(t)$ values from $B(t)$ at a given temperature. The $K(t)$ and $B(t)$ values were plotted on the log-time scale using the shift-factors to get both master curves. The master curves of $B(t)$ and $K(t)$ are shown in Figure 53 (a) and (b), respectively.

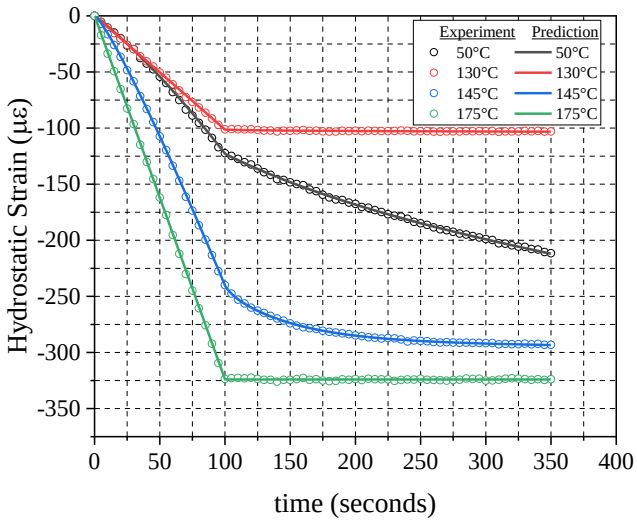


Figure 52 Comparison of the strain data obtained from experiment with the prediction of strain using the compressibility Prony series obtained from the optimization program

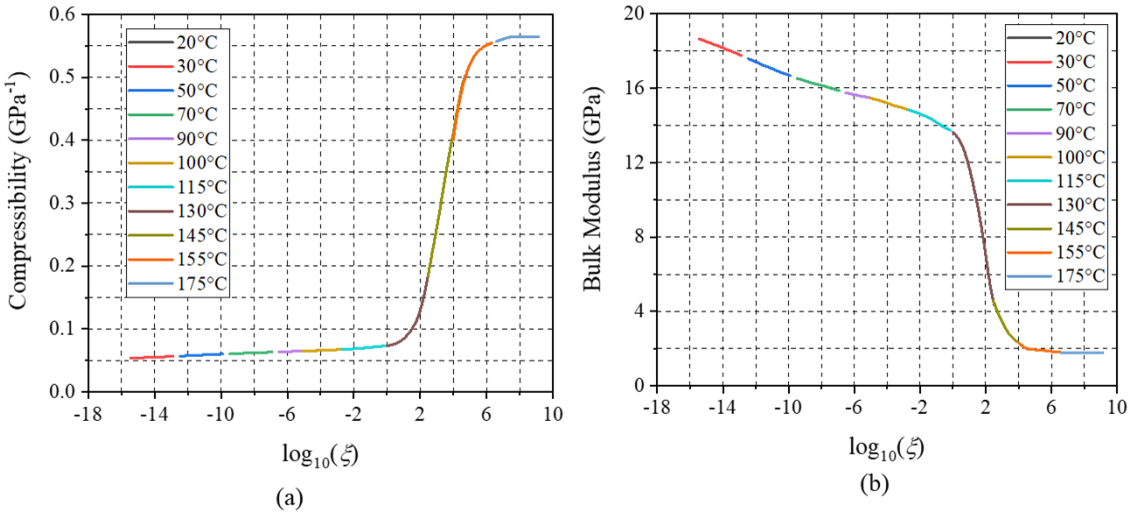


Figure 53 Bulk behavior master curves obtained from the experimental data – (a) compressibility, and (b) bulk modulus ($T_{ref} = 130°C$)

5.4. Discussions

5.4.1. Repeatability of measurements

Additional supplementary testing was conducted and a new compressibility master curve generated to determine repeatability of the measurements. The comparison of master curves obtained from Test 1 vs. Test 2 is shown in Figure 54. Both master curves look reasonably similar which shows the robustness of the developed test setup.

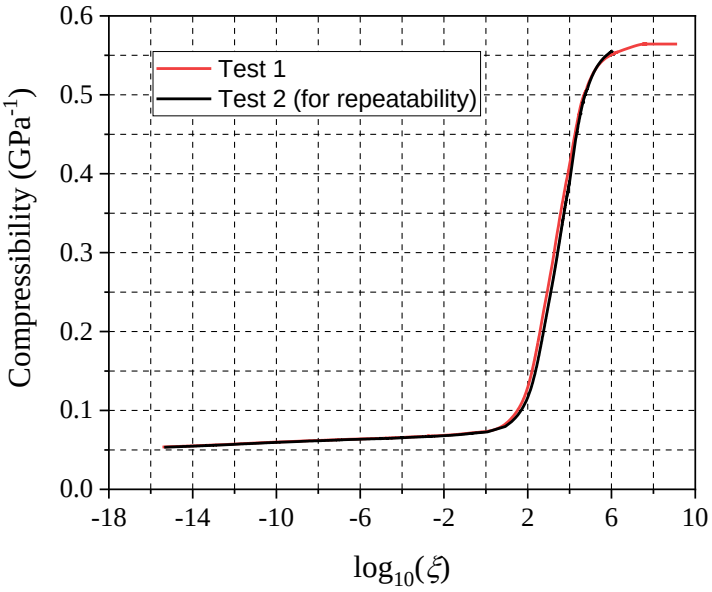


Figure 54 Comparison of compressibility obtained from Test 1 vs Test 2

5.4.2. Iteration issue

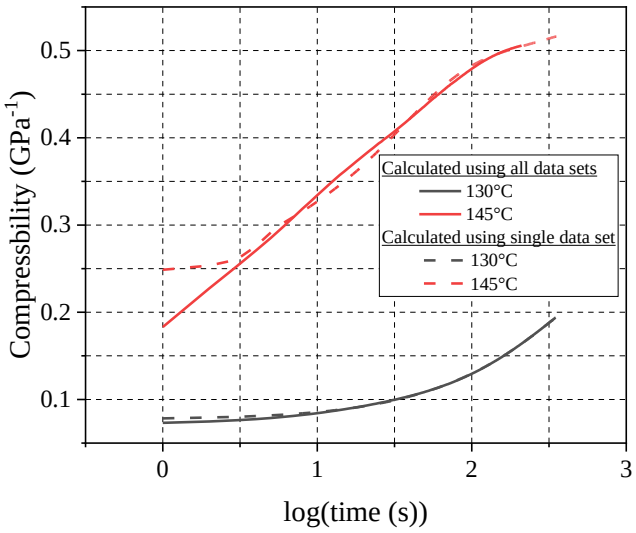


Figure 55 Comparison of compressibility evaluated for 2 temperatures (130 and 145°C) using single data sets versus the entire data set.

As discussed previously, one needs to be careful while interpreting the uniqueness of a system of linear equations. The difference between a solution obtained from global minimum vs. local minimum has been demonstrated by calculating compressibilities for two temperatures 130°C and 145°C using only single data sets and Eq. (75) and (76). The compressibilities have been compared with the solution obtained by fitting all the data sets together. The results of the two methodologies are shown in Figure 55. Both methodologies yielded a high R^2- 0.981 using single data sets and $R^2 - 0.992$ using all data sets.

It is clearly evident that the compressibilities obtained from single data sets deviate from the real compressibility values especially in the initial decades. The compressibility values obtained from single data sets show an apparent "flat" behavior in the initial decades as the

optimization program does not have the information for time-scales below 1 seconds and does not account for any viscoelastic behavior prior to the test time.

Due to this apparent behavior, the overlap also does not look continuous and shape of compressibility at final decade of 130°C and initial decade of 145°C looks very different. This is however not a problem when using the entire data set as the solution optimizes for all the time-scales involved between glassy and equilibrium region.

Chapter 6 Interconversion of Viscoelastic Properties

6.1. Introduction

Commercial numerical tools offer advanced but user-friendly analysis modules, and thus even engineers and scientists who do not have extensive experience of numerical analyses are able to simulate almost any kind of electronic packaging products. Yet, the prediction accuracy is still dependent on the accuracy of the constitutive properties of materials used in the model.

One of the most critical properties is the temperature-dependent viscoelastic properties of polymers, abundantly used in the advanced packages. Some simplifications and approximations (e.g., a constant bulk modulus, a constant Poisson's ratio, etc.) have been used due to the complexity involved in measuring the required properties. To compensate the simplifications, commercially available warpage measurement tools such as shadow moiré, projection moiré, digital image correlation (DIC), etc., have been employed, through which the simplified material properties are adjusted until numerical predictions have reasonably good agreement with displacement measurements.

In fact, it is not too difficult to find numerous papers in the open literature where authors claimed that predictions agreed very well with measurements in spite of missing properties [9, 10, 116-119]. Unfortunately, the "adjusted" models often do not produce accurate predictions when different package architectures using the same polymer materials are to be analyzed. This will be referred to as "architecture-dependent" model, which is defined as "a model that works for a specific packaging design but does not work for different designs using the same material sets". If accurate material properties are employed, however, the prediction accuracy should remain the

same regardless of the package architectures. This model will be referred to as "authentic material-based model".

It is rather obvious from the viscoelastic constitutive equations implemented in the commercial numerical tools, the master curves of shear and bulk moduli and the shift factors are required. Young's modulus master curve and the shift factors are $E(t,T)$, are routinely measured using a dynamic mechanical analyzer (DMA), but not the other properties. This is the issue we address in this chapter.

This chapter first reviews some basic viscoelastic fundamentals and discusses the common simplications/assumptions made in current practice of linear viscoelasticity (LVE) for FEM modeling. The calculation of $G(t,T)$ and $K(t,T)$ from the viscoelastic Young's modulus, $E(t,T)$, obtained from DMA testing, under the assumptions together with the critical implications of the assumptions is discussed. Using the property measurements from Chapter 4, specifically, (1) measurement of $E(t,T)$ using DMA, (2) determination of $K(t,T)$ from measured hydrostatic testing data, shear relaxation modulus - $G(t,T)$ has been calculated.

6.2. Background and Assumption made in current practice

The constitutive laws of linear viscoelasticity are written as [113, 120] :

$$s_{ij}(t) = 2\int_0^t G(t-\tau)\frac{\partial e_{ij}(\tau)}{\partial \tau}d\tau$$
$$\sigma_{kk}(t) = 3\int_0^t K(t-\tau)\frac{\partial \varepsilon_{kk}(\tau)}{\partial \tau}d\tau \quad (81)$$

where s_{ij}, σ_{kk}, e_{ij} and ε_{kk} are deviatoric stress, volumetric stress, deviatoric strain and volumetric strain tensors respectively. $G(t)$ and $K(t)$ are the time-dependent shear modulus and bulk modulus, respectively.

The correspondence principle represents the time-domain viscoelastic equations in Laplace domain. Due to the nature of the equations, the Laplace domain equations of linear viscoelasticity resemble elastic equations which can simplify the solutions to the problems. The two constants, E and ν have the following relationship with the other two constants G and K in Laplace domain as follows [42]:

$$\bar{G}(s) = \frac{\bar{E}(s)}{2[1 + s\bar{\nu}(s)]}; \bar{K}(s) = \frac{\bar{E}(s)}{3[1 - 2s\bar{\nu}(s)]} \tag{82}$$

In the above equation, the viscoelastic constants - $E(t), \nu(t)$, $G(t)$ and $K(t)$ have their corresponding representations in Laplace domain as - $\bar{E}(s), \bar{\nu}(s), \bar{G}(s)$ and $\bar{K}(s)$, respectively.

Conversions from the time-domain to Laplace domain is usually simple. However, converting back from the Laplace domain to the time domain requires complex integral functions and involves computationally heavy numerical solutions. Thus, for practical purposes, most viscoelastic problems are solved in time-domain directly using commercial FEM tools.

6.2.1. Assumptions and simplications used in the current practice of viscoelastic modeling

Measurement of temperature dependent viscoelastic Young's modulus - $E(t, T)$ is routinely conducted using commercially available machines like dynamic mechanical analyzer (DMA) or universal tensile testing machine (UTTM). However, other temperature-dependent viscoelastic properties are much more difficult to measure.

Some assumptions are needed to be able to conduct a viscoelastic analysis with only viscoelastic Young's modulus, as commercial FEM solvers requires the master curves of shear and bulk moduli and the shift factors.

6.2.1.1. Use of $E(t)$ Prony series for $G(t)$ and constant bulk modulus - K_0

One of the most widely used assumptions in the community is that the Prony terms for the shear modulus master curve - $G(t)$ follow the Prony terms for the Young's modulus - $E(t)$ [10, 116-118, 121, 122]. Under this assumption, using the glassy Poisson's ratio (typically measured at room temperature) - ν_0, the master curve for $G(t)$ is calculated as follows:

$$G(t) = \frac{E(t)}{2(1+\nu_0)} \tag{83}$$

This assumption originates from Knauss's review paper – Ref. [42] which states that both $E(t)$ and $G(t)$ undergo glass transition over similar time-scales while $K(t)$ transition is shorter than $E(t)$ or $G(t)$. The bulk modulus is assumed to be constant - K_0 which is calculated from the Poisson's ratio - ν_0 and glassy Young's modulus - E_0 as follows:

$$K_0 = \frac{E_0}{3(1-2\nu_0)} \tag{84}$$

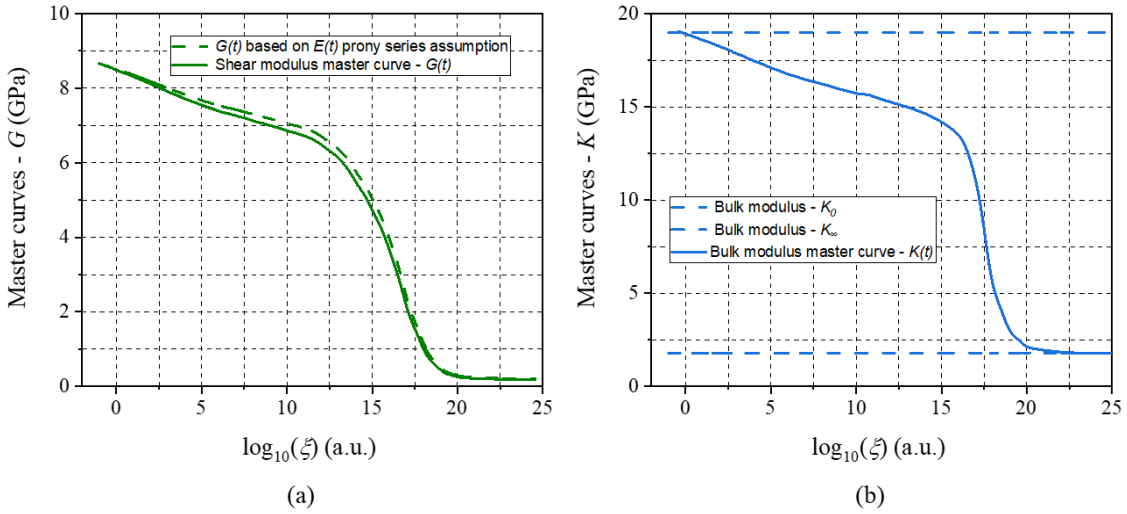


Figure 56 Comparison of real $G(t)$ and $K(t)$ master curves with the master curves obtained using the assumptions.

Using the real $G(t)$ and $K(t)$ obtained from the experimental data, a comparison between the $G(t)$ obtained from Eq. (83) and K_0 obtained from Eq. (84) are made. The comparison is shown in Figure 56. The (a) shows comparison between $G(t)$ calculated using the assumption and real $G(t)$. They seem to agree reasonably well confirming that the assumption made here by Knauss was reasonable.

However, in (b) it can be clearly seen that $K(t)$ changes significantly over the glass transition region and the assumption of K_0 does not work well. Assuming a constant K_0, also causes another issue, the Poisson's ratio of the model approaches 0.5 after the glass transition, which makes the apparent material behavior nearly incompressible.

This has been illustrated in Figure 57 by calculating $\nu(t)$ from the $G(t)$and K_0 obtained from the assumption.

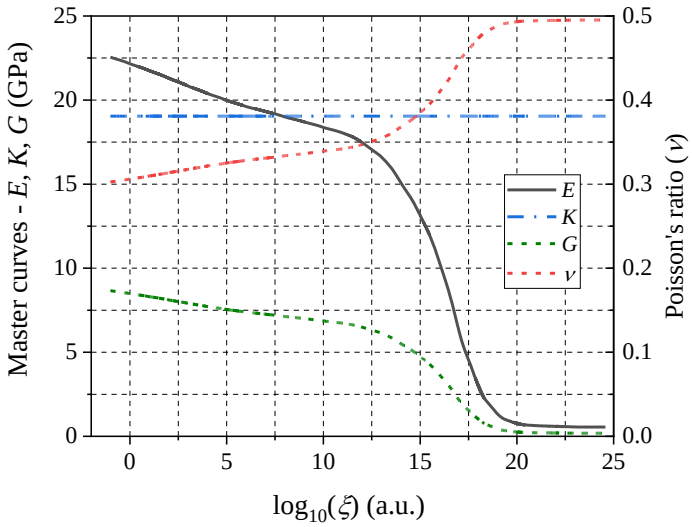


Figure 57 Calculation of time-dependent Poisson's ratio using $G(t)$ and K_0

6.2.1.2. Determination of $G(t)$ and $K(t)$ master curves assuming constant Poisson's ratio - ν_0

Another common practice (less widely used) in the community is "constant" Poisson's ratio (i.e., time-temperature "independent" Poisson's ratio) [119, 123]. Under the assumption, $G(t)$ and $K(t)$ required for FEM modeling, can be determined from $E(t)$ simply by:

$$\mathcal{L}^{-1}\left[\bar{G}(s) = \frac{\bar{E}(s)}{2\left(1 + s \cdot \frac{\nu_0}{s}\right)}\right] = G(t) = \frac{E(t)}{2(1+\nu_0)}$$
$$\mathcal{L}^{-1}\left[\bar{K}(s) = \frac{\bar{E}(s)}{3\left(1 - 2s \cdot \frac{\nu_0}{s}\right)}\right] = K(t) = \frac{E(t)}{3(1-2\nu_0)} \quad (85)$$

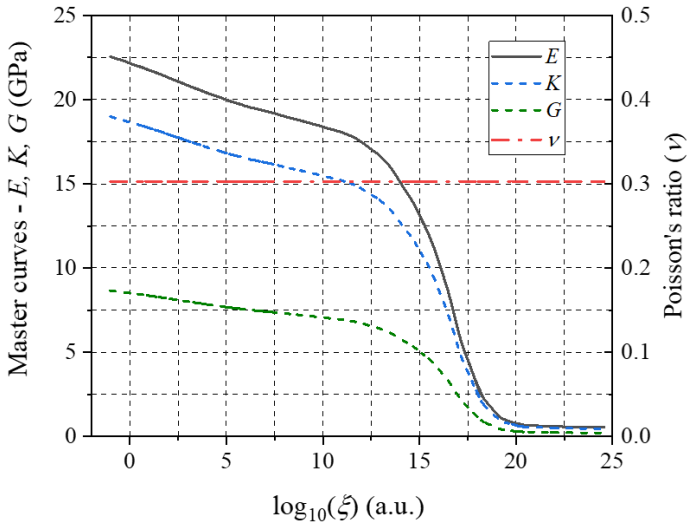


Figure 58 $G(t)$ and $K(t)$ master curves calculated based on the Poisson's ratio $\nu_0 = 0.3$ using Eq. (85)

The master curves of $G(t)$ and $K(t)$ calculated using Eq. (85) are illustrated in Figure 58, where $E(t)$ is determined by DMA and ν_0 is assumed to be 0.3. It is important to note that the calculated $G(t)$ and $K(t)$ are proportionally scaled with $E(t)$ simply because of the constant value of ν_0. This large relaxation in $K(t)$ is unrealistic, and, consequently, the volumetric deformations can be overestimated significantly when the temperatures cross T_g region.

6.3. Interconversion of Viscoelastic Properties from Governing Equations

As discussed previously, for FEM modeling two sets of master curves i.e. shear relaxation modulus - $G(t)$ and bulk relaxation modulus - $K(t)$ are required. In Chapter 4, the $E(t)$ and $K(t)$ were measured. A set of hereditary and convolution integrals is required to convert the viscoelastic functions to obtain the $G(t)$. Viscoelastic Poisson's ratio master curve has also been calculated to

determine how the Poisson's ratio evolves in EMC over the entire transition region. The equations for interconversion had been discussed and the master curves calculated.

6.3.1. Calculation of shear relaxation modulus - $G(t)$ from $E(t)$ and $K(t)$

Using the – Young's relaxation modulus $(E(t))$ and, bulk relaxation modulus $((K(t))$, the shear relaxation modulus $(G(t))$ can be calculated. The equations in Laplace domain are as follows:

$$\bar{G}(s) = \frac{3\,\bar{K}(s)\bar{E}(s)}{9\bar{K}(s) - \bar{E}(s)} \tag{86}$$

where $\bar{E}(s)$, $\bar{G}(s)$ and $\bar{K}(s)$ are Laplace transforms of $E(t), G(t)$ and $K(t)$ respectively.

By simplifying the equations and taking an inverse Laplace transform, it gives the following equations to obtain shear modulus in time-domain:

$$\begin{gathered} J(t) = 3D(t) - \frac{1}{3}B(t) \\ \int_0^t G(t-\tau)J(\tau) = t \\ \int_0^t E(t-\tau)D(\tau) = t \\ \int_0^t K(t-\tau)B(\tau) = t \end{gathered} \tag{87}$$

where $B(t), D(t)$ and $J(t)$ are the creep compliances for the viscoelastic functions - $K(t), E(t)$ and $G(t)$ respectively.

To determine the shear modulus master curve, the uniaxial creep compliance $D(t)$ needs to be first evaluated from $E(t)$ by solving the convolution integral. $B(t)$ calculated from the

hydrostatic data and $D(t)$, the time-dependent shear creep compliance is calculated - $J(t)$. Finally, the shear creep compliance is converted to $G(t)$ using the convolution integral.

6.3.2. Calculation of viscoelastic Poisson's ratio - $\nu(t)$ from $E(t)$ and $K(t)$

The Poisson's ratio in Laplace domain ($\bar{\nu}(s)$) can be expressed in terms of $\bar{E}(s)$ and $\bar{K}(s)$ as follows:

$$\bar{\nu}(s) = \frac{1}{2s} - \frac{\bar{E}(s)}{6s\bar{K}(s)}$$
$$\bar{\nu}(s) = \frac{1}{2s} - \frac{s\bar{E}(s)\bar{B}(s)}{6} \quad (88)$$

The time-domain viscoelastic Poisson's ratio - $\nu(t)$ can be obtained by taking the inverse Laplace transform of above equation to get the following equation:

$$\nu(t) = \frac{1}{2} - \int_0^t E(\tau)\frac{\partial B(t-\tau)}{\partial \tau}d\tau \quad (89)$$

The hereditary integral, can be solved numerically using the measured $E(t)$ and $B(t)$ to get the viscoelastic Poisson's ratio master curve.

Using Eq. (87)and (89), the master curves for $G(t)$ and $K(t)$ were calculated. The master curves for $E(t)$, $K(t)$, and $G(t)$ are shown in Figure 59 together with the Poisson's ratio - $\nu(t)$. The two sets of "authentic material based" properties will be used as inputs for the FEM model.

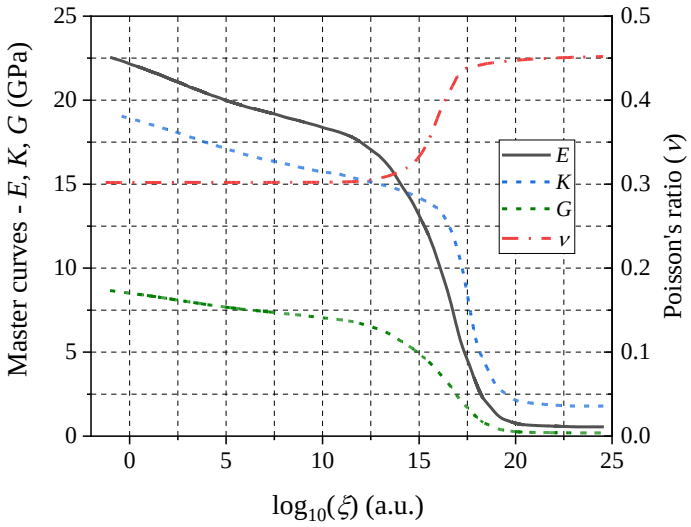


Figure 59. Master curves for EMC - E, G, K and ν

Chapter 7 Characterization of Cure-extent Dependent Viscoelastic Behavior

7.1. Theoretical Background: Cure-dependent Viscoelasticity

For a fully-cured polymer, the relaxation modulus (represented here by shear modulus - $G(t,T)$) can be expressed using Prony series as follows:

$$G(t,T) = G_\infty + \sum_{i=1}^{N} G_i \exp\left(-\frac{t}{a_T(T)\tau_i}\right)$$
$$\frac{G(t,T) - G_\infty}{G_G - G_\infty} = \sum_{i=1}^{N} g_i \exp\left(-\frac{t}{a_T(T)\tau_i}\right) \quad (90)$$

where G_∞ and G_G are equilibrium modulus and glassy modulus, respectively; g_i are the normalized Maxwell constants and τ_i are the relaxation time constants of a polymer.

For a partially-cured polymer, the relaxation modulus is cure-extent dependent. For a partially-cured polymer with cure-extent (p), the viscoelastic function can be written as [74]:

$$G(t,p) = G_\infty(p) + \sum_{i=1}^{N} G_i(p) \exp\left(-\frac{t}{\tau_i(p)}\right)$$
$$\frac{G(t,p) - G_\infty(p)}{G_G - G_\infty(p)} = \sum_{i=1}^{N} g_i(p) \exp\left(-\frac{t}{\tau_i(p)}\right) \quad (91)$$

where $G_\infty(p)$ is cure-extent dependent equilibrium modulus; $g_i(p)$ and $\tau_i(p)$ are cure-extent dependent normalized Maxwell constants and relaxation time constant, respectively. Further simplification to Eq. (91) can be made based on theoretical framework developed by Adolf et. al., in Ref. [71].

A schematic illustration of the relaxation modulus at various cure extents is shown in Figure 60. The figure shows representative relaxation moduli at three cure extents -$p_1 > p_2 > p_3$. The polymer relaxes slower for higher-cure extents, while the equilibrium modulus -$G_\infty(p)$ increases as it cures. It has been known that the magnitude of glassy modulus - G_G is independent of cure-extent [70, 124].

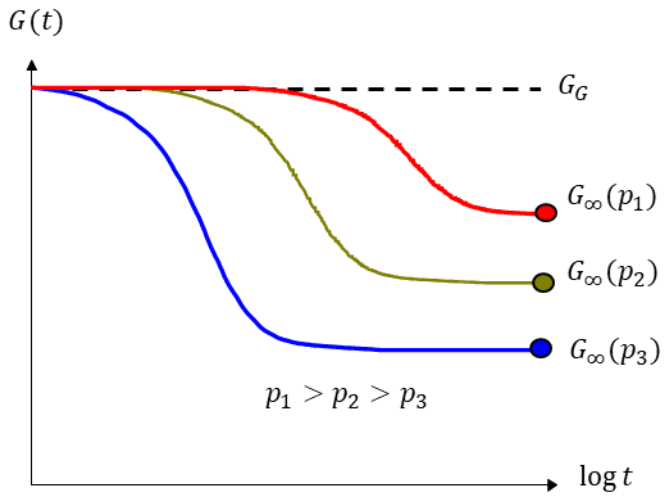


Figure 60 A schematic illustration relaxation modulus at various cure-extents

7.1.1. Cure-rheological simplicity (CRS)

During the curing process, the polymers being cured undergo crosslinking process through chemical reactions. This has been illustrated in Figure 61 which shows a schematic of how the polymer clusters grow in size during the curing process. The polymer clusters in the near-critical gel region are geometrically self-similar, a change in the extent of cure results in a mere change in scale; clusters become larger as p increases [71].

This increase in cluster sizes has two consequences – (1) increase in equilibrium modulus ($G_\infty(p)$) and (2) increase in relaxation time. This provides a technical rationale for an assumption that no change in relaxation mechanism occurs with cure-extent, i.e., cure-extent only affects the rate of the behavior – Cure-rheological simplicity (CRS). The implication of this assumption is that the cure-extent dependent normalized Maxwell constants - $e_i(p)$ shown in Eq. (91) can be assumed to be constant i.e., independent of cure extent – $e_i(p) \approx e_i$.

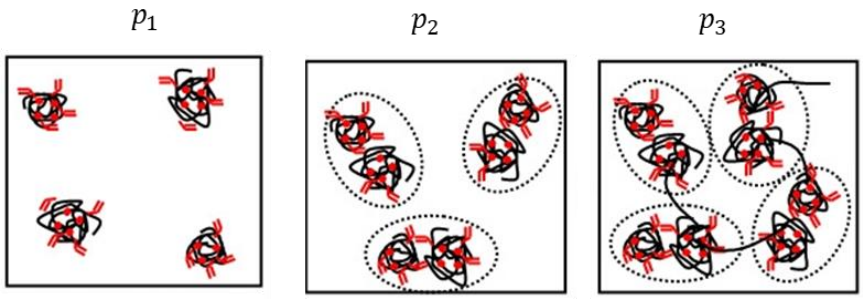


Figure 61 A schematic illustrating crosslinking process in a polymer during curing ($p_1 < p_2 < p_3$) [125]

The equation simplifies to the following based on the CRS assumption:

$$G(t,p) = G_\infty(p) + (G_G - G_\infty(p)) \sum_{i=1}^{N} g_i \exp\left(-\frac{t}{\tau_i(p)}\right) \tag{92}$$

The relaxation moduli can be normalized using G_G and $G_\infty(p)$. The normalized master curves have similar shapes but are shifted on the $\log(t)$ scale due to different relaxation times.

7.1.1.1. Time-cure superposition (TCS)

A second implication of the CRS assumption gives us time-cure superposition (TCS). TCS states that the viscoelastic functions at different cure extents should super impose provided appropriate horizontal shifts ($\log a_p(p)$) on the $\log(t)$ scale. This is illustrated in Figure 62 (c).

Similar to the shift-factors in TTS, the horizontal shift change, (caused by the increase in cluster sizes), can be expressed by redefining a relaxation time (larger clusters relax more slowly). Eq. (92) can be simplified further based on the shift-factors to the following equation [74]:

$$G(t,p) = G_\infty(p) + (G_G - G_\infty(p)) \sum_{i=1}^{N} g_i \exp\left(-\frac{t}{a_p(p)\tau_i}\right) \tag{93}$$

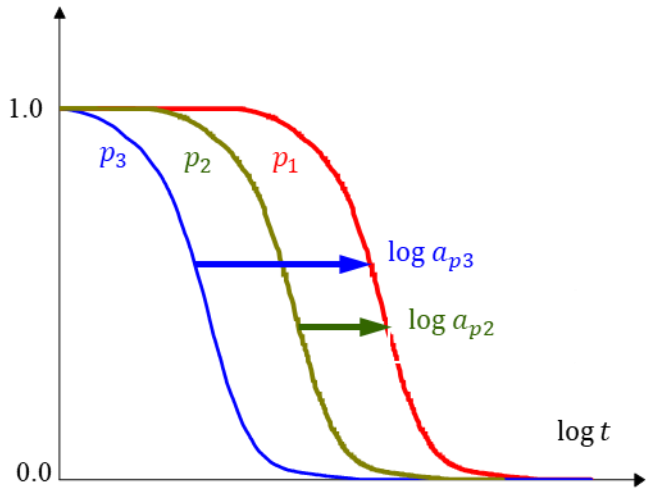


Figure 62 Horizontal shifting of the normalized master curves (shape functions) on the $\log(t)$ scale using time-cure superposition (TCS)

7.1.1.2. Evolution of equilibrium moduli during curing

The equilibrium moduli as a function of cure extent must be known. Attempts to explain the gel formation and evolution of equilibrium modulus have been made using the Mean Field Theory [64] and the percolation theory [65].

Percolation theory is a simple way to predict the strength of polymers as a function of cross-link density. The theory has been well established in the polymer community and was originally applied in Ref. [70] in an attempt to describe evolution of equilibrium shear modulus -

$G_\infty(p)$ for a two-part epoxy (DGEBA/DEA) system. The shear equilibrium modulus evolution of a two-part system using percolation theory can be expressed as [70]:

$$G_\infty(p) = G_\infty^f \left(\frac{p^2 - p_{gel}^2}{1 - p_{gel}^2}\right)^{n_G} \tag{94}$$

where G_∞^f is the equilibrium shear modulus of fully-cured polymer, p_{gel} is the gel point of the polymer and n_G is the evolution component. The evolution component was determined to be $n = 8/3$ for the two-part epoxy (DGEBA/DEA) system. The evolution component needs to be determined experimentally for the EMC being tested.

7.2. Background and Motivation

There have been attempts to measure cure-dependent viscoelastic properties of polymers (EMC and unfilled thermosets). This section describes shortcomings and insufficient accuracies in the reported data.

7.2.1. Cure-dependent viscoelastic measurements of EMC

There have been attempts to measure cure-dependent viscoelastic properties of EMC in Ref. [14, 49, 57, 75, 110]. Although different EMCs were used across the papers, the measurement methodology was common. The papers attempted to measure two sets of properties – shear modulus and bulk modulus to determine viscoelastic behavior of EMC as a function of cure extent.

For bulk modulus measurements, a high-pressure dilatometer/ P-V-T (pressure-volume-temperature) machine described in section 5.1.1 was used. It was assumed that the bulk modulus does not change with cure-extent and the measurements were only conducted on a fully-cured specimen. This is fundamentally incorrect, as it is well known that when the material crosses the

gel-point, it transitions from a liquid state to a solid state. The bulk modulus transitions from incompressible ($K \to \infty$) state to a compressible material (K finite) gradually as the material cures.

A P-V-T setup similar to the schematic diagram shown in Figure 35 was used for measurement. An EMC coupon was inserted in the chamber and a pressure level from 10 MPa – 100 MPa was applied at various temperatures to determine volume change as a function of temperature and pressure. The results of the compressibility tests are shown in Figure 63.

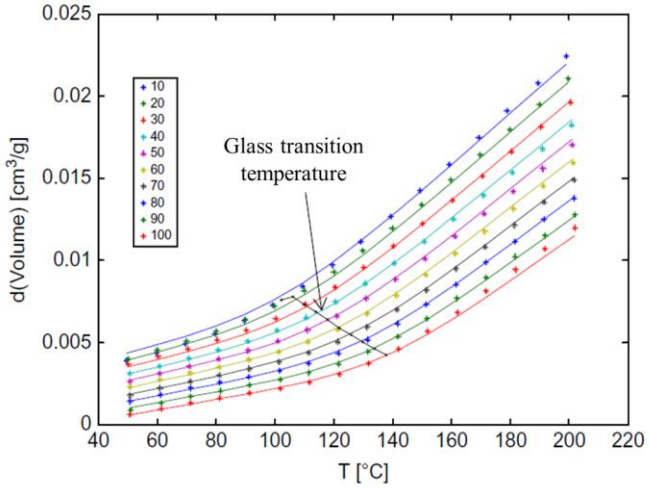


Figure 63 Volume change of fully-cured EMC in different temperature and pressure for P-V-T measurement [14]

Using the Tait's equation shown in Eq. (56), the temperature-dependent compressibility $-B(T)$ and bulk modulus - $K(T)$ were calculated. As described before, the equations of state have been obtained independent of time and do not consider time-dependent behavior. Hence, bulk modulus determined was both cure and time-independent.

For the second viscoelastic property measurement, a custom shear test setup was used to measure cure-dependent viscoelastic shear behavior of EMC. A schematic for the setup is shown in Figure 64. Two identical shear test specimens (partially-cured) are mounted on the fixture and were subjected to multi-frequency temperature sweeping (MFT) tests.

The shear tool was originally developed in Ref. [126]. The tool was developed to provide reliable results for shear modulus measurements for materials with shear moduli lower than 200 MPa [126]. This is because, the tool uses a correction factor while determining the shear moduli from the experimental results. However, the results showed significant deviations (over 10%) for shear moduli of magnitude 200 MPa or more based on the analysis conducted in the paper. It is clear from the experimental results that the shear moduli of (fully-cured) EMC tested changes from about 2520 MPa (glassy) to 40 MPa (rubbery) over the duration of tests which implies measurement uncertainties specifically in the glassy region.

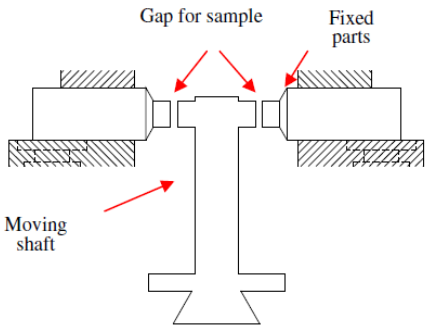


Figure 64 Schematic of the shear clamps used for EMC testing [14]

Several temperature ramps were conducted exceeding $T_g(p)$ of the partially cured material (shown in Figure 65). This was done to determine T_g^{DMA} and obtain the equilibrium modulus - $G_\infty(p)$ of the polymer at various cure extents

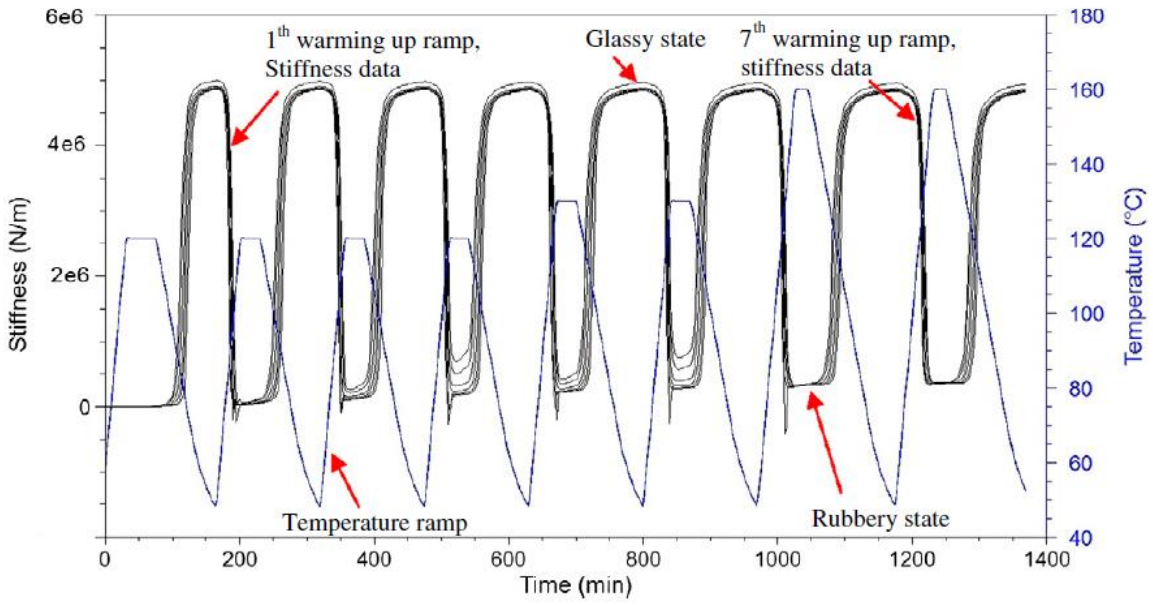


Figure 65 Temperature profile and measured stiffness values during various ramping testing for different degrees of cure.

Considering the range of frequencies applied – 0.32 Hz to 60 Hz, it must at least several minutes to run a frequency sweep at a particular temperature. In addition, the temperatures during each ramp exceeded $T_g(p)$. Extra curing during testing should not be ignored. Yet, the curing during the testing where the material exceeds $T_g(p)$ was not mentioned or discussed.

The storage modulus master curves obtained from testing are shown in Figure 66. Here, the last point in each master curve was used as the equilibrium modulus -$G_\infty(p)$. The isocure state was not maintained as the test temperatures exceeded $T_g(p)$. Both relaxation and curing rates are significant above T_g. The $G_\infty(p)$ determined for that specific cure extent seems incorrect.

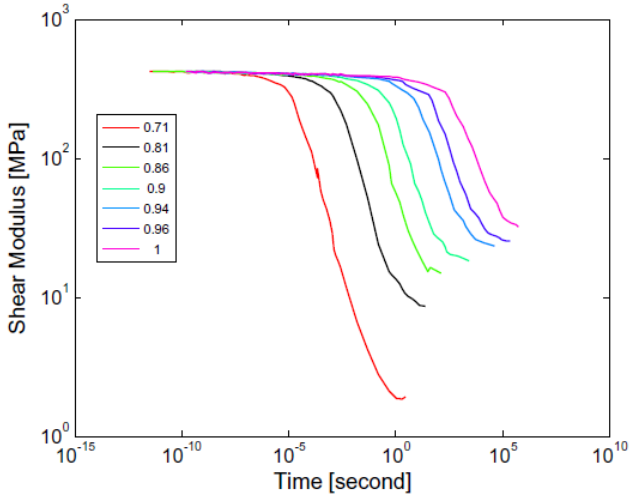


Figure 66 Storage modulus master curves at various cure extents

The extra curing during testing is even more evident in normalized overlapped master curves shown in Figure 67. There is an initial good overlap in the glassy region indicating that the data was measured consistently in isocure state. It is evident that the overlap does not look good in the T_g region which have been attributed to the extra curing during testing. Additionally, rubbery plateau is not clearly visible at the end of master curve. In fact, in some cases an increase in the modulus can be clearly seen (red and green lines).

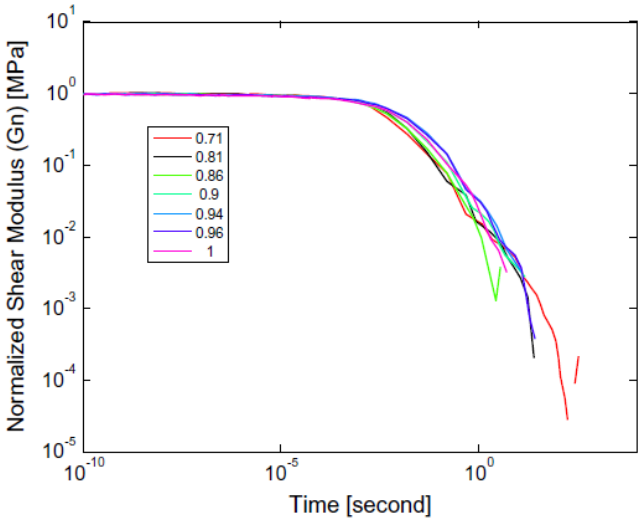


Figure 67 Normalized shear modulus master curves.

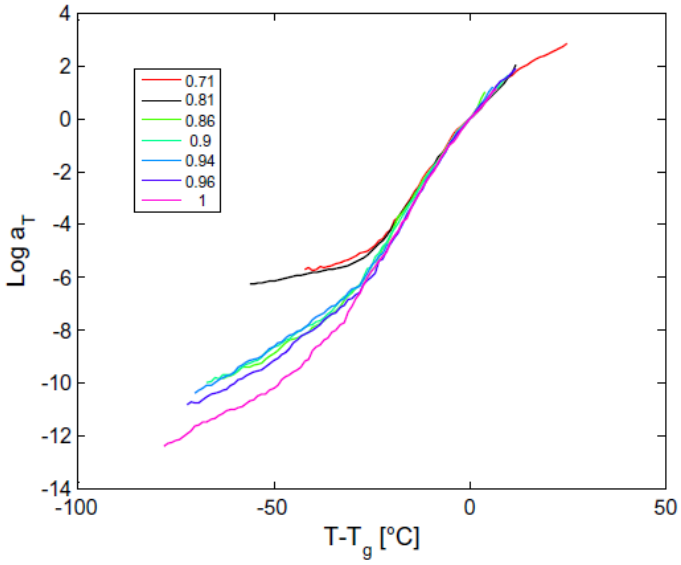


Figure 68 Shift-factor related to shear modulus master curves

The authors attempted to claim that the overlap of cure-dependent master curves is evident when the master curves are constructed using $T_{ref} = T_g(p)$ as the reference temperature. The results of shifting are shown in Figure 68 with x-axis as $T_g - T$ and y-axis as $\log a_T$. It is again

evident that the overlap is excellent only in the glassy region. However, once the material temperature crosses T_g, there are significant deviations in the shift factors and no justification or reasoning was provided for these deviations while simply claiming that they "overlap". So, shifting criteria used does not have sufficient technical justification either theoretically or experimentally.

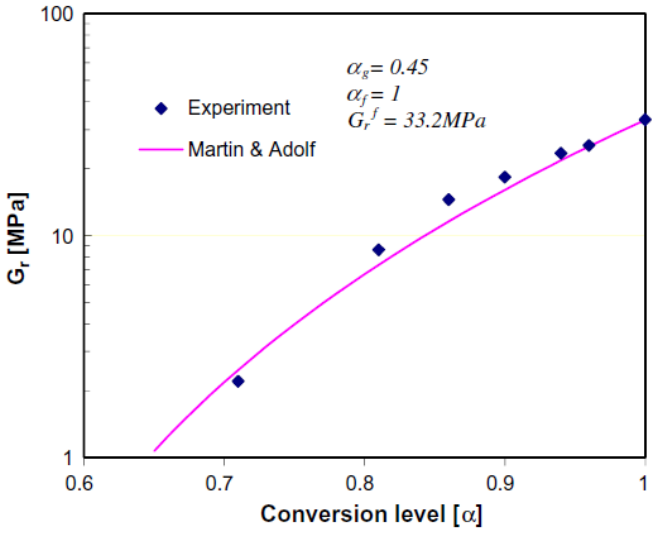


Figure 69 Cure-dependency of the shear rubbery plateau. Fittings are based on Martin and Adolf theory.

As mentioned previously, an attempt to determine equilibrium modulus was made based on the end point of the ramp shown in Figure 66 which had significant uncertainties due to the reasons provided above.

$$G_\infty(p) = G_\infty^f \left(\frac{p^2 - p_{gel}^2}{1 - p_{gel}^2} \right)^{8/3}$$

Martin and Adolf's percolation theory-based model was used for comparison with the obtain experimental data. Although the theory was technically sound, the exponent was obtained for a DGEBA/DEA based two-part epoxy system (soft unfilled thermoset polymer) - $n = 8/3$.

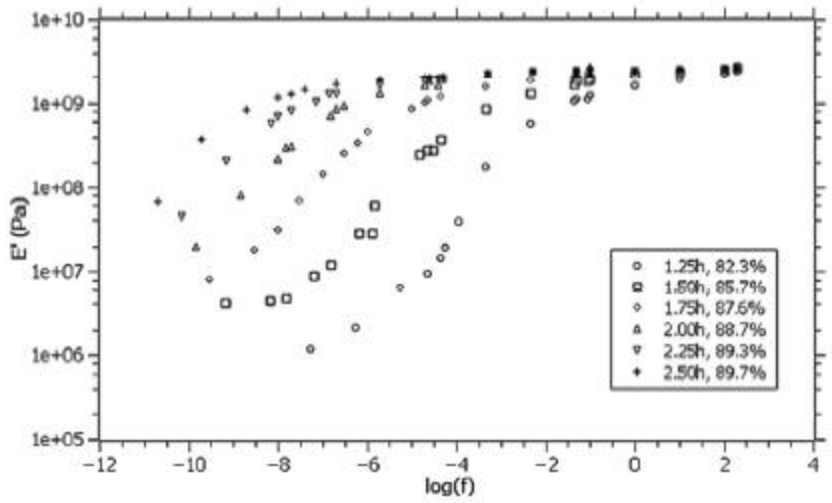
This exponent was assumed to be same for the filled thermoset (EMC) that was tested. Additionally, it was assumed that the p_{gel} is 0.5 with no experimental evidence or technical rationale provided for it. An evolution model based on incorrect parameters was constructed to compare with incorrect equilibrium modulus data to "apparently" show that both theory and experiment are matching well.

7.2.2. Cure-dependent viscoelastic measurements of unfilled thermosets

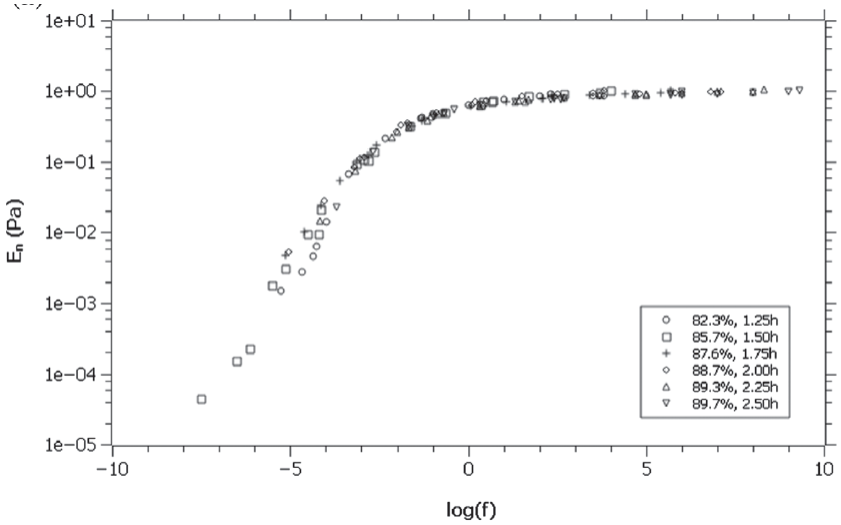
More recently, Saseendran et.al. [69, 76, 80] attempted to measure cure-extent dependent viscoelastic properties of an unfilled thermoset two-part epoxy system (LY5052/HY50552 epoxy resin). The authors chose an unfilled thermoset system like Adolf et. al. [70] (who developed the theory for cure-dependent viscoelastic shear behavior) and attempted to extend it for other property measurements - Young's modulus and Poisson's ratio. They used procedure similar to previous section to measure cure-extent dependent viscoelastic Young's modulus.

Partially-cured epoxy specimens were subjected to uniaxial testing using MFT sweeping to determine Young's modulus master curves of the epoxy at various cure extents. Here also the authors exceeded the $T_g(p)$ of the material during the sweeping test while determining the master curves. The paper utilized dual shift methodology, i.e., determination of both cure-extent dependent shift-factors ($a_p(p)$) and temperature-dependent shift-factors ($a_T(T)$) of partially cured EMC to generate one super master curve.

The results of the MFT sweeping after TTS shifting and TCS shifting are shown in Figure 70 (a) and (b), respectively. The master curves show reasonable overlap in the glassy region; however, the overlap is not as good as the material transitions into glass transition region, which may be attributed to extra curing and inaccuracies in calculation of equilibrium moduli.



(a)



(b)

Figure 70 (a) Master curves at various cure states referenced at a test temperature of 23°C, (b)super-master curve generated by normalizing and horizontally shifting the data in (a) [80]

The equilibrium modulus was determined using the lowest point in the master curve. The evolution model equation with evolution component of $n = 8/3$ was used for comparison with the

experimental data. It was assumed that evolution model remains same for Young's equilibrium moduli and the evolution equation can be expressed as follows:

$$E_\infty(p) = E_\infty^f \left(\frac{p^2 - p_{gel}^2}{1 - p_{gel}^2} \right)^{8/3} \tag{95}$$

A comparison of the fitting to the experimental data is shown in Figure 71. Large deviations between the model and the experimental data can be clearly seen. It is also worth noting that using another evolution model would also produce erroneous results as the equilibrium moduli measurements have large uncertainties due to curing and testing beyond T_g of the material.

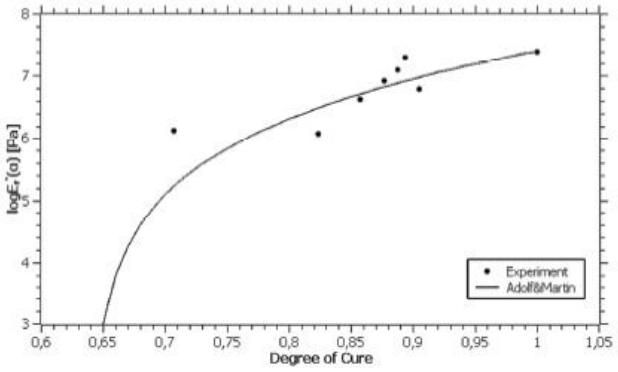


Figure 71 Experimental values of equilibrium modulus vs. Adolf and Martin model [69]

Saseendran et al. also attempted to measure cure-dependent viscoelastic Poisson's ratio of the epoxy system [76]. To the best of author's knowledge, this was the first attempt to measure a second cure-dependent viscoelastic property of the same polymer other than shear or Young's modulus. This paper also provided a theoretical justification for assuming both temperature-dependent and cure-dependent shift-factors to be a universal property, which can be applied to all viscoelastic functions (using constitutive equations).

A strain gauge was attached to the specimen to determine transverse strains. The issues associated with reinforcement effect have not been discussed. The Young's modulus of the partially-cured material is very small (~10 MPa), it is very difficult to negate the issue of reinforcement without using a very large specimen. A long term (24 hours $\sim 10^5$ seconds) relaxation test was conducted at room temperature by applying a constant longitudinal strain of 0.5% and the transverse strain was recorded as a function of time. The results of the tests are shown in Figure 72. Looking closely at the data shows issues, specifically the large differences in magnitude and trend of Poisson's ratio behavior with a cure extent difference of only ~1%. The data obtained at 100 second and 1000 second was plotted (shown in Figure 73 (a) and (b)) to conclude that Poisson's ratio does exhibit cure dependency. Additionally, even though the testing was conducted in the glassy region, the duration of the test is very long ~24 hrs. The expected amount of change in cure extent under diffusion control conditions has not been considered or discussed.

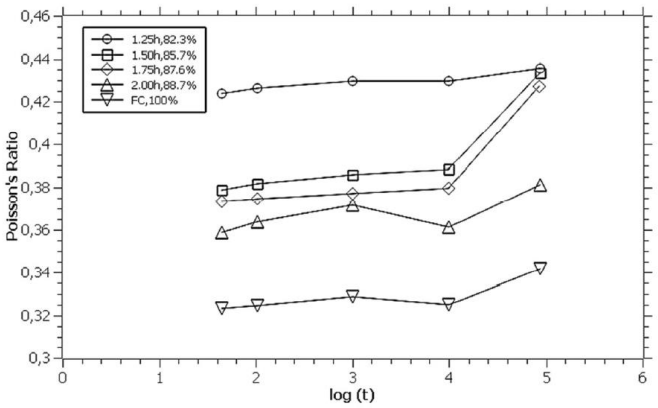


Figure 72 Poisson's ratio from stress relaxation testing of samples at various cure states [76].

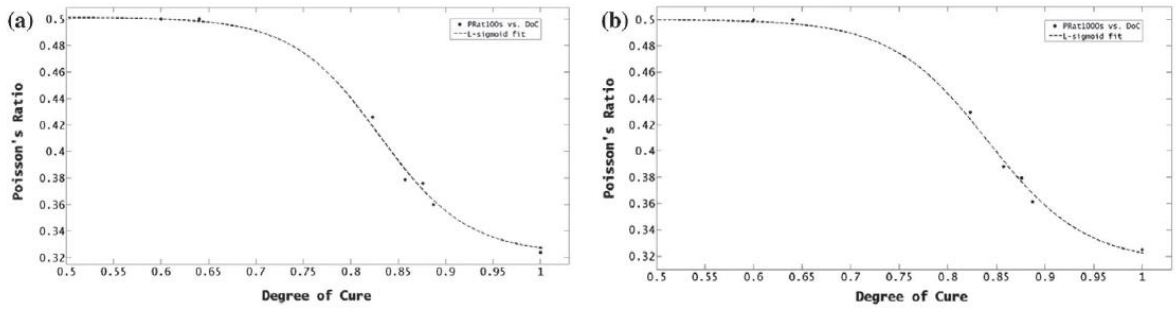


Figure 73 Poisson's ratio vs. degree of cure (a) 100 seconds and (b) 1000 seconds [76]

The time-domain data was converted to frequency domain using the Christensen approximation. The reason for this is unclear as all the viscoelastic analysis is typically done in the time-domain. Use of approximate conversion introduces additional uncertainties in the data associated with numerical errors from conversion. A master curve is shown in Figure 74. The master curve has several gaps and does not follow a general increasing trend indicating inaccuracies and uncertainties in the measured data. Additionally, it was not possible to determine the equilibrium Poisson's ratio as the test temperature were much below $T_g(p)$ of the epoxy.

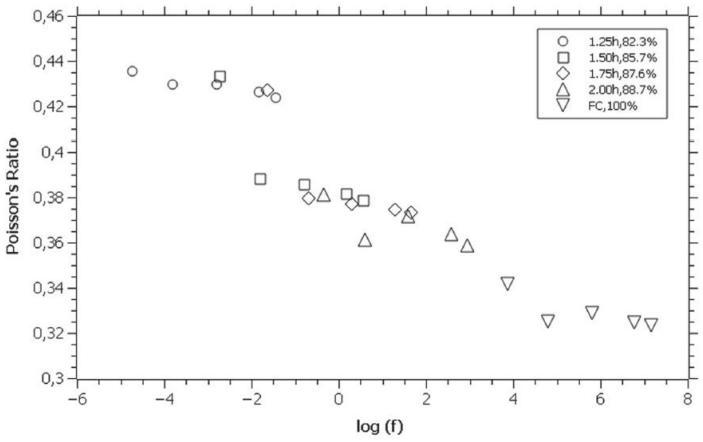


Figure 74 Master curve of Poisson's ratio obtained with horizontal shifting [76]

7.3. Proposed Method

It is clear that to be able to conduct cure-extent dependent viscoelastic analysis, following properties need to be measured experimentally –

(1) Equilibrium moduli as a function of cure extent

(2) Cure-dependent shift-factors - $a_p(p)$

Measurement of each set of properties is challenging, and each measurement poses unique challenges for which different experiments have to be designed. Section 7.3.1 and 7.3.2 discusses proposed methodologies and challenges to determine equilibrium moduli and cure-extent dependent shift-factors, respectively.

7.3.1. Proposed equilibrium moduli measurement procedure

It is necessary to measure the evolution of equilibrium moduli as a function of cure extent to be able to determine cure-dependent viscoelastic behavior of the EMC. As described before, two sets of viscoelastic properties are required to be able to describe viscoelastic behavior of a

material completely. In this thesis two sets of equilibrium moduli were measured – Young's equilibrium moduli ($E_\infty(p)$) and bulk equilibrium moduli - $K_\infty(p)$.

The main challenge for the measurement that involves a partially-cured EMC is that the relaxation and cure of the EMC occurs simultaneously. Equilibrium moduli can only be determined when EMC relaxes completely. The complete relaxation can be achieved above T_g where the curing-rate is also high. A special measurement procedure needs to be developed, through which the EMC moduli above T_g can be determined quickly at a near isocure state. To be able to determine temperatures for testing - T_{test} for various cure extents, it is first necessary to understand the evolution of cure-dependent glass transition temperature $T_g(p)$ during curing. The $T_g(p)$ of the EMC at various cure extents was determined first using differential scanning calorimeter (DSC) in section 7.4.1.

Next, it was necessary to understand the gel point (p_{gel}) of the material to be ensure that the viscoelastic testing is conducted above p_{gel}. Additionally, p_{gel} is also required in determination of the evolution equation. The gel-point was determined using dielectrometry described in section 7.4.2.

To establish a temperature to be used for testing partially-cured specimens, the test temperature - T_{test} should be sufficiently above the $T_g(p)$ of the partially-cured EMC being tested. The procedures to choose test temperature and the experiment to determine equilibrium moduli without extra curing is described in section 7.4.3.

Finally, an evolution model needs to be fit to the experimental data to describe the behavior as a function of cure extent. The evolution equation shown in Eq. (94) was used to describe evolution of shear equilibrium moduli in a thermoset during curing. Similar calculations can be done for other viscoelastic functions as shown below.

For a general viscoelastic function – $\mathcal{M}$, the evolution of the equilibrium value ($\mathcal{M}_\infty$) is directly proportional to $\left(p^2 - p_{gel}^2\right)^n$(in a two-part epoxy system). The equilibrium viscoelastic function can be expressed as:

$$\left(\mathcal{M}_\infty(p) - \mathcal{M}_\infty^{gel}\right) \propto \left(p^2 - p_{gel}^2\right)^n$$

$$\frac{\mathcal{M}_\infty(p) - \mathcal{M}_\infty^{gel}}{\mathcal{M}_\infty^{f} - \mathcal{M}_\infty^{gel}} = \left(\frac{p^2 - p_{gel}^2}{1 - p_{gel}^2}\right)^{n_E} \tag{96}$$

where $\mathcal{M}_\infty^{f}$ and $\mathcal{M}_\infty^{gel}$ are the values of the function at fully-cured state and gel point, respectively. The individual evolution equations for the measured equilibrium moduli are shown in section 7.3.4 and fitted to the measured experimental data.

7.3.2. Proposed cure-dependent shift factor measurement procedure

It is necessary to measure cure-dependent shift-factors ($a_p(p)$) to be able to determine cure-dependent viscoelastic behavior of the EMC at various cure extents. The main challenge is that the measurements need to be conducted at low temperatures ($T_{test} \leq T_g(p)$) while ensuring that the EMC is in a near isocure state during the test. Although the temperatures for testing are lower than $T_g(p)$, EMC still undergoes curing in the diffusion-controlled regime. Due to long duration of testing required, the amount of curing cannot be ignored. It is thus necessary to first determine cure kinetics of EMC in the diffusion-controlled region. The procedure and methodology to determine diffusion-controlled cure kinetics of EMC is described in section 7.5.1

To measure cure-dependent shift-factors for EMC ($a_p(p)$), several partially-cured samples with known extent of cure were subjected to viscoelastic testing. The testing was conducted using multi-frequency temperature sweeping (MFT) on a DMA machine. The testing was conducted at

temperature below or near $T_g(p)$ of the material to ensure that the reaction rate is slow under the diffusion control.

The amount of extra curing during the testing was determined using the diffusion kinetics, and it was ensured that the material was in a near isocure state ($\Delta p \sim 1\%$). The master curves were shifted to determine cure-dependent shift-factors ($a_p(p)$). The procedure for the partially-cured viscoelastic testing and the methodology to determine $a_p(p)$ is described in section 7.5.2.

7.4. Equilibrium Moduli Measurements

7.4.1. Measurement of $T_g(p)$ using DSC

Glass transition temperature ($T_g(p)$) governs when the mechanical behavior of material transition from glassy region to rubber region. The polymer exhibits large time and temperature dependent behavior as it transitions over $T_g(p)$. The equilibrium moduli can only be determined accurately and in realistic time-scales only if the test temperature is above $T_g(p)$. $T_g(p)$ is measured with a differential scanning calorimeter (DSC) using the partially-cured EMC with a known cure extent.

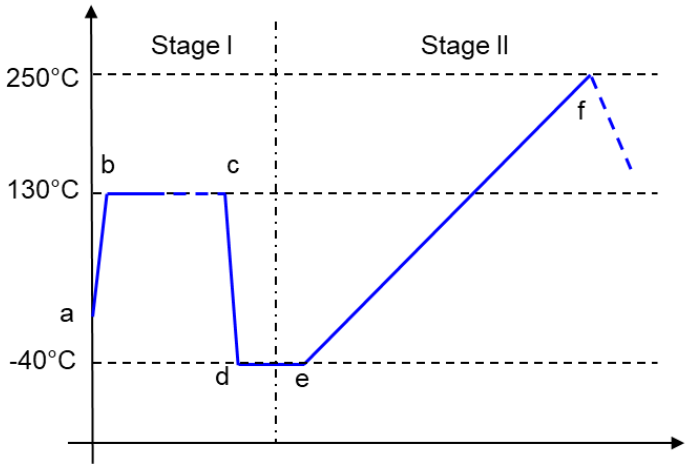


Figure 75 Temperature profile followed in DSC to determine $T_g(p)$ of the material

The temperature profile used to determine $T_g(p)$ is illustrated in Figure 75.. An uncured EMC sample was first partially cured for a known amount of time (3, 5, 10 min etc.), indicated by step (a-b-c). The partially cured specimens were rapidly cooled to -40°C (c-d). Finally, EMC was heated at a linear temperature ramp rate of 10°C/min (e-f) (1) to measure the residual heat released to determine uncured extent $(1 - p)$ and (2) to determine the $T_g(p)$ of EMC.

The heat flow rate measured during the dynamic ramping stage (e-f) is shown in Figure 76. The $T_g(p)$ is determined by measuring the mid-point of the specific heat capacity (C_p) transition during the ramping stage. It is clear from the plots that $T_g(p)$ increases with the increasing cure-extent during the isothermal curing step.

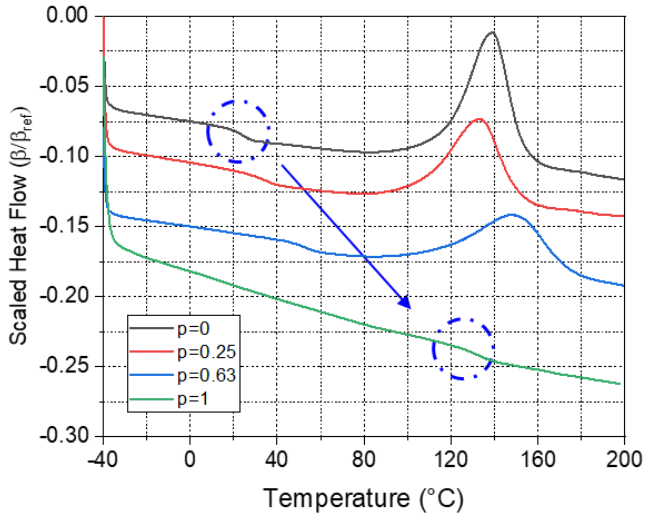


Figure 76 Heat flow rate vs Temperature during dynamic ramping of partially cured specimens at various cure extents

The values of $T_g(p)$ are plotted as a function of cure-extent, they are fitted to the DiBenedetto (DB) equation [127]:

$$\frac{T_g(p) - T_{g0}}{T_{g\infty} - T_{g0}} = \frac{\lambda p}{1 - (1 - \lambda)p}$$

$$T_{g0} = 23.85°C \tag{97}$$

$$T_{g\infty} = 130.73°C$$

$$\lambda_1 = 0.378$$

where T_{g0} and $T_{g\infty}$ are glass transition temperature of uncured and fully-cured EMC respectively. A comparison of the DiBenedetto fitting with the experimentally measure data is shown in Figure 77. It is clear from the figure that the data agrees very well with the fitting.

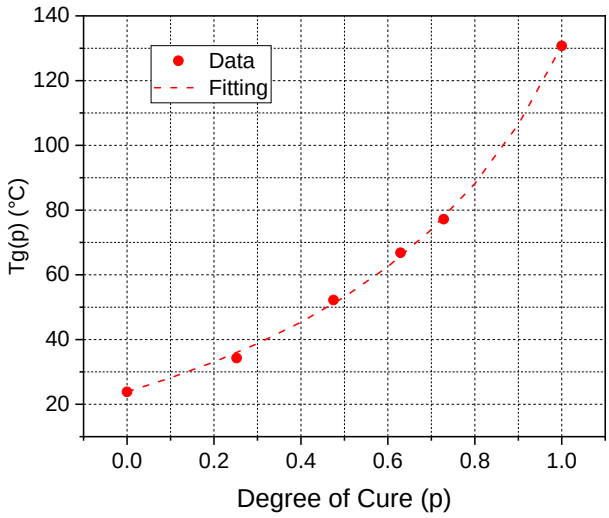
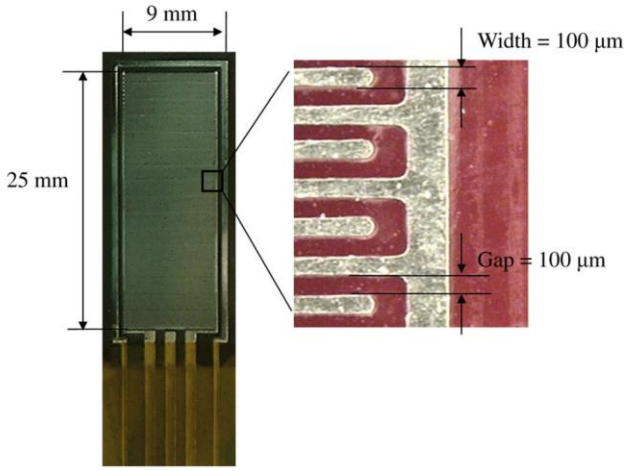


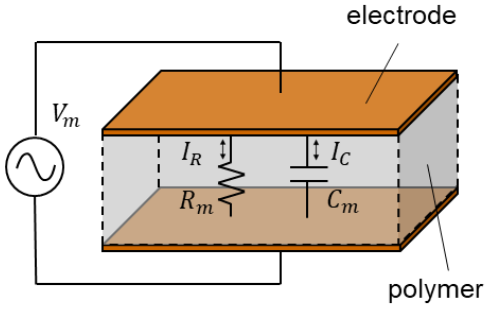
Figure 77 Evolution of glass transition temperature - $T_g(p)$ during curing

7.4.2. Measurement of gel point (p_{gel})

Dielectrometry is one of the methods to determine the gel point of thermosetting polymers [128]. In dielectrometry, the movement of the dipoles and ions in the polymer is monitored by measuring the impedance (Z) of the system, and the gel point can be detected based on the changes of the movement during the curing. A dielectric sensor was used to determine the gel point of carbon fiber epoxy composite materials [129]. The sensor is shown in Figure 78 (a). The dielectric sensor consists of two long copper electrodes with opposite polarity and a base film made of a polyimide film. For the measurement, the sensor is embedded in composite materials, and the composite forms a capacitor. The composite material can be modeled as a parallel circuit of resistance R_m and capacitance C_m, as illustrated in Figure 78 (b) [129].



(a)



(b)

Figure 78 (a) Dielectric sensor, (b) equivalent electrical circuit model for polymer material [129].

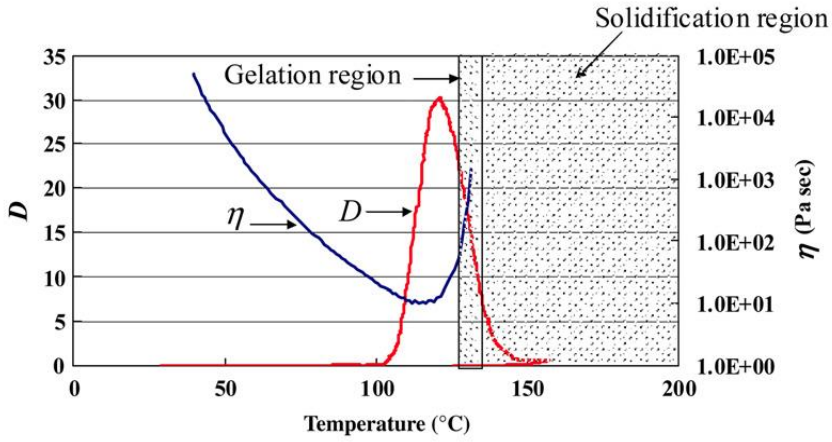
The dissipation factor *D* for the equivalent circuit can be defined by the following equation [130]:

$$D = \left|\frac{E_l}{E_s}\right| = \left|\frac{I_R \cdot V_m}{I_C \cdot V_m}\right| = \left|\frac{I_R}{I_C}\right| = \left|\frac{Z_C}{Z_R}\right| = \frac{1}{\omega \cdot R_m \cdot C_m} \quad (98)$$

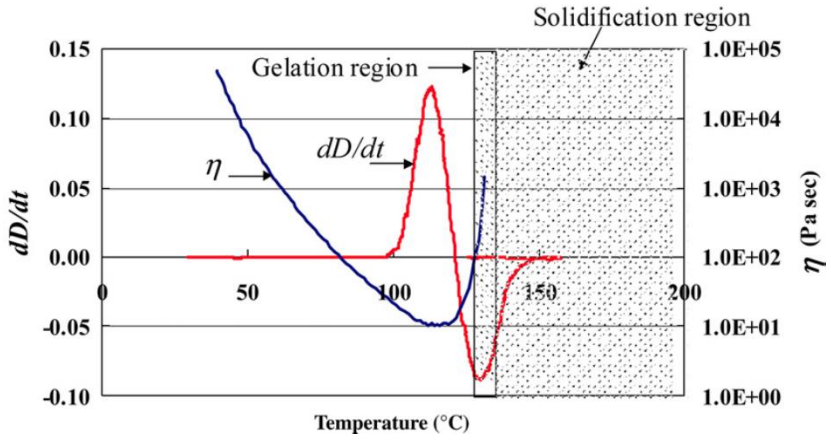
where *I* is the electric current, *Z* is the equivalent impedance, V_m is the alternating voltage with an angular frequency ω applied to the circuit, *R* is the resistance, and *C* is the capacitance of the equivalent circuit model. *D* represents a ratio between the amount of energy losses (E_l) caused by the movements of dipoles and ions and the energy supplied to the EMC (E_s) [131], and it is related

to the degree of movement [129]. In the application, an R-L-C meter with 1 kHz frequency was used, and dissipation D and the rate of dissipation factor (dD/dt) were monitored during the curing process of the epoxy resin. When the polymer is heated, the viscosity gets lower, and D is expected to be the maximum when the viscosity of the epoxy resin is the lowest. As the extent of cure increases, the viscosity increases, and D starts dropping. At the gel point, the dissipation factor decreases very quickly, and the point where dD/dt becomes the minimum indicates the gel point of the polymer [129].

The measurement result of viscosity, D, and dD/dt during the heating at the rate of 3 °C/min is shown in Figure 79 (a) and (b), respectively. The gelation region was determined based on the viscosity, where the viscosity became 100 Pa·s. The maximum D occurred when the viscosity was the lowest, while dD/dt at the gel point became the minimum because D decreased quickly near the gel point.



(a)



(b)

Figure 79. Experimental results of (a) D and viscosity, and (b) dD/dt and viscosity during the curing process [129]

7.4.3. Gel point determination of EMC

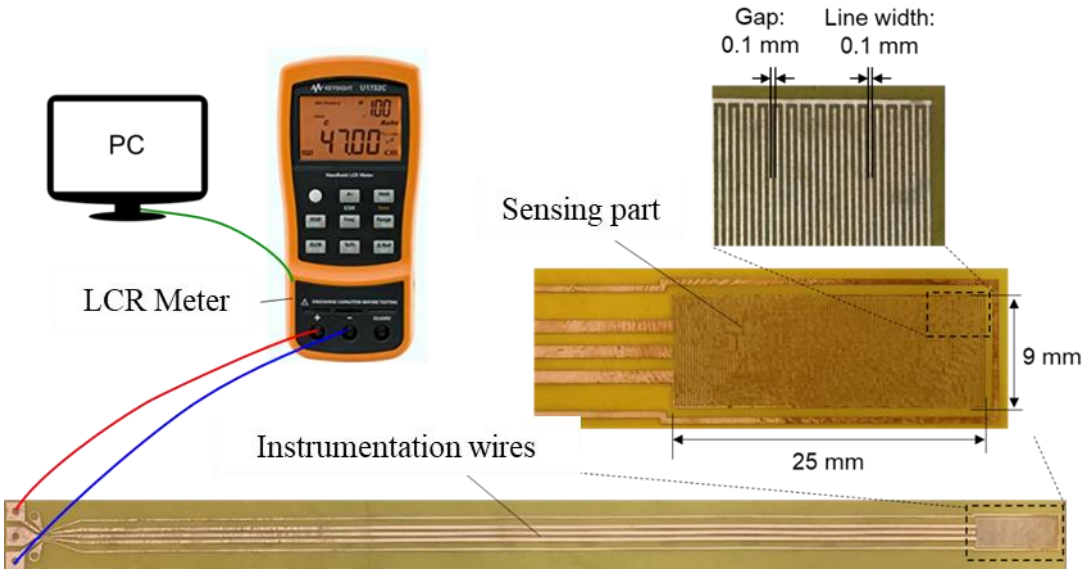
In this work, the gel point of the EMC is determined by using the dielectrometry. The configuration of the measurement setup is shown in Figure 80. In the sensor, copper lines are printed on the dielectric sheet like shown in Figure 80 (a) with a pitch of 0.1 mm. The other side of the sensor is connected to the LCR meter, and the measured dissipation factor is recorded by a PC.

For the EMC measurement, the EMC needs to uniformly cover the sensing part of the dielectric sensor, like illustrated in Figure 80 (b). For the gel point determination, the EMC needs to be heated to the cure temperature (T_{cure}) so that the EMC powder melts and covers the sensor uniformly. The sensor is directly kept on the conduction heater (HCP304SC: INSTEC). The EMC pellet is then crushed into a powder form, and a Kapton mold is made to contain the EMC during the measurement. A thermocouple is placed right next to the dielectric sensor to monitor the

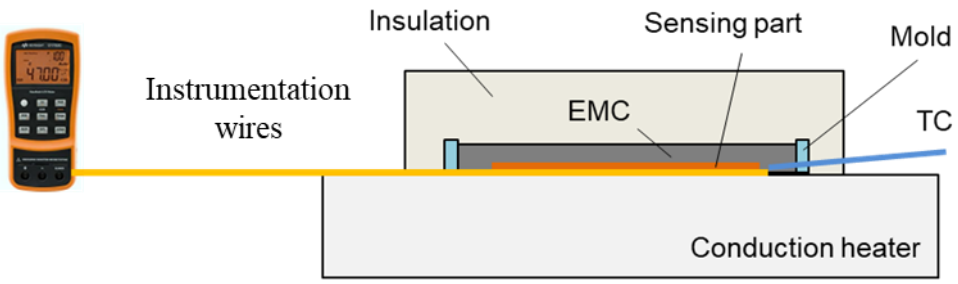
temperature continuously during curing. An insulation box is used to cover the setup to maintain uniform temperature over the sensing region.

The frequency of the LCR meter is set to 100 Hz, and the dissipation factor is monitored continuously. The setup is first preheated to 80°C before the measurement starts. The preheating step is used to soften the EMC such that it can spread uniformly over the sensor. At this temperature, the amount of curing can be considered negligible ($\Delta p < 0.1\%$). At the preheating temperature, the EMC is soft but very viscous. A gentle pressure using a plunger is applied to uniformly spread the EMC over the sensing region.

The setup is then heated to the cure temperature at 130°C, and the temperature maintained. The temperature profile with the linear temperature increase was initially considered, but it was not chosen because the temperature dependent dissipation factor of the EMC was observed.



(a)

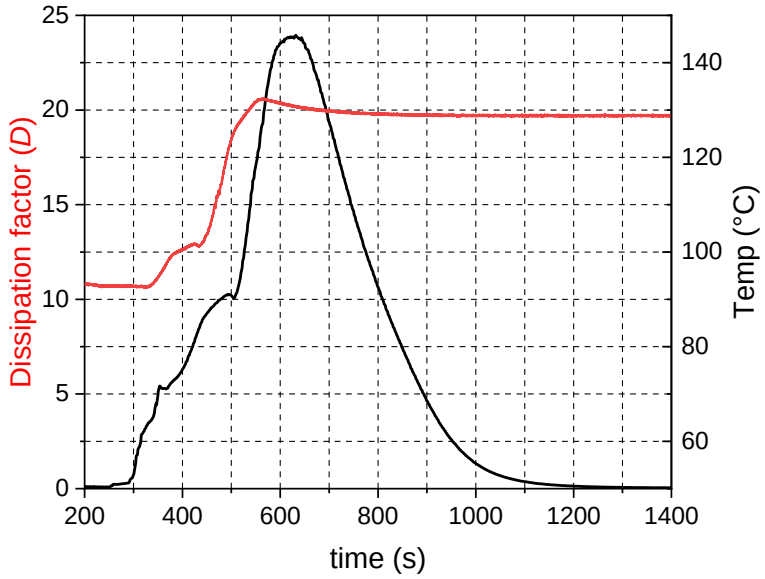


(b)

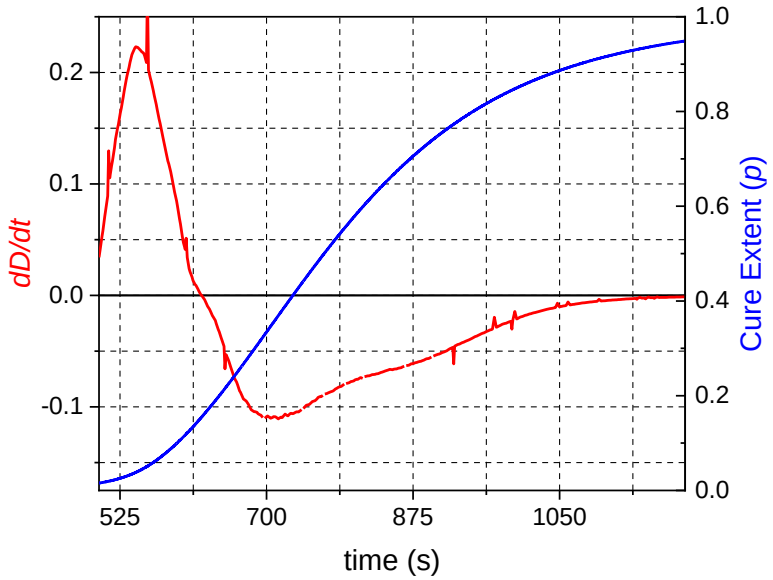
Figure 80. Illustration of the (a) dielectric sensor and electrical connection and (b) measurement setup.

The dissipation factor measurement result is shown in Figure 81. After the EMC is loaded, D increases as the viscosity of the EMC gets lower while heating. As the curing starts occurring, the viscosity of the increases, and D decreases after reaching its peak. The EMC is still in liquid state when the cure temperature is reached. This is done to ensure that the gel point measurement is done under isothermal conditions (T_{cure}) to avoid any effects of temperature-dependent D.

One the EMC reaches the T_{cure} the curing occurs continuously and D decreases very quickly due to increase in viscosity (or reduction in mobility of ions). The gel point is determined where dD/dt becomes the minimum, as marked in Figure 81(b).



(a)



(b)

Figure 81. Result of the dissipation factor measurement, (a) dissipation factor and temperature, (b) rate of the dissipation factor change as a function of time.

The cure kinetics determined previous had to be used to determine the gel point based on the dielectrometry result. The extent of cure at the gel point was determined based on the temperature profile recorded using the thermocouple (shown in Figure 81 (a) with red line). The cure extent as a function of time is also shown in Figure 81 (b). The gel point is defined as the minimum of the dD/dt, which is determined to be $p_{gel} = 0.387$.

7.4.4. Experiments to measure the equilibrium moduli

To establish a temperature to be used for testing partially-cured specimens, the test temperature - T_{test} should be sufficiently above the $T_g(p)$ of the partially-cured EMC being tested. If the test temperature is sufficiently high, the equilibrium modulus, can simply be measured by conducting monotonic testing and by taking a slope of the stress vs. strain curve.

The testing temperatures for the equilibrium moduli measurements were chosen based on the $T_g(p)$ of the partially-cured EMC determined in previous section. The testing temperature (T_{test}) were chosen such that the difference between the T_{test} and $T_g(p)$ was at least 40°C to ensure complete relaxation.

Two sets of temperature were chosen based on degree of cure of the partially-cured material - $p = 0.5$ to 0.7, the test temperature was chosen to be 120°C and for $p = 0.7\ to\ 0.9$, the test temperature was chosen to be 150°C. A testing time of 10 seconds was chosen such that the specimen curing was minimal during the measurement such as to maintain a near isocure state.

A summary of expected change in cure extent along with the glass transition temperature of the partially cured EMC is shown in Table 5. It can be seen that the maximum expected change in cure extent at 150°C is about ~1% (near isocure state) while the minimum difference between T_{test} and $T_g(p)$ is larger than 40°C ensuring complete relaxation.

Table 5 Summary of change in cure extent (Δp) over 10 seconds and $T_g(p)$ of the EMC at various cure extents and proposed measurement temperatures.

p_{test}	T_{test}	Δp	$T_g(p)$
0.5	120°C	0.0072	53.5 °C
0.6	120°C	0.0063	62.8°C
0.7	120°C	0.0051	74.3°C
0.8	150°C	0.011	89.8°C
0.9	150°C	0.008	107.5°C

The partially-cured specimen and the chamber should not be heated together above T_g of the material, simply because extra curing while being heated to the test temperature is too excessive. To mitigate this issue, the test chambers were heated to the testing temperature prior to inserting the sample. The samples were inserted just before the test was conducted to ensure ignorable extra curing.

For Young's equilibrium moduli measurements, a sample with dimension of 20 mm x 7 mm x 2.5 mm was fabricated and mounted on the fixture once the system was at the test temperature. The sample inserted in DMA machine required 1.2 minutes (~70 seconds) to heat from room temperature the target temperature at 150°C and stabilize completely. The amount of curing estimated during the heating was about $\Delta p = 0.055$. This additional cure extent was included in the calculations while determining cure extent at the time of testing.

The loading was applied using displacement control. A linear displacement rate of 0.002 mm/s was applied for 10 seconds and the force vs. deflection data was recorded. A plot of force vs. deflection data and the corresponding stress vs. strain data are shown in Figure 82 (a) and (b), respectively. The slope of the curves was obtained using linear fitting to determine the $E_\infty(p)$.

The results of $E_\infty(p)$ are shown in Figure 84 (black scatter plot). The R^2 for each fit were greater than 0.99 indicating that the lines are linear and there is minimal viscoelastic behavior

causing nonlinearity. The plot clearly shows an increase in $E_\infty(p)$ with cure extent, the modulus increases sharply after $p = 0.8$. The E_∞^f (at $p = 1$) was determined previous during fully-cured Young's moduli tests.

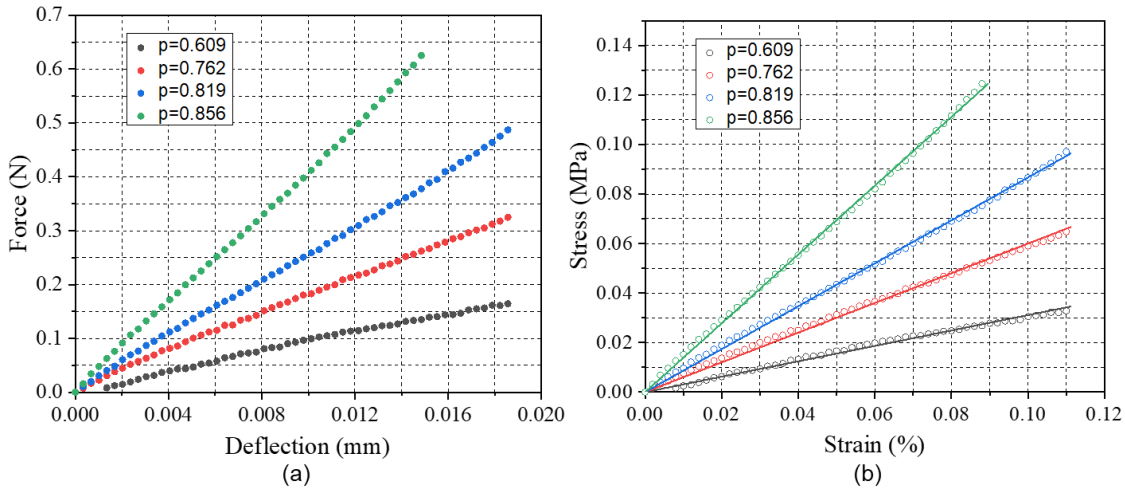


Figure 82 Results of monotonic testing data using DMA for Young's equilibrium modulus measurements – (a)Force vs deflection data, and (b) Stress vs Strain data

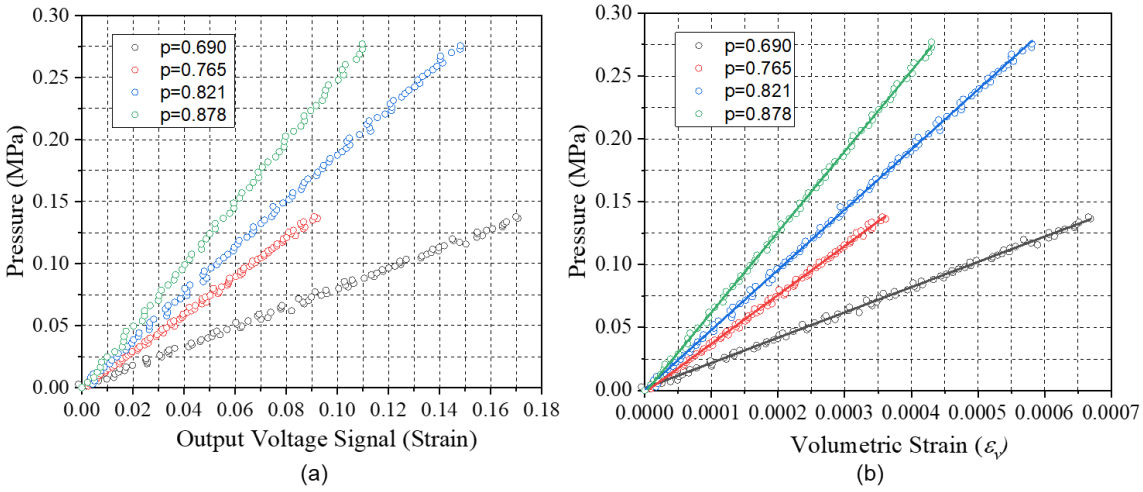


Figure 83 Results of monotonic testing data using hydrostatic test setup for bulk equilibrium modulus measurements – (a) Pressure vs. output voltage strain signal and, (b) pressure vs volumetric strain.

For bulk equilibrium moduli measurements, a sample size of 15 mm x 10 mm x 6 mm was fabricated and inserted into the chamber once the system was at the target temperature. A swivel-type joint was used for attaching the compression sealing unit to the chamber. Swivel joints can rotate freely before locking which allowed for quick locking without twisting the instrumentation wires.

After the specimen was sealed inside the system, it took about 2.25 minutes (130 seconds) to heat the sample from room temperature to the target temperature of 150°C and stabilize completely. The total amount of curing expected was estimated to be about $\Delta p = 0.106$. This additional change in cure extent was included while determining the cure extent during the tests.

The loading was applied using pressure control. The LabVIEW program was utilized to apply pressure control at a fixed linear rate. Two levels of pressure rate were applied - $p = 0.6$ to 0.8 - 2 psi/s (0.0138 MPa/s) and $p = 0.8$ to 1 - 4 psi/s (0.0275 MPa/s) for 10 seconds and the strain response was recorded.

A plot of pressure vs. raw strain signal and the corresponding hydrostatic stress vs. volumetric strain is shown in Figure 83 (a) and (b), respectively. The slope of the curves was obtained using line fitting to determine the $K_\infty(p)$. The results of $K_\infty(p)$ are shown in Figure 84 (blue scatter plot). The R^2 for each fit were greater than 0.99 indicating that the lines are linear and there is minimal viscoelastic behavior causing nonlinearity.

It can be clearly seen that bulk modulus increases with cure extents. However, it is significantly larger than Young's modulus, which is expected as the material becomes more incompressible ($\nu_\infty \rightarrow 0.5$). At the gel-point, the bulk modulus will theoretically have an infinite value as the EMC is in liquid state and the Poisson's ratio is 0.5.

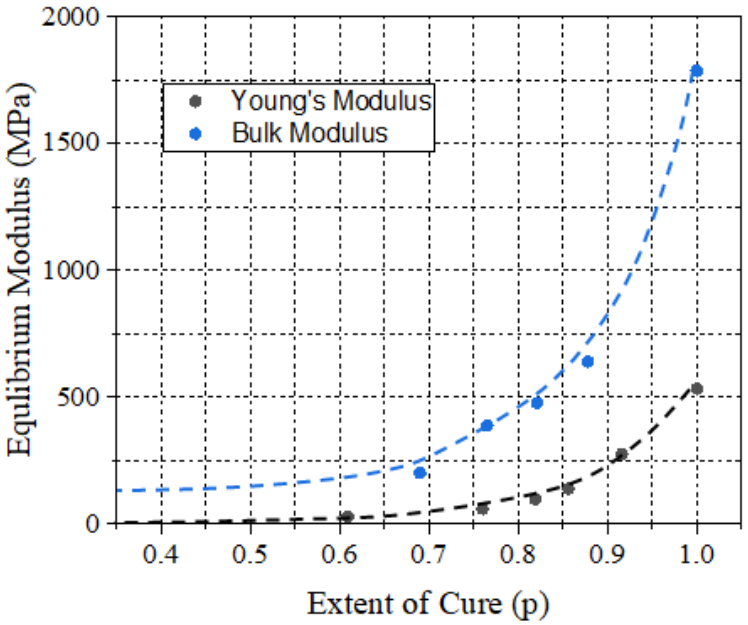


Figure 84 Measured values of equilibrium moduli – (a) $E_\infty(p)$ (black scatter plot) and, (b) $K_\infty(p)$ (blue scatter plot)

7.4.5. Evolution model calculation

Using the evolution equations for general viscoelastic function - $\mathcal{M}$ shown in Eq. (96), an equation for Young's equilibrium modulus can be derived as follows:

$$\begin{aligned} (E_\infty(p) - E_\infty^{gel}) &\propto \left(p^2 - p_{gel}^2\right)^{n_E} \\ \frac{E_\infty(p) - E_\infty^{gel}}{E_\infty^f - E_\infty^{gel}} &= \left(\frac{p^2 - p_{gel}^2}{1 - p_{gel}^2}\right)^{n_E} \\ \frac{E_\infty(p)}{E_\infty^f} &= \left(\frac{p^2 - p_{gel}^2}{1 - p_{gel}^2}\right)^{n_E} \end{aligned} \tag{99}$$

where E_∞^f is the equilibrium Young's modulus when the polymer is fully-cured ($E_\infty^f = 534.5$ MPa) and E_∞^{gel} is the Young's modulus at gel point. The EMC is effectively liquid at the gel point and Young's modulus can be regarded as "0" MPa. Eq. (99) was fitted to the Young's equilibrium

modulus data in Figure 84 to determine the evolution component - n_E. A comparison of the model fit to the experimental data is shown in Figure 85. The model fit seems to be agreeing well with the data (R^2= 0.994) indicating that the percolation model works well. The evolution component was determined to be $n_E = 3.409$.

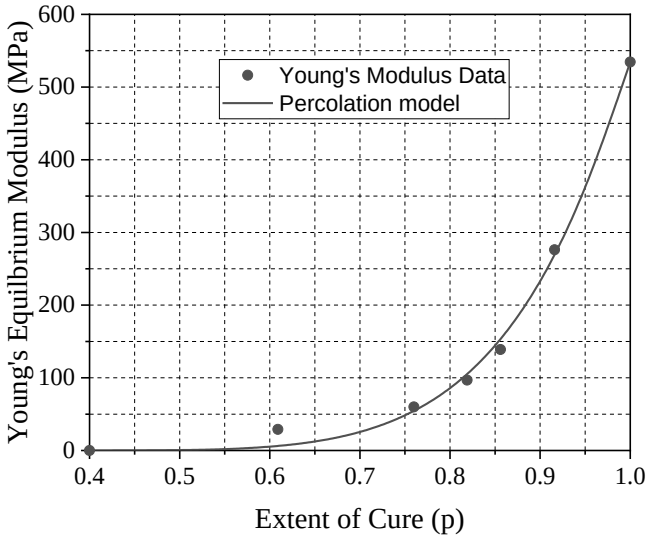


Figure 85 Comparison of $E_\infty(p)$ data with the percolation model fitting

Similar equations can be derived for bulk modulus evolution as shown below:

$$(K_\infty(p) - K_\infty^{gel}) \propto \left(p^2 - p_{gel}^2\right)^{n_K}$$

$$\frac{K_\infty(p) - K_\infty^{gel}}{K_\infty^f - K_\infty^{gel}} = \left(\frac{p^2 - p_{gel}^2}{1 - p_{gel}^2}\right)^{n_K} \tag{100}$$

$$\frac{K_\infty(p) - \infty}{K_\infty^f - \infty} \approx \frac{\infty}{\infty} \rightarrow \text{Indeterminate Form}$$

However, the equations break down near the gel-point as the material becomes incompressible. Due to the incompressibility, the bulk modulus approaches infinity ($K_\infty^{gel} \rightarrow \infty$) and thus the equation becomes an indeterminate form. To resolve this issue of singularity, the

percolation model was instead fit to shear modulus. The shear equilibrium modulus - $G_\infty(p)$ was calculated using the measured $K_\infty(p)$ data and the $E_\infty(p)$ determined using the model. Linear elastic equations can be used for calculation for $G_\infty(p)$ as there is no viscoelastic behavior. The equation for determining $G_\infty(p)$ from $K_\infty(p)$ and $E_\infty(p)$ is shown below:

$$G_\infty(p) = \frac{3K_\infty(p)E_\infty(p)}{9K_\infty(p) - E_\infty(p)} \tag{101}$$

The evolution equation for shear modulus - $G_\infty(p)$ is as follows:

$$\begin{gathered}(G_\infty(p) - G_\infty^{gel}) \propto \left(p^2 - p_{gel}^2\right)^{n_G} \\ \frac{G_\infty(p) - G_\infty^{gel}}{G_\infty^f - G_\infty^{gel}} = \left(\frac{p^2 - p_{gel}^2}{1 - p_{gel}^2}\right)^{n_G} \\ \frac{G_\infty(p)}{G_\infty^f} = \left(\frac{p^2 - p_{gel}^2}{1 - p_{gel}^2}\right)^{n_G}\end{gathered} \tag{102}$$

where G_∞^f is the equilibrium shear modulus when the polymer is fully-cured ($E_\infty^f = 534.5$ MPa) and G_∞^{gel} is the shear modulus at gel point. The EMC is effectively liquid at the gel point and the shear modulus can be regarded as "0" MPa. Eq. (102) was fitted to the shear equilibrium modulus data to determine the evolution component - n_G. A comparison of the model fit to the experimental data is shown in Figure 86. The model fit seems to be agreeing well with the data (R^2= 0.996) indicating that the percolation model works well. The evolution component was determined to be $n_G = 3.56$.

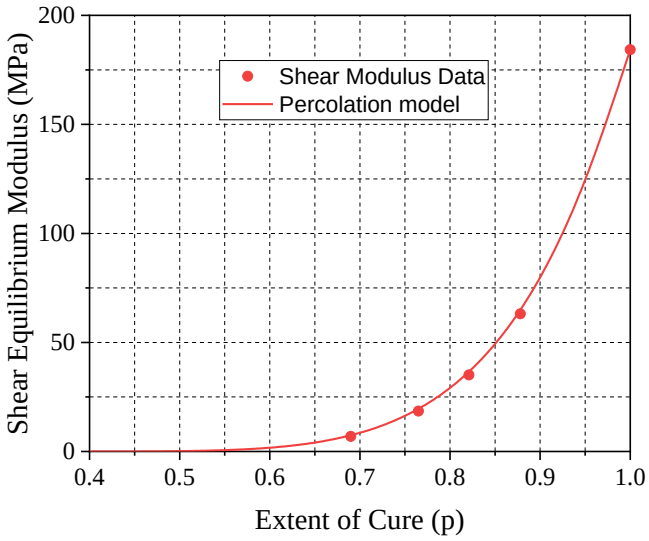


Figure 86 Comparison of $G_\infty(p)$ data with the percolation model fitting

Using the two evolution models - $E_\infty(p)$ and $G_\infty(p)$, other viscoelastic functions can be evaluated as a function of cure extent. The equilibrium viscoelastic functions as a function cure extent are shown in Figure 87. At the gel point - $p_{gel} = 0.387$, the material is practically liquid and the Poisson's ratio is 0.5. This causes bulk modulus to diverges to infinity and hence the theoretical asymptote.

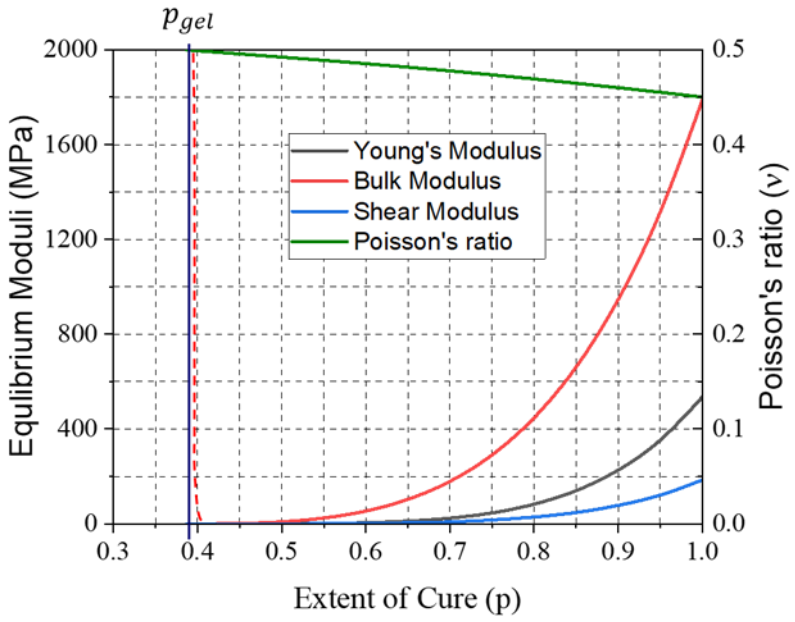


Figure 87 Plot of evolution of viscoelastic functions with cure extent

7.5. Cure-dependent Shift-factors Measurements

7.5.1. Measurement of diffusion-controlled cure-kinetics

When a polymer undergoes vitrification during curing, the reaction transitions from chemical-controlled mechanism to a diffusion-controlled mechanism. Vitrification is glass formation due to T_g of the polymer increasing from below T_c (cure temperature) to above T_c as a result of the curing reaction. In the glassy state, the rate of reaction (dp/dt) will undergo a significant decrease and falls below the chemical-controlled reaction rate as the reaction becomes dominated by the diffusion of the reactants through the medium.

A mathematical form for a general cure-kinetics reaction [132] can be expressed as:

$$\frac{dp}{dt} = k_c(T)[f_d(T_c, T_c - T_g(p))](1-p)^n p^m \tag{103}$$

where f_d is the diffusion-function, whose value is generally dependent on both cure temperature (T_c) and p. More specifically, the value of the function – f_d depends on the difference between T_c and $T_g(p)$ at any particular instant. The value of $f_d = 1$ when $T_c \gg T_g(p)$ and starts becoming smaller in the neighborhood of $T_g(p) \sim T_c$. k_c, n and m are the KS-model constants measured for the EMC in the chemical-control region. The values of these were determined in Chapter 3.

Several isothermal DSC tests were conducted at curing temperature (T_c) below $T_{g\infty}$ of the material. The results of cumulative heat released as a function of time are shown in Figure 88. The isothermal tests were conducted at 10°C intervals from 70°C to 120°C to understand the diffusion-controlled behavior of the EMC at various temperatures.

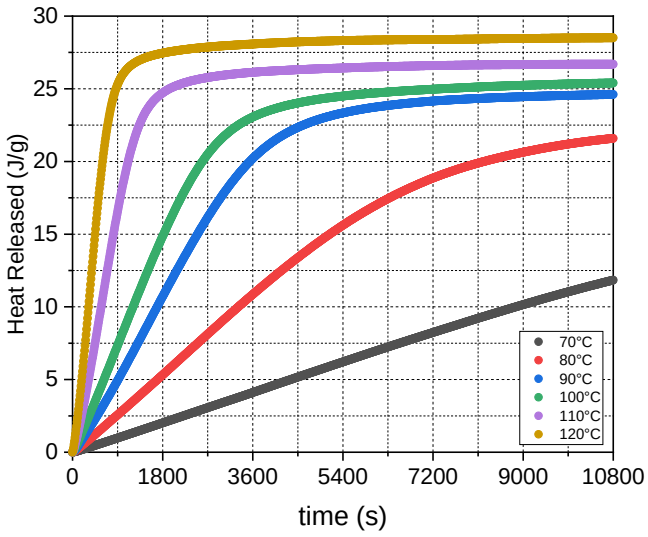


Figure 88 Cumulative heat released as a function of time obtained from DSC experiment

Taking logarithm of equation (103), the diffusion function can be expressed as follows:

$$\ln(f_d) = \ln\left(\frac{dp}{dt}\right)_{data} - \ln A - \frac{E_a}{RT_c} - n\ln(1 - p_{data}) - m\ln(p_{data}) \qquad (104)$$

The dp/dt and p obtained form the isothermal data in Figure 88 are substituted in Eq. (104) to obtain the value of diffusion function at each curing temperature (T_c). A plot of $\ln(f_d)$ vs. $\Delta T_g(p)$ using the data is shown in Figure 89 (a) for various cure temperatures, T_c. The plot clearly shows that when the $T_c \gg T_g(p)$, the value of $\ln(f_d)$ is nearly zero indicating that the reaction is under chemical control. However, as the $T_g(p)$ gradually gets closer to T_c, the reaction rate starts slowing down due to vitrification and the curing mechanism gradually shifts to diffusion-control.

In general polymers, the f_d is defined as follows [132]:

$$f_d(\Delta T_g) = \frac{k_d(T_c, p)}{k_c(T_c) + k_d(T, p)} \tag{105}$$

where $k_d(T_c, p)$ is the rate constant for diffusion-control and k_c is the chemical-control reaction constant determined previously. The rate constant - $k_d(T_c, p)$ is expressed as follows [132]:

$$k_d(T_c, p) = A_d \exp\left(-\frac{E_d}{RT_c}\right) \exp\left(-\frac{b}{c + d\left(T_c - T_g(p)\right)}\right) \tag{106}$$

where A_d is the rate coefficient, E_d is activation energy for diffusion control, and b, c and d are material constant which can be determined experimentally. It is important to note that the diffusion-function is very weak function of the cure-temperature (T_c) and does not show any specific trend. The activation energy term - E_d is 0 and the equation can be simplified further.

Thus, for the analysis and data fitting, f_d, was assumed to be a function of only $\Delta T_g(p)$. By combining the data at all cure temperatures, a single f_d vs $\Delta T_g(p)$ plot was made, and it is shown in Figure 89 (b). The shape of the data follows a family of mathematical functions represented using the following equation:

$$f_d(\Delta T_g) = \frac{1}{1 + \exp\left(-A(\Delta T_g(p) - B)\right)} \tag{107}$$

where A and B are material constants obtained from the experimental data.

Using a non-linear fitting program in MATLAB based on least-squares method (discussed in Chapter 3 and 4), the data in Figure 89 (b) was fitted to Eq. (107) to determine the material constants A and B. The values of the material constants were determined to be $A = 0.213\,°C^{-1}$ and $B = 7.723°C$, respectively. The model prediction result (R^2 = 0.99) is also shown in (b) indicating that the function represents the diffusion behavior accurately.

A cure extent data obtained from an isothermal DSC test at 90°C is compared with the model prediction using both diffusion and chemical control models in Figure 90. The prediction using chemical-control model initially agrees well with the isothermal data. However, as the $T_g(p)$ approaches T_c, the prediction using chemical-control model deviates significantly. The diffusion-control model is able to predict the behavior as the reaction enters diffusion-control domain.

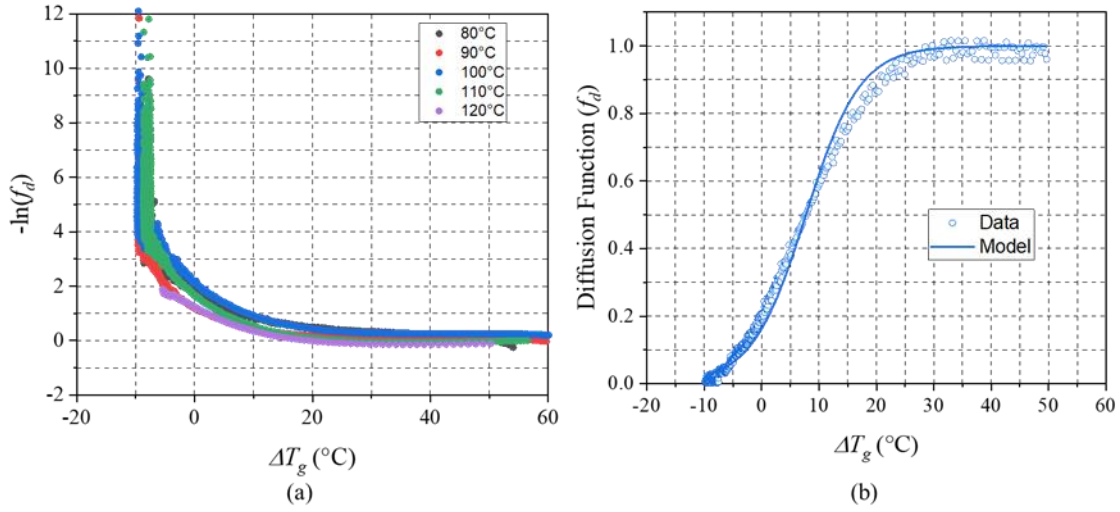


Figure 89 Diffusion function (f_d) for various cure temperatures (T_c) obtained for the isothermal data – (a) Plot of $-ln(f_d)$ vs. $\Delta T_g(p)$ and (b) comparison data vs prediction of diffusion function (f_d) vs $\Delta T_g(p)$

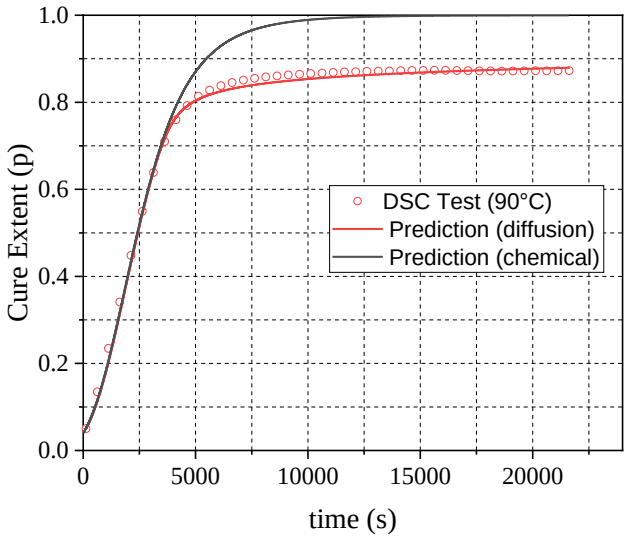


Figure 90 Comparison of model prediction (diffusion and chemical control) with isothermal DSC test data at 90°C

7.5.2. Determination of cure-dependent shift-factors ($a_p(p)$) using MFT sweeping

The time-cure superposition (TCS) was originally proposed in Ref. [71]. It is a concept similar to time-temperature superposition (TTS) but differs in the mechanism. The cause of TTS is relative friction between the molecular chains. However, the cause for TCS is a result of change in connectivity. The polymers neat-critical gel-state are geometrically self-similar, a change in the cure extent only results in change of the scale of cluster; i.e. the cluster becomes larger as curing increases [71].

This change in scale can then be expressed as proportional scaling of relaxation time (larger clusters relax more slowly) combine with larger equilibrium moduli due to increase in cluster size. The theory of TCS has been developed for unfilled-thermosets and soft thermoplastic polymers. However, EMC is a filled thermoset and it is necessary to confirm the validity of time-cure superposition and determine the corresponding cure-dependent shift-factors ($a_p(p)$).

To measure cure-dependent shift-factors for EMC, several partially-cured samples with known extent of cure - $p = 0.6$ to $p = 0.9$ were fabricated and subjected to viscoelastic testing using multi-frequency temperature sweeping (MFT) tests on the DMA machine. It was necessary to maintain a near isocure state to obtain accurate viscoelastic data for a given cure extent. Since, the testing was mainly conducted below or near $T_g(p)$ of the partially-cured EMC, diffusion-controlled cure kinetics determined in the previous section could be used to predict evolution of cure-extent during the test.

A multi-frequency temperature sweep test was conducted from -40°C with 10°C/step in the frequency range of 0.1 to 25 Hz (3 points per decade). It took about 15 and 10 minutes to heat and stabilize between each step below 30°C and above 30°C, respectively,

and about 75 seconds to conduct frequency sweep between 0.1 to 25 Hz. Using the temperature profile, the amount of curing was estimated for each cure extent tested. The test parameters - range of test temperature (T_{test}), glass transition temperature ($T_g(p)$) and expected amount of curing over the test duration is summarized in Table 6. It is worth noting that for $p = 0.6$, it was possible to exceed $T_g(p)$ of the material for testing. Although the reaction was under chemical control, the reaction rate at 70°C is slow enough to be able to run the test under near isocure state.

Table 6 Summary table of test parameters for MFT sweeping test for partially-cured EMC specimens

p_{test}	$T_g(p)$	T_{test}	Δp
0.6	62.8°C	-40 -70°C	0.011
0.7	74.3°C	-40 – 70°C	0.0092
0.8	89.8°C	-40- 90°C	0.013
0.9	107.5°C	-40 – 110°C	0.011

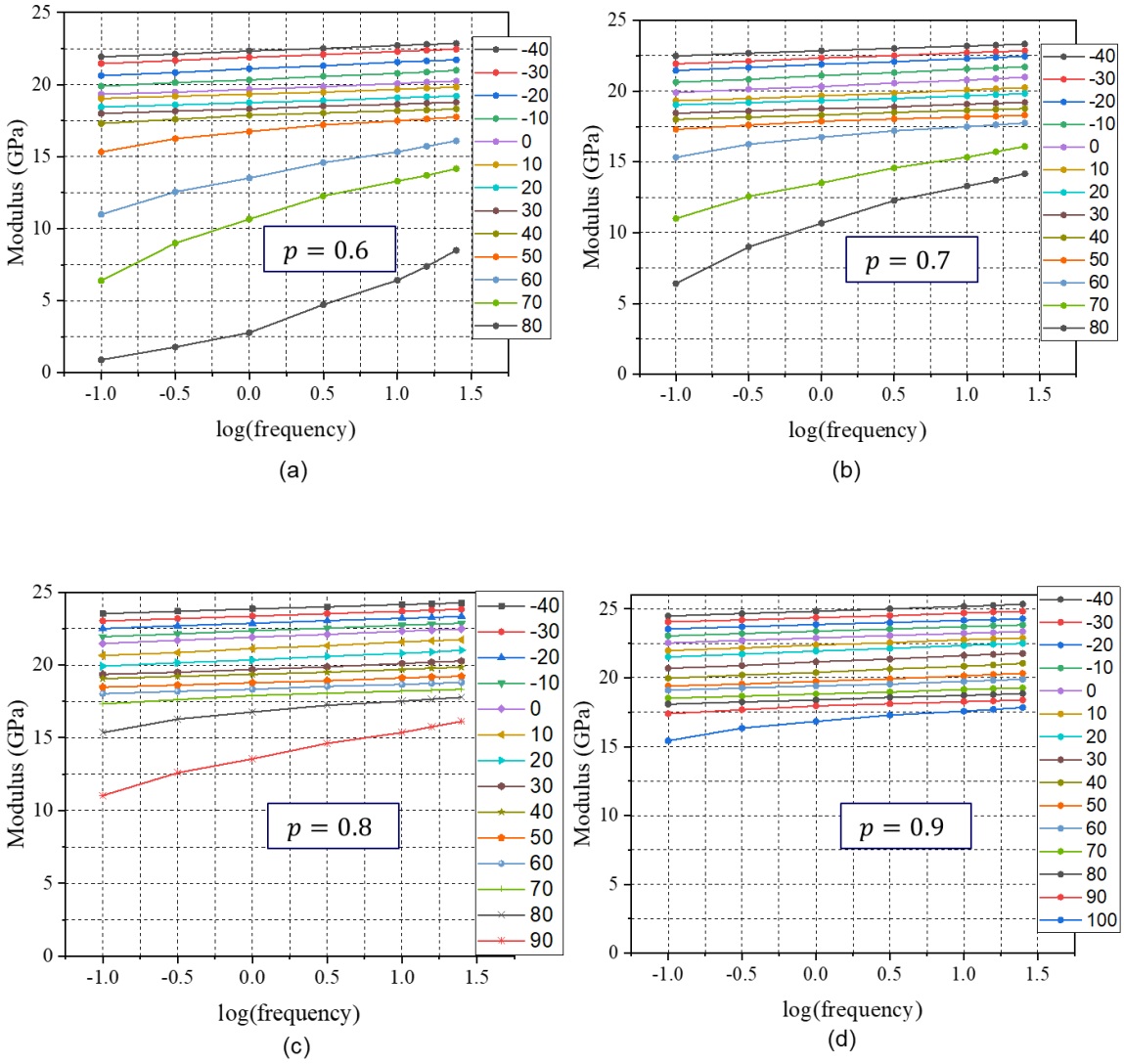


Figure 91 Raw storage modulus data of MFT sweeping tests conducted on partially-cured EMC specimen from $p = 0.6$ to $p = 0.9$

The results of MFT sweeping data are shown in Figure 91. The figures (a) to (d) represent storage modulus data from $p = 0.6$ to $p = 0.9$. Then storage modulus data was shifted to create sections of master curve at $T_{ref} = -40°C$. The section of master curves for partially-cured EMC are shown in Figure 92

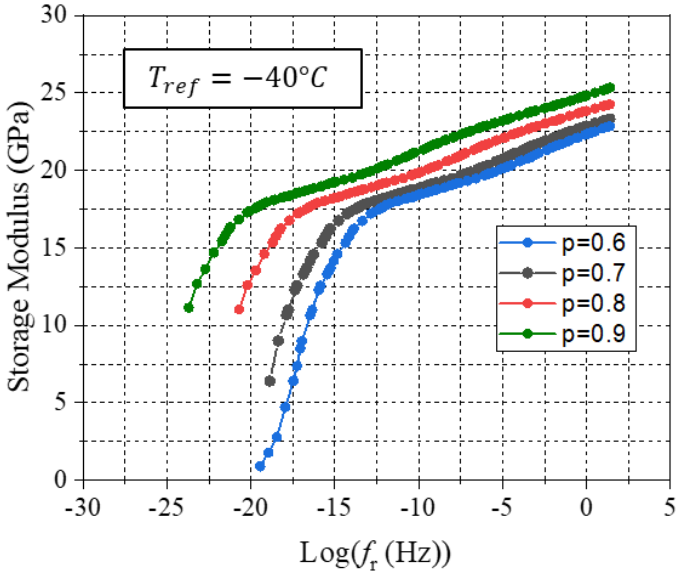


Figure 92 MFT results – master curves after shifting at $T_{ref} = -40°C$

Before determination of the cure-dependent shift-factors, it was necessary to normalize the master curves using E_G and $E_\infty(p)$ for scaling the data between 0 and 1. $E_\infty(p)$ for various cure extents was calculated using the evolution model in the previous section. The normalized master curves for various cure extents are shown in Figure 93.

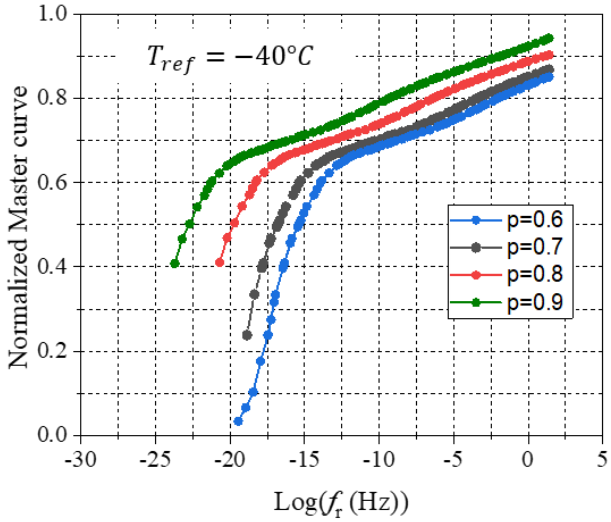


Figure 93 Normalized master curves for partially-cured EMC at $T_{ref} = -40°C$

The cure-dependent shift-factors ($\log a_p(p)$) were determined next by horizontally shifting the partially cured master curves to overlap with the fully-cured ($p = 1$) master curve. The results of TCS shifting are shown in Figure 94. The overlapped master curves are shown in (a) and the corresponding cure-dependent shift factors are shown in (b) (blue scatter plot). The master curves show a good overlap with the fully-cured master curve indicating that TCS is working for the EMC tested.

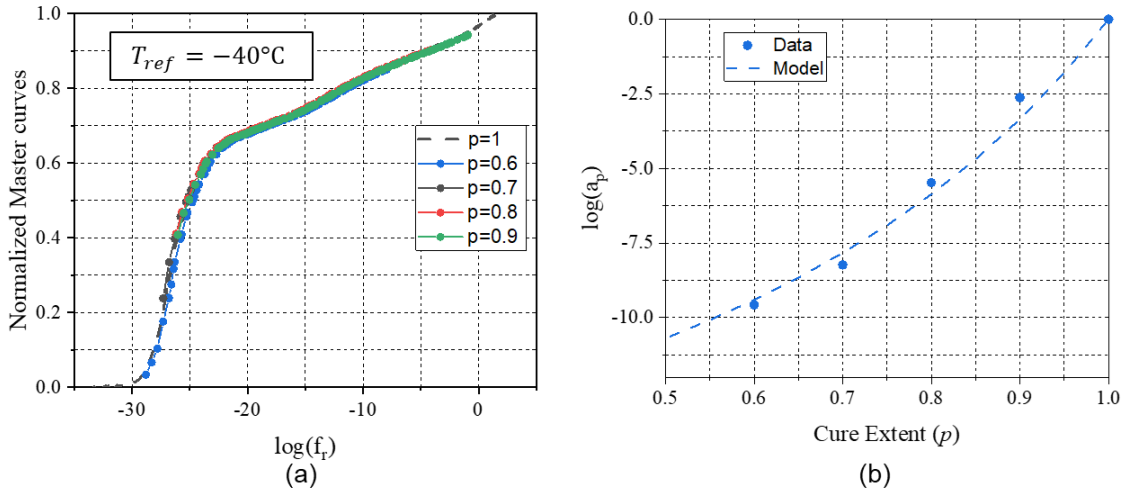


Figure 94 Results of TCS shifting – (a) Master curve after overlap, and, (b) Cure-dependent shift-factors ($\log a_p(p)$)

In TTS, it is common to use WLF equation for temperature-dependent shift-factors ($\log a_T$) in the glass transition and rubbery region of a polymer. WLF equation works well in the region where the relaxation rate at a given temperature (T) is equal to or higher than the reference temperature (T_{ref}) i.e., the shift-factors are negative.

In case of cure-dependent behavior, the reference degree of cure (p) is fully-cured state and the partially-cured specimens relax faster than the fully-cured polymer. A WLF type equation can be used to fit to a function form for cure-dependent shift-factors. Since, the WLF equation is temperature based, a following modification is proposed to the equations:

$$\log a_p(p) = \frac{-C_1\,(T_{g\infty} - T_g(p))}{C_2 + (T_{g\infty} - T_g(p))} \tag{108}$$

where T_{g_∞} is the fully-cured glass transition temperature, $T_g(p)$ is the glass-transition temperature at a given cure extent (p) and C_1 and C_2 are material-specific constants. $T_g(p)$ has already been determined previously in Eq. (97).

The experimental data was fitted to Eq. (108) to determine the constants $C_1 = 1.5036$ and $C_2 = 10.905$. A comparison of the model with the experimental data is shown in Figure 94 (b). The R^2 of the fitting was 0.98 indicating that the fitting works well.

7.5.2.1. Discussion: Temperature-dependent shift-factors ($\log a_T$) for partially-cured specimen

It is worth investigating the temperature-dependent shift factors ($\log a_T$) determined while generating master curves of partially-cured specimen shown in Figure 92. $\log a_T$ obtained from TTS shifting is shown in Figure 95.

It can be clearly observed that the temperature-dependent shift-factors are similar with respect to reference temperature within experimental error bound, which indicates that the shift-factors ($\log a_T(T)$) does not have a strong cure dependency in the glassy region and the neighborhood of T_g region.

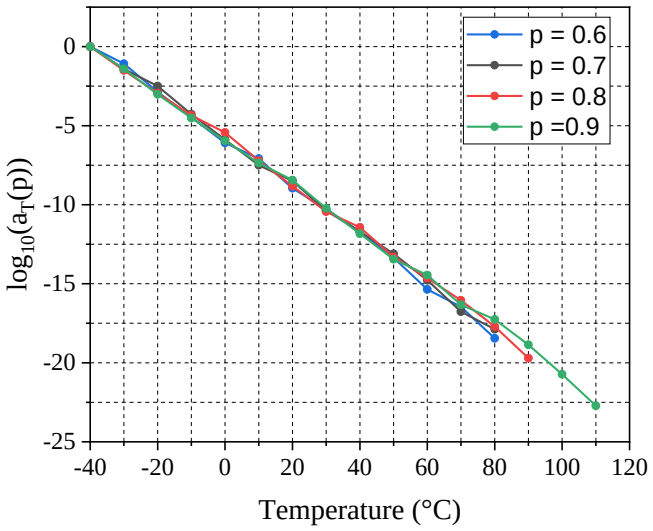


Figure 95 $\log a_T$ calculated while generating master curves for the partially-cured specimens tested

7.6. Implementation of Time-cure superposition (TCS) in a commercial FEM program

Commercial finite element method (FEM) softwares like ANSYS have inbuilt modules to run numerical models for LVE using time-temperature superposition (TTS). The constitutive governing equations using hereditary integral remain the same for cure-dependent viscoelastic behavior. Thus, the inbuilt solvers can be readily used to be able to run models for cure-dependent viscoelasticity. However, there are some differences between standard LVE and cure-dependent viscoelastic behavior which require some modifications to be able to accurately include the effects associated with curing.

Following are the effects which need to be included to be able to accurately run numerical models for cure-dependent viscoelastic behavior:

1) Evolution of cure-extent using cure-kinetics function - $p(t)$

2) Evolution of equilibrium moduli as the EMC cures - $G_\infty(p)$ and $K_\infty(p)$

3) Inclusion of shift-factors associated with time-cure superposition (TCS) - $\log a_P(p)$

For this thesis, an FEM implementation scheme has been developed considering a constant curing temperature (T_c). A cure extent (p) – thermal analogy (T) is employed to run numerical models using cure-extent dependent viscoelasticity.

7.6.1. Cure extent (p) – Thermal (T) analogy

At any given instant for a cure temperature (T_c) and cure-extent (p), the total amount of horizontal shifting ($\log(a_{Total})$) is determined by addition of two-factors - (1) the temperature-shift factor ($\log(a_T)$) associated with the difference between cure temperature (T_c) and the reference temperature (T_{ref}) and, (2) the cure-dependent shift factor (a_p) associated with the cure-extent at the specific time:

$$\log a_{Total} = \log a_T\left(T_c - T_{ref}\right) + \log a_p(p) \tag{109}$$

For a constant cure temperature (T_c), the term $\log a_T(T_c - T_{ref})$ is fixed and the term $\log a_p(p)$ changes as the curing occurs.

A field variable (p) can be defined in the FEM program which will track the cure extent over time. Alternately, an analogy can be made between the cure-extent (p) and temperature (T) to relate the cure-dependent shift factors ($\log a_p$) to the temperature-dependent shift factors ($\log a_T$).

A pseudo-temperature variable ($T_{fictive}$) is defined to determine the shift-factor for a given T_c and p:

$$T_{fictive} = T_c - T_g(p) \tag{110}$$

The reason for choosing $T_g(p)$ as parameter in $T_{fictive}$ is that $T_g(p)$ is directly related to the cure-extent (p) through the DiBenedetto equation determined in Eq. (97). Using the complete cure kinetics function form Eq. (104) combined with the $T_g(p)$, the evolution of $T_{fictive}$ as a function of time can be determined for a fixed T_c as:

$$T_{fictive}(t) = T_c - T_g(p(t)) \tag{111}$$

The curing reaction can be simulated as temperature change (thermal condition) in the commercial FEM solver.

Since both $T_{fictive}$ and $\log a_p$ have unique values for a given cure extent (p) and cure-temperature (T_c), an analogy can be established. A pseudo-temperature ($T_{fictive}$) based shift-factor table can be defined for a given p as:

$$[T, \log a_T] \rightarrow [p, \log a_p] \rightarrow [T_{fictive}, \log a_{T_{fictive}}] \tag{112}$$

7.6.1.1. Cure-dependent viscoelastic master curves - $\boldsymbol{G(t,p)}$ and $\boldsymbol{K(t,p)}$

Unlike traditional LVE, in cure-dependent viscoelasticity, the equilibrium moduli - $G_\infty(p)$ and $K_\infty(p)$ evolve at each time-step as curing occurs. Thus, the mathematical functional forms need to be included in the model. For current implementation, a tool called look-up table was utilized.

Master curves (Prony series) as a function of cure-extent were defined at various degrees of cure ($\Delta p = 0.01$) beyond the gel-point (p_{gel}) and input into the look-up tables for the model. The solver would refer to the look-up tables for the appropriate master curve based on the value of $T_{fictive}$ at a specific time-step in the run.

Based on the above modifications, we can now run a cure-dependent viscoelastic model at a given cure temperature (T_c). In the next section, the modified FEM solver will be checked using a virtual stress relaxation experiment.

7.6.2. Comparison of relaxation behavior at various cure extents with analytical solution

It is important to confirm that model gives accurate results for various cure extents (p) during the implementation of cure extent (p) – Thermal (T) analogy. A virtual stress relaxation experiment is conducted to compare the results with the FEM output.

An instantaneous uniaxial and hydrostatic strain ($100\ \mu\varepsilon$) were used and the stress relaxation behavior was calculated as a function of time. The results of the virtual experiment are shown in Figure 96 for two representative cure-extent – (a) $p = 0.9$ and (b) $p = 0.7$, respectively. The results of analytical solution match well with the FEM results, which corroborates that the cure (p) – thermal (T) has been implemented properly.

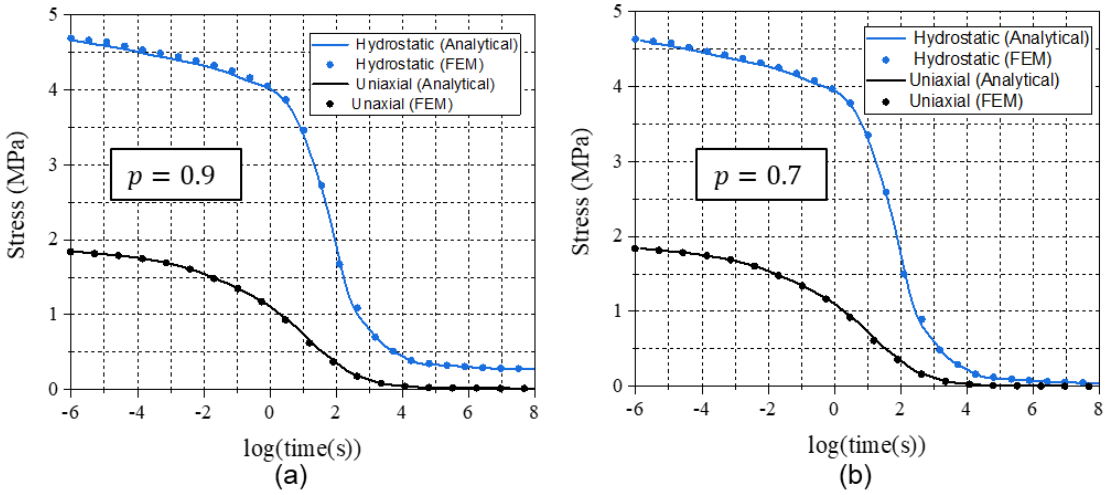


Figure 96 Comparison of stress relaxation results obtained from FEM vs. analytical solution – (a)$p = 0.9$, and (b) $p = 0.7$

7.6.3. Mold process simulation using a TFBGA package

A thin fine-pitch ball grid array (TFBGA) package was used to simulate mold process conditions at 165°C. A schematic of the TFBGA package used in the model is shown in Figure 97. It consists of two stacked dies of 50 μm thickness with a die attach film of 20 μm. The substrate and EMC thicknesses are 100 μm and 450 μm, respectively.

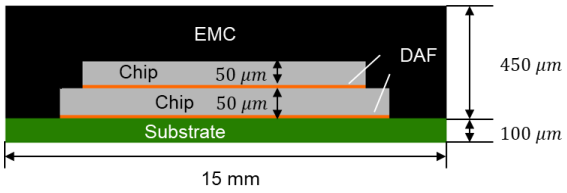


Figure 97 Schematic of a TFBGA package used in the FEM model

For the FEM model it was assumed that all materials except EMC have isotropic elastic properties. The mechanical properties of the materials in the package are summarized in Table 7.

Table 7 Summary table for the material properties (other than EMC)

Material	E (GPa)	ν	K (GPa)
Chip	130	0.23	80.25
Die-attach film (DAF)	0.008	0.3	0.006
Substrate	7.5	0.30	6.25

A schematic of a pressure profile applied is shown in Figure 98. The mold pressure was applied for 60 seconds (1 minute) and demolded. It was held under post mold conditions for 9 minutes to predict how the warpage will evolve over time. A curing profile (beyond gel point) was simulated at 165°C which is in the range of typical molding temperatures.

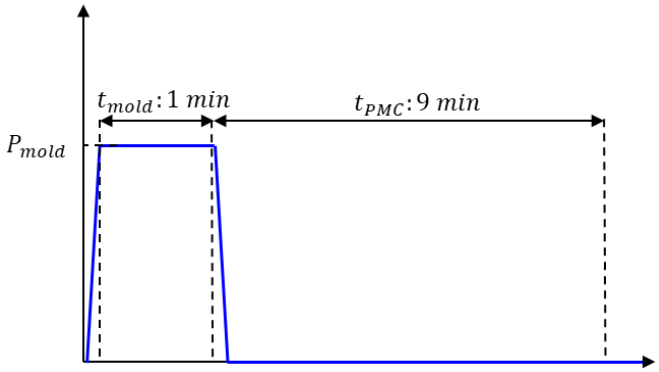


Figure 98 Mold pressure profile used in the FEM model

The model was run assuming quarter symmetry conditions. A schematic for the boundary conditions applied is shown in Figure 99 (a). The boundary conditions shown in the schematic were applied during the molding process. The edges are under roller conditions due to presence of mold walls. After molding process is finished, all edges are set to "free" in the model to simulate demold conditions (traction free on all sides). The meshed model is shown in Figure 99 (b)

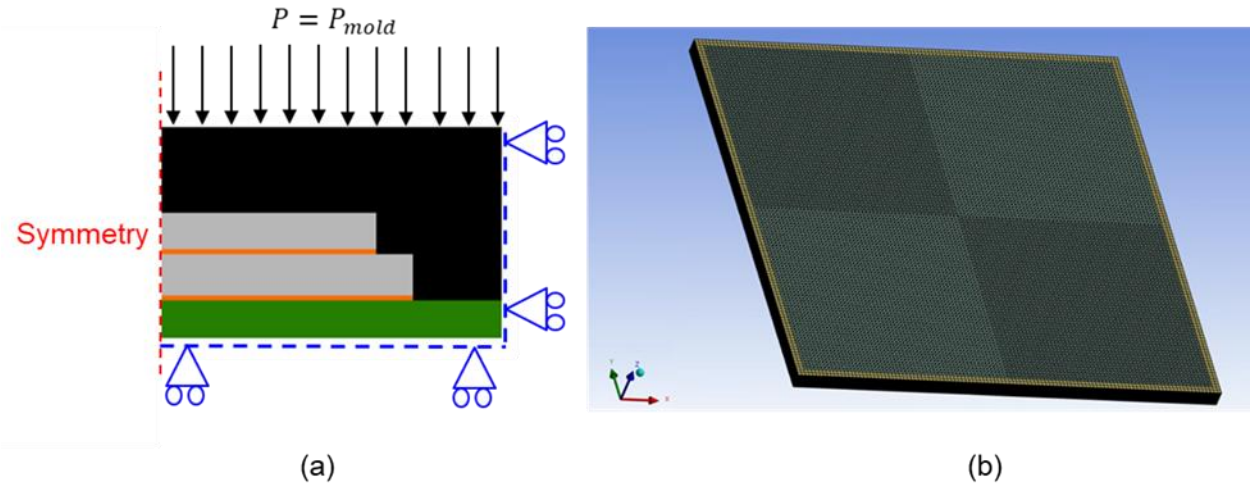


Figure 99 Model conditions - (a)Boundary conditions applied on the model and (b) Meshed model

The results of the model for mold pressure of 1 MPa (red plot) and 7 MPa (black plot) are shown in Figure 100. Initially for the first 60 seconds, when the mold pressure is being applied,

the package is inside the mold and there is no warpage. The entire package is under near hydrostatic compression due to the pressure applied from the top and the roller conditions at the edges.

There is an instantaneous elastic recovery at the instant of demolding which is indicated by a sudden jump in warpage. After the initial jump, the EMC continues to cure upto ~250 seconds at which point the curing has completed. The EMC warpage continues to change beyond that point for over 300 seconds due to viscoelastic behavior.

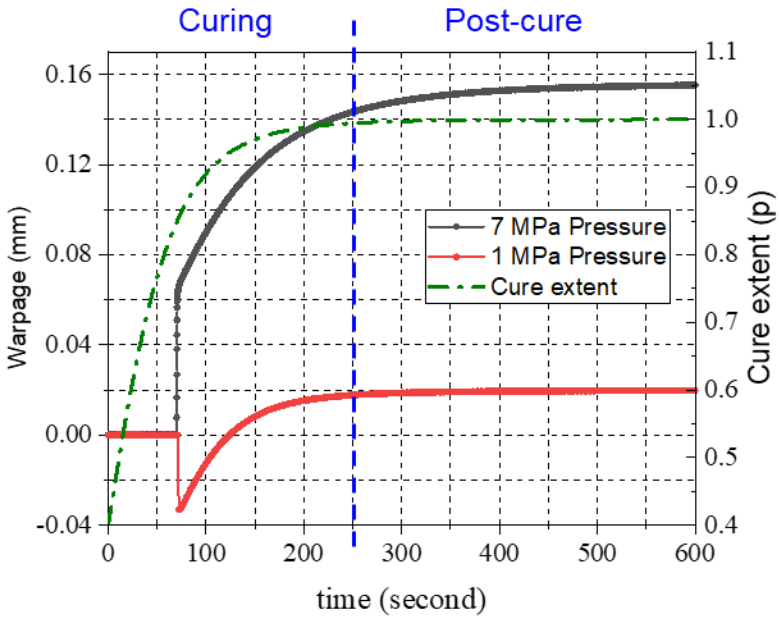


Figure 100 Warpage of the TFBGA package during and after molding process

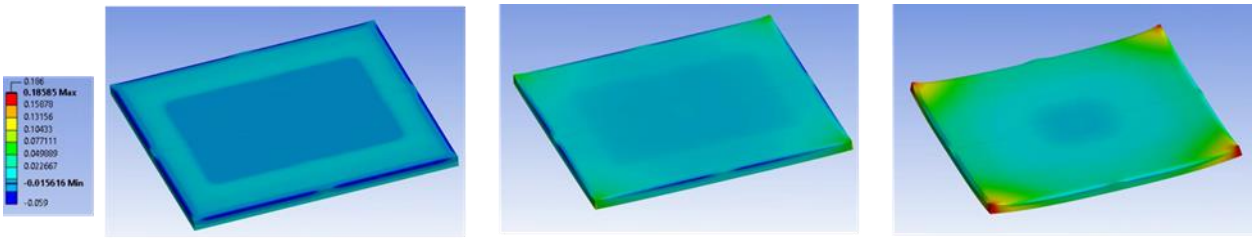
It is worth noting that at the moment of instantaneous recovery, the package exhibits vastly different warpages - crying warpage for 1 MPa pressure and a smiling warpage for 7 MPa pressure. Both chip and substrate undergo deformation during the molding stage.

The chip when compressed from top will expand in the xy-direction nearly freely as EMC modulus is much lower during curing compared to the chip. Upon removal of pressure, the chip will try to shrink back in the xy-direction.

The substrate is not allowed to expand in the xy- direction during molding stage and will undergo purely volumetric deformation due to the near hydrostatic pressure conditions. Once, the pressure is removed, the substrate will expand in all directions. Because of the bulk modulus of the substrate, the volumetric deformation at 1 MPa and 7 MPa pressures will be about 18 μm and 130 μm, respectively. The amount of expansion is vastly different and combined with the effect of chip and EMC is speculated to contribute to the crying and smiling warpages, respectively for the two levels of pressure.

The EMC will also expand significantly due to the built-up strains once the pressure is removed. The EMC will continue to relax over time which causes increase of warpage over time. In both cases, the final warpage will be governed by the equilibrium stresses in the EMC.

Warpage at various stages for 7 MPa molding conditions are shown in Figure 100. (a) shows the z- deformations just before demolding, (b) shows warpage just after demolding which causes a sudden jump due to elastic recovery and (c) is the warpage at 600 seconds when the EMC has relaxed and is fully-cured.



(a) (b) (c)

Figure 101 Warpage at various stages during and after molding processes – (a) Before demolding – 0 μm, (b) just after demolding – 50 μm, and (c) after complete relaxation (600 seconds) – 155 μm.

Chapter 8 Thesis Contributions and Future Work

8.1. Thesis Contributions

The cure-dependent viscoelastic properties of epoxy molding compound (EMC) for the warpage and residual stress prediction in microelectronics packaging were characterized by the novel experimental/numerical tools and procedures. The most significant contributions made in this dissertation are:

1) A new deterministic approach to obtain autocatalytic cure kinetics model constants was developed to determine cure-kinetics of thermosets like EMC. To the best knowledge of the author, an analytical solution to a KS based autocatalytic model is not available in the literature. This technique will allow a packaging engineer to quickly characterize cure kinetics of polymers using simple spreadsheet softwares. This chapter also gives a guideline on minimum number of measurements required to be able to accurately quantify cure kinetics.
2) A novel method was developed to quantify autocatalytic cure kinetics of advanced thermosets with dual-reaction systems. The procedure utilizes non-linear regression tools combined with appropriate methodology to determine initial guess values to obtain model constants for dual-reaction thermosets with minimum data set. To the best knowledge of the author, current literature utilizes large amount of DSC test data to obtain model constants. However, inspite of this, the global minima solution is not guaranteed. This will help packaging engineers to quickly quantify the curing behavior of advanced thermosets which are being introduced in packaging industries to tailor material properties.

3) A test methodology has been developed to quantify viscoelastic bulk behavior of thermosets using hydrostatic testing. The methodology combines the advantage of direct strain measurement along with constitutive equations of LVE to determine master curves (Prony series) of bulk modulus directly from the time-dependent pressure and strain data. Use of low rate linear loading also mitigates the issues associated with heat generation when using gas as a pressurization medium.
4) A novel test procedure was proposed and implemented to measure equilibrium moduli - $E_\infty(p)$ and $K_\infty(p)$ of EMC as a function of cure-extent. It has been particularly challenging to measure equilibrium moduli due to large viscoelasticity and high curing rate of EMC in the equilibrium region. An evolution model based on percolation theory was fit to the experimental dataset. To the best author's knowledge, this is the first time, $E_\infty(p)$ and $K_\infty(p)$ have been characterized for a filled thermoset material. These properties are critical to describe cure-dependent behavior of EMC.
5) The assumption of time-cure superposition (TCS) was shown to work for the EMC by determining viscoelastic Young's moduli behavior for partially-cured EMC specimens. Several MFT sweeping experiments were conducted on partially-cured EMC at temperature below $T_g(p)$ of the material to determine sections of master curves. It was ensured that the EMC is in a near isocure state by limiting the amount of curing using the diffusion-controlled model. Appropriate temperatures were chosen such that the cumulative total amount of EMC curing was ~1%. The partially-cured data was normalized and horizontally shifted to determine cure-dependent shift factors ($\log a_p$).

6) An FEM model was developed to utilize the measured cure-dependent viscoelastic properties using TCS to be able to predict stress/warpages at a constant cure temperature (T_c) during and after molding process.

8.2. Future Work

1) **Tailoring mold process for warpage "design"**

   The measured cure-dependent viscoelastic properties can be used in real world mold process applications (specifically compression molding) to design the warpage of packages by controlling the process parameters such as time, temperature and pressure for molding.

2) **Additional work on FEM model for general loading conditions (non-isothermal)**

   More work on the FEM model needs to be done such that it can predict mechanical behavior for non-isothermal temperature while combining viscoelastic effects associated with curing.

3) **Measurement of additional viscoelastic properties - $G(t)$ and $\nu(t)$**

   Measurement of additional viscoelastic properties like - $G(t)$ and/or $\nu(t)$ to validate the accuracy of interconversion tools and the measured properties.

4) **Validation of the measurement properties using an inline warpage measurement tool**

   The warpage generated by transfer/compression molding process is measured using an inline-warpage measurement tool. This measurement in combination with the

FEM program developed can be used to validate the accuracy for the measured cure-dependent viscoelastic properties.

Appendix

A-1 First-order and second-order optimality criterion for a system of linear equations.

A system of equations with N variables and M number of data points such that $M \geq N$ can be expressed as follows [90]:

$$\begin{pmatrix} y_1 \\ \vdots \\ y_m \end{pmatrix} = \begin{bmatrix} x_{1,1} & \cdots & x_{n,1} \\ \vdots & \ddots & \vdots \\ x_{n,m} & \cdots & x_{n,m} \end{bmatrix} \begin{pmatrix} C_1 \\ \vdots \\ C_n \end{pmatrix} \tag{113}$$

For determining the constants - $C_1, C_2, \ldots, C_n$ using the experimentally obtained data, an objective function based on least squares method is defined:

$$\begin{gathered} S = \sum_{i=1}^{M} \left(y_{i,exp} - y_{i,pred}\right)^2 \\ S = \sum_{i=1}^{M} \left(y_{i,exp} - C_1 x_{1,i} - C_2 x_{2,i} \ldots . - C_n x_{n,i}\right)^2 \end{gathered} \tag{114}$$

To obtain an optimum set of constants, the function S needs to be minimized, i.e, ∇S=0

$$\begin{gathered} \frac{\partial S}{\partial C_1} = \frac{\partial S}{\partial C_2} = \cdots \frac{\partial S}{\partial C_n} = 0 \\ \frac{\partial S}{\partial C_j} = 0 = 2 \sum_{i=1}^{M} \left(y_{i,exp} - \sum_{j=1}^{N} C_j x_{j,i} \right) - x_{j,i} \end{gathered} \tag{115}$$

For the extrema to be a minimum, the Hessian of the function should be a positive-definite matrix. The Hessian (H) of the function can be calculated as follows:

$$H = \begin{pmatrix} \frac{\partial^2 S}{\partial C_1^2} & \cdots & \frac{\partial^2 S}{\partial C_1 \partial C_n} \\ \vdots & \ddots & \vdots \\ \frac{\partial^2 S}{\partial C_n \partial C_1} & \cdots & \frac{\partial^2 S}{\partial C_n^2} \end{pmatrix}$$

$$H = \begin{pmatrix} 2\sum_{i=1}^{M} x_{1,i}^2 & \cdots & 2\sum_{i=1}^{M} x_{1,i} x_{N,i} \\ \vdots & \ddots & \vdots \\ 2\sum_{i=1}^{M} x_{1,i} x_{N,i} & \cdots & 2\sum_{i=1}^{M} x_{N,i}^2 \end{pmatrix} \tag{116}$$

Here the Hessian matrix is symmetric with all pivots having positive values (squared). Hence, the Hessian is positive definite and the stationary point is a minimum. Since the system of equations is linear, a single solution satisfies the first-order criterion and is a global minimum.

References

[1] M. Brunnbauer *et al.*, "An embedded device technology based on a molded reconfigured wafer," in *56th Electronic Components and Technology Conference 2006*, 2006: IEEE, p. 5 pp.

[2] Y. Kurita *et al.*, "Fan-Out Wafer-Level Packaging with highly flexible design capabilities," in *3rd Electronics System Integration Technology Conference ESTC*, 2010: IEEE, pp. 1-6.

[3] T. Braun *et al.*, "Through mold via technology for multi-sensor stacking," in *2012 IEEE 14th Electronics Packaging Technology Conference (EPTC)*, 2012: IEEE, pp. 316-321.

[4] C. C. Liu *et al.*, "High-performance integrated fan-out wafer level packaging (InFO-WLP): Technology and system integration," in *2012 International Electron Devices Meeting*, 2012: IEEE, pp. 14.1. 1-14.1. 4.

[5] H.-W. Liu *et al.*, "Warpage characterization of panel fan-out (P-FO) package," in *2014 IEEE 64th Electronic Components and Technology Conference (ECTC)*, 2014: IEEE, pp. 1750-1754.

[6] T. Takahashi *et al.*, "A new embedded die package—WFOP™," in *Proceedings of the 5th Electronics System-integration Technology Conference (ESTC)*, 2014: IEEE, pp. 1-5.

[7] B. Han, Y. Guo, C. Lim, and D. Caletka, "Verification of numerical models used in microelectronics packaging design by interferometric displacement measurement methods," 1996.

[8] B. Wu, D.-S. Kim, B. Han, A. Palczynska, A. Prisacaru, and P. J. Gromala, "Hybrid approach to conduct failure prognostics of automotive electronic control unit using stress sensor as in situ load counter," *IEEE Transactions on Components, Packaging and Manufacturing Technology*, vol. 9, no. 1, pp. 28-38, 2018.

[9] M. Amagai and Y. Suzuki, "A study of package warpage for package on package (PoP)," in *2010 Proceedings 60th Electronic Components and Technology Conference (ECTC)*, 2010: IEEE, pp. 226-233.

[10] P.-Y. Lin and S. Lee, "Warpage modeling of ultra-thin packages based on chemical shrinkage and cure-dependent viscoelasticity of molded underfill," *IEEE Transactions on Device and Materials Reliability*, vol. 20, no. 1, pp. 67-73, 2019.

[11] J. M. Kenny, "Determination of autocatalytic kinetic model parameters describing thermoset cure," *Journal of Applied Polymer Science*, vol. 51, no. 4, pp. 761-764, 1994.

[12] S.-J. Hwang and Y.-S. Chang, "PVTC equation for epoxy molding compound," *IEEE Transactions on components and packaging technologies*, vol. 29, no. 1, pp. 112-117, 2006.

[13] Y.-J. Lin, S.-J. Hwang, H.-H. Lee, and D.-Y. Huang, "Modeling of viscoelastic behavior of an epoxy molding compound during and after curing," *IEEE Transactions on Components, Packaging and Manufacturing Technology*, vol. 1, no. 11, pp. 1755-1760, 2011.

[14] M. Sadeghinia, K. M. Jansen, and L. J. Ernst, "Characterization of the viscoelastic properties of an epoxy molding compound during cure," *Microelectronics Reliability*, vol. 52, no. 8, pp. 1711-1718, 2012.

[15] J. D. Russell, "Cure shrinkage of thermoset composites," *SAMPE Quarterly (Society of Aerospace Material and Process Engineers);(United States)*, vol. 24, no. 2, 1993.

[16] J. Lange, S. Toll, J.-A. E. Månson, and A. Hult, "Residual stress build-up in thermoset films cured above their ultimate glass transition temperature," *Polymer,* vol. 36, no. 16, pp. 3135-3141, 1995.
[17] V. Fano, I. Ortalli, S. Pizzi, and M. Bonanini, "Polymerization shrinkage of microfilled composites determined by laser beam scanning," *Biomaterials,* vol. 18, no. 6, pp. 467-470, 1997.
[18] W. D. Cook, M. Forrest, and A. A. Goodwin, "A simple method for the measurement of polymerization shrinkage in dental composites," *Dental Materials,* vol. 15, no. 6, pp. 447-449, 1999.
[19] C. Li, K. Potter, M. R. Wisnom, and G. Stringer, "In-situ measurement of chemical shrinkage of MY750 epoxy resin by a novel gravimetric method," *Composites Science and Technology,* vol. 64, no. 1, pp. 55-64, 2004.
[20] H. Yu, S. Mhaisalkar, and E. Wong, "Cure shrinkage measurement of nonconductive adhesives by means of a thermomechanical analyzer," *Journal of electronic materials,* vol. 34, no. 8, pp. 1177-1182, 2005.
[21] D. U. Shah and P. J. Schubel, "Evaluation of cure shrinkage measurement techniques for thermosetting resins," *Polymer Testing,* vol. 29, no. 6, pp. 629-639, 2010.
[22] Y. Nawab, P. Casari, N. Boyard, and F. Jacquemin, "Characterization of the cure shrinkage, reaction kinetics, bulk modulus and thermal conductivity of thermoset resin from a single experiment," *Journal of Materials Science,* vol. 48, no. 6, pp. 2394-2403, 2013.
[23] Y. Wang, L. Woodworth, and B. Han, "Simultaneous measurement of effective chemical shrinkage and modulus evolutions during polymerization," *Experimental mechanics,* vol. 51, no. 7, pp. 1155-1169, 2011.
[24] Y. Sun, B. Han, E. Parsa, and A. Dasgupta, "Measurement of effective chemical shrinkage and equilibrium modulus of silicone elastomer used in potted electronic system," *Journal of materials science,* vol. 49, no. 24, pp. 8301-8310, 2014.
[25] S. P. Phansalkar, C. Kim, B. Han, and P. J. Gromala, "Volumetric effective cure shrinkage measurement of dual curable adhesives by fiber Bragg grating sensor," *Journal of materials science,* vol. 55, no. 22, pp. 9655-9664, 2020.
[26] A. Maxwell, W. Broughton, and M. Lodeiro, "Review of techniques for the characterisation of residual stress in polymer composites," 2006.
[27] P. P. Parlevliet, H. E. Bersee, and A. Beukers, "Residual stresses in thermoplastic composites—A study of the literature—Part II: Experimental techniques," *Composites Part A: Applied Science and Manufacturing,* vol. 38, no. 3, pp. 651-665, 2007.
[28] I. Baran, K. Cinar, N. Ersoy, R. Akkerman, and J. H. Hattel, "A review on the mechanical modeling of composite manufacturing processes," *Archives of computational methods in engineering,* vol. 24, no. 2, pp. 365-395, 2017.
[29] C. Kim, S. P. Phansalkar, H.-S. Lee, and B. Han, "Measurement of effective cure shrinkage of epoxy-based molding compound by fiber Bragg grating sensor using two-stage curing process," *Journal of Applied Polymer Science,* vol. n/a, no. n/a, p. 51620, 2021, doi: https://doi.org/10.1002/app.51620.
[30] *Standard Test Method for Measuring Shrinkage from Mold Dimensions of Molded Thermosetting Plastics,* ASTM, 2013.
[31] C. Kim, S. Phansalkar, H.-S. Lee, and B. Han, "On Curing-Induced Residual Stresses After Molding Processes: Mold Shrinkage, Chemical Shrinkage or Both?," in *2019 IEEE 69th Electronic Components and Technology Conference (ECTC),* 2019: IEEE, pp. 1382-1386.

[32] F. Goffreda, A. Griff, L. Livinghouse, T. Walsh, and J. Scuralli, "Tool and Manufacturing Engineers Handbook Knowledge Base," *Society of Manufacturing Engineers,* 1998.
[33] F. Hou *et al.*, "Experimental verification and optimization analysis of warpage for panel-level fan-out package," *IEEE Transactions on Components, Packaging and Manufacturing Technology,* vol. 7, no. 10, pp. 1721-1728, 2017.
[34] P. Chen, Z. Ji, Y. Liu, C. Wu, N. Ye, and H. Takiar, "Warpage prediction methodology of extremely thin package," in *2017 IEEE 67th Electronic Components and Technology Conference (ECTC)*, 2017: IEEE, pp. 2080-2085.
[35] F. X. Che, M. Kawano, M. Z. Ding, Y. Han, and S. Bhattacharya, "Study on low warpage and high reliability for large package using TSV-free interposer technology through SMART codesign modeling," *IEEE Transactions on Components, Packaging and Manufacturing Technology,* vol. 7, no. 11, pp. 1774-1785, 2017.
[36] C. Arayama, T. Akashi, Y. Tomita, and N. Kanagawa, "Method for Mitigating the Warpage of Ultra-Thin FC-CSPs by Controlling of EMC Properties," in *2019 IEEE 69th Electronic Components and Technology Conference (ECTC)*, 2019: IEEE, pp. 1022-1027.
[37] J. De Vreugd *et al.*, "Advanced viscoelastic material model for predicting warpage of a QFN panel," in *2008 58th Electronic Components and Technology Conference*, 2008: IEEE, pp. 1635-1640.
[38] S.-S. Yeh *et al.*, "Warpage modeling and characterization of the viscoelastic relaxation for cured molding process in fan-out packages," in *2017 IEEE 67th Electronic Components and Technology Conference (ECTC)*, 2017: IEEE, pp. 841-846.
[39] Z. Chen *et al.*, "Package level warpage simulation of fan-out wafer level package (FOWLP) considering viscoelastic material properties," in *2018 IEEE 20th Electronics Packaging Technology Conference (EPTC)*, 2018: IEEE, pp. 836-842.
[40] Z. Chen *et al.*, "Wafer Level Warpage Modelling and Validation for FOWLP Considering Effects of Viscoelastic Material Properties under Process Loadings," in *2019 IEEE 69th Electronic Components and Technology Conference (ECTC)*, 2019: IEEE, pp. 1543-1549.
[41] A. V. Amirkhizi, J. Isaacs, J. McGee, and S. Nemat-Nasser, "An experimentally-based viscoelastic constitutive model for polyurea, including pressure and temperature effects," *Philosophical magazine,* vol. 86, no. 36, pp. 5847-5866, 2006.
[42] N. W. Tschoegl, W. G. Knauss, and I. Emri, "Poisson's ratio in linear viscoelasticity–a critical review," *Mechanics of Time-Dependent Materials,* vol. 6, no. 1, pp. 3-51, 2002.
[43] R. Schapery and S. Park, "Methods of interconversion between linear viscoelastic material functions. Part II—an approximate analytical method," *International Journal of Solids and Structures,* vol. 36, no. 11, pp. 1677-1699, 1999.
[44] S. Park and R. Schapery, "Methods of interconversion between linear viscoelastic material functions. Part I—A numerical method based on Prony series," *International journal of solids and structures,* vol. 36, no. 11, pp. 1653-1675, 1999.
[45] M. L. Williams, R. F. Landel, and J. D. Ferry, "The temperature dependence of relaxation mechanisms in amorphous polymers and other glass-forming liquids," *Journal of the American Chemical society,* vol. 77, no. 14, pp. 3701-3707, 1955.
[46] Q. Xu and B. Engquist, "A mathematical model for fitting and predicting relaxation modulus and simulating viscoelastic responses," *Proceedings of the Royal Society A: Mathematical, Physical and Engineering Sciences,* vol. 474, no. 2213, p. 20170540, 2018.

[47] V. Kamath and M. Mackley, "The determination of polymer relaxation moduli and memory functions using integral transforms," *Journal of non-newtonian fluid mechanics,* vol. 32, no. 2, pp. 119-144, 1989.
[48] K. Jansen, "Thermomechanical modeling and characterization of polymers," *course book, TU Delft,* 2007.
[49] J. De Vreugd, K. M. Jansen, L. J. Ernst, and C. Bohm, "Prediction of cure induced warpage of micro-electronic products," *Microelectronics Reliability,* vol. 50, no. 7, pp. 910-916, 2010.
[50] R. W. Chan and M. L. Rodriguez, "A simple-shear rheometer for linear viscoelastic characterization of vocal fold tissues at phonatory frequencies," *The Journal of the Acoustical Society of America,* vol. 124, no. 2, pp. 1207-1219, 2008.
[51] N. Nakajima, E. Harrell, and E. Collins, "Viscoelastic Characterization of Ethylene-Propylene-Diene Terpolymer Elastomers," *Rubber Chemistry and Technology,* vol. 50, no. 1, pp. 99-108, 1977.
[52] S. Imaoka, "Analyzing viscoelastic materials," *Ansys Advantage,* vol. 2, no. 4, pp. 46-47, 2008.
[53] D.-L. Chen, P.-F. Yang, and Y.-S. Lai, "A review of three-dimensional viscoelastic models with an application to viscoelasticity characterization using nanoindentation," *Microelectronics Reliability,* vol. 52, no. 3, pp. 541-558, 2012.
[54] S.-S. Yeh *et al.*, "Fan-out wafer molding process optimization using cure-dependent viscoelastic modeling and characterizations," in *2017 12th International Microsystems, Packaging, Assembly and Circuits Technology Conference (IMPACT)*, 2017: IEEE, pp. 148-151.
[55] P. Gromala, "Private Discussion with P. Gromala," ed, 2021.
[56] I. Emri and T. Prodan, "A measuring system for bulk and shear characterization of polymers," *Experimental mechanics,* vol. 46, no. 4, pp. 429-439, 2006.
[57] M. Sadeghinia, K. Jansen, and L. Ernst, "Characterization and modeling the thermo-mechanical cure-dependent properties of epoxy molding compound," *International Journal of Adhesion and Adhesives,* vol. 32, pp. 82-88, 2012.
[58] Y. Sun, H.-S. Lee, and B. Han, "Measurement of elastic properties of epoxy molding compound by single cylindrical configuration with embedded fiber Bragg grating sensor," *Experimental mechanics,* vol. 57, no. 2, pp. 313-324, 2017.
[59] H. S. Lee, Y. Sun, C. Kim, and B. Han, "Characterization of Linear Viscoelastic Behavior of Epoxy Molding Compound Subjected to Uniaxial Compression and Hydrostatic Pressure," *IEEE Transactions on Components, Packaging and Manufacturing Technology,* vol. 8, no. 8, pp. 1363-1372, 2018.
[60] H. S. Lee, B. Han, and P. Gromala, "Effect of Time-Dependent Bulk Modulus on Reliability Assessment of Automotive Electronic Control Unit," in *2019 IEEE 69th Electronic Components and Technology Conference (ECTC)*, 2019: IEEE, pp. 1529-1534.
[61] H. Lee, S. Phansalkar, and B. Han, "Constant Poisson's Ratio of Thermosetting Polymers: Is It Reasonable for Accurate Thermal Stress Analysis?," in *2020 IEEE 70th Electronic Components and Technology Conference (ECTC)*, 2020: IEEE, pp. 2092-2096.
[62] J. E. Martin and D. Adolf, "Constitutive equation for cure-induced stresses in a viscoelastic material," *Macromolecules,* vol. 23, no. 23, pp. 5014-5019, 1990.

[63] D. J. Plazek and I. C. Chay, "The evolution of the viscoelastic retardation spectrum during the development of an epoxy resin network," *Journal of Polymer Science Part B: Polymer Physics,* vol. 29, no. 1, pp. 17-29, 1991.
[64] W. H. Stockmayer, "Theory of molecular size distribution and gel formation in branched polymers II. General cross linking," *The Journal of Chemical Physics,* vol. 12, no. 4, pp. 125-131, 1944.
[65] D. Stauffer, "gIntroduction to Percolation Theory,• hTaylor & Francis," *London and Philadelphia,* 1985.
[66] S. L. Simon, G. B. Mckenna, and O. Sindt, "Modeling the evolution of the dynamic mechanical properties of a commercial epoxy during cure after gelation," *Journal of Applied Polymer Science,* vol. 76, no. 4, pp. 495-508, 2000.
[67] V. Antonucci, A. Cusano, M. Giordano, J. Nasser, and L. Nicolais, "Cure-induced residual strain build-up in a thermoset resin," *Composites Part A: Applied Science and Manufacturing,* vol. 37, no. 4, pp. 592-601, 2006.
[68] J.-F. Larché, P.-O. Bussière, P. Wong-Wah-Chung, and J.-L. Gardette, "Chemical structure evolution of acrylic-melamine thermoset upon photo-ageing," *European polymer journal,* vol. 48, no. 1, pp. 172-182, 2012.
[69] S. Saseendran, M. Wysocki, and J. Varna, "Evolution of viscoelastic behaviour of a curing LY5052 epoxy resin in the rubbery state," *Advanced Composite Materials,* vol. 26, no. 6, pp. 553-567, 2017.
[70] D. B. Adolf, J. E. Martin, R. S. Chambers, S. N. Burchett, and T. R. Guess, "Stresses during thermoset cure," *Journal of materials research,* vol. 13, no. 3, pp. 530-550, 1998.
[71] D. Adolf and J. E. Martin, "Time-cure superposition during crosslinking," *Macromolecules,* vol. 23, no. 15, pp. 3700-3704, 1990.
[72] J. Lange, J.-A. E. Månson, and A. Hult, "Build-up of structure and viscoelastic properties in epoxy and acrylate resins cured below their ultimate glass transition temperature," *Polymer,* vol. 37, no. 26, pp. 5859-5868, 1996.
[73] Y. Eom, L. Boogh, V. Michaud, P. Sunderland, and J. A. Månson, "Time-cure-temperature superposition for the prediction of instantaneous viscoelastic properties during cure," *Polymer Engineering & Science,* vol. 40, no. 6, pp. 1281-1292, 2000.
[74] D.-G. Yang *et al.*, "Numerical modeling of warpage induced in QFN array molding process," *Microelectronics Reliability,* vol. 47, no. 2-3, pp. 310-318, 2007.
[75] T. Falat, K. Jansen, J. De Vreugd, and S. Rzepka, "Influence of cure dependency of molding compound properties on warpage and stress distribution during and after the encapsulation of electronics components," in *EuroSimE 2009-10th International Conference on Thermal, Mechanical and Multi-Physics Simulation and Experiments in Microelectronics and Microsystems*, 2009: IEEE, pp. 1-6.
[76] S. Saseendran, M. Wysocki, and J. Varna, "Cure-state dependent viscoelastic Poisson's ratio of LY5052 epoxy resin," *Advanced Manufacturing: Polymer & Composites Science,* vol. 3, no. 3, pp. 92-100, 2017.
[77] L. J. Ernst, G. Q. Zhang, K. M. B. Jansen, and H. J. L. Bressers, "Time- and Temperature-Dependent Thermo-Mechanical Modeling of a Packaging Molding Compound and its Effect on Packaging Process Stresses," *Journal of Electronic Packaging,* vol. 125, no. 4, pp. 539-548, 2003, doi: 10.1115/1.1604156.
[78] E. Suhir, Y.-C. Lee, and C. Wong, *Micro-and opto-electronic materials and structures: physics, mechanics, design, reliability, packaging: Volume I Materials physics-materials*

mechanics. Volume II Physical design-reliability and packaging. Springer Science & Business Media, 2007.
[79] K. M. Jansen *et al.*, "Modeling and characterization of molding compound properties during cure," *Microelectronics Reliability*, vol. 49, no. 8, pp. 872-876, 2009.
[80] S. Saseendran, M. Wysocki, and J. Varna, "Evolution of viscoelastic behavior of a curing LY5052 epoxy resin in the glassy state," *Advanced Manufacturing: Polymer & Composites Science*, vol. 2, no. 2, pp. 74-82, 2016.
[81] H. J. Borchardt and F. Daniels, "The application of differential thermal analysis to the study of reaction kinetics1," *Journal of the American Chemical Society*, vol. 79, no. 1, pp. 41-46, 1957.
[82] *Standard Test Method for Estimating Kinetic Parameters by Differential Scanning Calorimeter Using the Borchardt and Daniels Method*, I. ASTM, 2018.
[83] S. P. Phansalkar, C. Kim, and B. Han, "Effect of critical properties of epoxy molding compound on warpage prediction: A critical review," *Microelectronics Reliability*, vol. 130, p. 114480, 2022.
[84] J. H. Lau, *Semiconductor advanced packaging*. Springer Nature, 2021.
[85] P. I. Karkanas and I. K. Partridge, "Cure modeling and monitoring of epoxy/amine resin systems. I. Cure kinetics modeling," *Journal of applied polymer science*, vol. 77, no. 7, pp. 1419-1431, 2000.
[86] R. Tao, S. P. Phansalkar, A. M. Forster, and B. Han, "Investigation of Cure Kinetics of Advanced Epoxy Molding Compound Using Dynamic Heating Scan: An Overlooked Second Reaction," in *2023 IEEE 73rd Electronic Components and Technology Conference (ECTC)*, 2023: IEEE, pp. 1319-1326.
[87] C.-C. Lee, C.-C. Lee, and C.-P. Chang, "Simulation methodology development of warpage estimation for epoxy molding compound under considerations of stress relaxation characteristics and curing conditions applied in semiconductor packaging," *Materials Science in Semiconductor Processing*, vol. 145, p. 106637, 2022.
[88] J. Hu, J. Shan, D. Wen, X. Liu, J. Zhao, and Z. Tong, "Flame retardant, mechanical properties and curing kinetics of DOPO-based epoxy resins," *Polymer degradation and stability*, vol. 109, pp. 218-225, 2014.
[89] M. Kamal and S. Sourour, "Kinetics and thermal characterization of thermoset cure," *Polymer Engineering & Science*, vol. 13, no. 1, pp. 59-64, 1973.
[90] P. Y. Papalambros and D. J. Wilde, *Principles of optimal design: modeling and computation*. Cambridge university press, 2000.
[91] Z. Wang, J. Cardenas-Garcia, and B. Han, "Inverse method to determine elastic constants using a circular disk and moiré interferometry," *Experimental mechanics*, vol. 45, pp. 27-34, 2005.
[92] Z. Lu, R. D. Monteiro, and M. Yuan, "Convex optimization methods for dimension reduction and coefficient estimation in multivariate linear regression," *Mathematical Programming*, vol. 131, no. 1-2, pp. 163-194, 2012.
[93] J. M. Barton, "The application of differential scanning calorimetry (DSC) to the study of epoxy resin curing reactions," in *Epoxy resins and composites I*: Springer, 2005, pp. 111-154.
[94] D. Roşu, C. Caşcaval, F. Mustață, and C. Ciobanu, "Cure kinetics of epoxy resins studied by non-isothermal DSC data," *Thermochimica acta*, vol. 383, no. 1-2, pp. 119-127, 2002.

[95] J. Lee, H. Choi, M. Shim, and S. Kim, "Kinetic studies of an epoxy cure reaction by isothermal DSC analysis," *Thermochimica Acta,* vol. 343, no. 1-2, pp. 111-117, 2000.
[96] S. Vyazovkin and C. A. Wight, "Model-free and model-fitting approaches to kinetic analysis of isothermal and nonisothermal data," *Thermochimica acta,* vol. 340, pp. 53-68, 1999.
[97] N. Schneider, J. Sprouse, G. Hagnauer, and J. Gillham, "DSC and TBA studies of the curing behavior of two dicy-containing epoxy resins," *Polymer Engineering & Science,* vol. 19, no. 4, pp. 304-312, 1979.
[98] Y. He, "DSC and DEA studies of underfill curing kinetics," *Thermochimica acta,* vol. 367, pp. 101-106, 2001.
[99] R. B. Prime, "Thermosets," in *Thermal characterization of polymeric materials*: Elsevier, 1981, pp. 435-569.
[100] S. Z. Cheng, *Handbook of thermal analysis and calorimetry: applications to polymers and plastics*. Elsevier, 2002.
[101] S. Vyazovkin, A. K. Burnham, J. M. Criado, L. A. Pérez-Maqueda, C. Popescu, and N. Sbirrazzuoli, "ICTAC Kinetics Committee recommendations for performing kinetic computations on thermal analysis data," *Thermochimica acta,* vol. 520, no. 1-2, pp. 1-19, 2011.
[102] H. L. Friedman, "Kinetics of thermal degradation of char-forming plastics from thermogravimetry. Application to a phenolic plastic," in *Journal of polymer science part C: polymer symposia*, 1964, vol. 6, no. 1: Wiley Online Library, pp. 183-195.
[103] H. E. Kissinger, "Differential thermal analysis," *J. Res. Natl. Bur. Stand,* vol. 57, no. 4, p. 217, 1956.
[104] J. H. Flynn and L. A. Wall, "General treatment of the thermogravimetry of polymers," *Journal of research of the National Bureau of Standards. Section A, Physics and chemistry,* vol. 70, no. 6, p. 487, 1966.
[105] S. P. Phansalkar and B. Han, "Deterministic Approach to Obtain Autocatalytic Cure Kinetics Model Constants by Normal Equations of Least-Squares Method," *IEEE Transactions on Components, Packaging and Manufacturing Technology* Submitted on December 17, 2023 2024.
[106] J. Martin, "Kinetic analysis of two DSC peaks in the curing of an unsaturated polyester resin catalyzed with methylethylketone peroxide and cobalt octoate," *Polymer Engineering & Science,* vol. 47, no. 1, pp. 62-70, 2007.
[107] Z. Zhang and C. Wong, "Flip-chip underfill: Materials, process and reliability," *Materials for advanced packaging,* pp. 307-337, 2009.
[108] S. Singer and J. Nelder, "Nelder-mead algorithm," *Scholarpedia,* vol. 4, no. 7, p. 2928, 2009.
[109] L.-C. Hong and S.-J. Hwang, "Study of warpage due to PVTC relation of EMC in IC packaging," *IEEE Transactions on Components and Packaging Technologies,* vol. 27, no. 2, pp. 291-295, 2004.
[110] K. Jansen, M. Hawryluk, and P. Gromala, "Cure dependent characterisation of moulding compounds," in *2011 12th Intl. Conf. on Thermal, Mechanical & Multi-Physics Simulation and Experiments in Microelectronics and Microsystems*, 2011: IEEE, pp. 1/6-6/6.
[111] R. Simha, P. Wilson, and O. Olabisi, "Pressure-volume-temperature properties of amorphous polymers: empirical and theoretical predictions," *Kolloid-Zeitschrift und Zeitschrift für Polymere,* vol. 251, pp. 402-408, 1973.

[112] Y. Sun, Y. Wang, Y. Kim, and B. Han, "Dual-Configuration Fiber Bragg Grating Sensor Technique to Measure Coefficients of Thermal Expansion and Hygroscopic Swelling," *Experimental mechanics*, pp. 1-11, 2013.
[113] D. Roylance, "Engineering viscoelasticity," *Department of Materials Science and Engineering–Massachusetts Institute of Technology, Cambridge MA*, vol. 2139, pp. 1-37, 2001.
[114] S. P. Phansalkar, R. Mittakolu, and B. Han, "Time-dependent Bulk Behavior of Cured Epoxy Molding Compound," in *2023 IEEE 73rd Electronic Components and Technology Conference (ECTC)*, 2023: IEEE, pp. 2093-2100.
[115] S. P. Phansalkar, B. Han, E. Akbari, and P. Vaitiekunas, "On the Viscoelastic Property Measurement of Filled Polymers by Dynamic Mechanical Analyzer (DMA)," in *International Electronic Packaging Technical Conference and Exhibition*, 2022, vol. 86557: American Society of Mechanical Engineers, p. V001T05A004.
[116] J.-H. Baek, D.-W. Park, G.-H. Oh, D.-O. Kawk, S. S. Park, and H.-S. Kim, "Effect of cure shrinkage of epoxy molding compound on warpage behavior of semiconductor package," *Materials Science in Semiconductor Processing*, vol. 148, p. 106758, 2022.
[117] H.-C. Cheng, Z.-D. Wu, and Y.-C. Liu, "Viscoelastic warpage modeling of fan-out wafer-level packaging during wafer-level mold cure process," *IEEE Transactions on Components, Packaging and Manufacturing Technology*, vol. 10, no. 7, pp. 1240-1250, 2020.
[118] S. Park, D. Liu, Y. Kim, H. Lee, and S. Zhang, "Stress evolution in an encapsulated MEMS package due to viscoelasticity of packaging materials," in *2012 IEEE 62nd Electronic Components and Technology Conference*, 2012: IEEE, pp. 70-75.
[119] K. Miyake, T. Yoshida, H. G. Baik, and S. W. Park, "Viscoelastic warpage analysis of surface mount package," *J. Electron. Packag.*, vol. 123, no. 2, pp. 101-104, 2001.
[120] H. F. Brinson and L. C. Brinson, *Polymer engineering science and viscoelasticity*. Springer, 2015.
[121] C. Selvanayagam, R. Mandal, and N. Raghavan, "Comparison of experimental, analytical and simulation methods to estimate substrate material properties for warpage reliability analysis," *Microelectronics Reliability*, vol. 88, pp. 817-823, 2018.
[122] M. Amagai and Y. Suzuki, "Warpage modeling for 3D packages," in *2012 IEEE 14th Electronics Packaging Technology Conference (EPTC)*, 2012: IEEE, pp. 479-489.
[123] D. Xia, B. Wang, C. Liao, Z. Liu, H. He, and L. Liu, "Warpage Behavior Study and Optimization for Ultra-Thin POP Memory with Multi-Stacked Chips," in *2021 22nd International Conference on Electronic Packaging Technology (ICEPT)*, 2021: IEEE, pp. 1-5.
[124] T. Kamon and H. Furukawa, "Epoxy Resins and Composites IV," *Advances in Polymer Science (Springer, Berlin, Heidelberg, 1986) Vol*, vol. 80, pp. 173-202, 1986.
[125] M. P. Group. "Functional networks: Physically crosslinked gels." https://www.cmu.edu/maty/materials/Polymers_with_Specific_Architecture/networks-gels.html (accessed 06/26, 2024).
[126] C. Van't Hof *et al.*, "Novel shear tools for viscoelastic characterization of packaging polymers," *Microelectronics Reliability*, vol. 47, no. 2-3, pp. 240-247, 2007.
[127] J. Pascault and R. Williams, "Glass transition temperature versus conversion relationships for thermosetting polymers," *Journal of Polymer Science Part B: Polymer Physics*, vol. 28, no. 1, pp. 85-95, 1990.

[128] C. Carlini, P. Rolla, and E. Tombari, "Measurement method and apparatus for monitoring the kinetics of polymerization and crosslinking reactions by microwave dielectrometry," *Journal of applied polymer science,* vol. 41, no. 3-4, pp. 805-818, 1990.
[129] H. S. Kim, "Reduction of fabricational thermal residual stress of the hybrid co-cured structure using a dielectrometry," *Composites science and technology,* vol. 67, no. 1, pp. 29-44, 2007.
[130] J. W. Kwon, W. S. Chin, and D. G. Lee, "In situ cure monitoring of adhesively bonded joints by dielectrometry," *Journal of adhesion science and technology,* vol. 17, no. 16, pp. 2111-2130, 2003.
[131] J. S. Kim and D. G. Lee, "Measurement of the degree of cure of carbon fiber epoxy composite materials," *Journal of Composite Materials,* vol. 30, no. 13, pp. 1436-1457, 1996.
[132] J. Schawe, "A description of chemical and diffusion control in isothermal kinetics of cure kinetics," *Thermochimica Acta,* vol. 388, no. 1-2, pp. 299-312, 2002.